สมรรถนะต้านทานแผ่นดินไหวของสะพานแม่ลาวที่ใช้แบริ่งแบบอีลาสโตเมริก และเดือยรับแรงเฉือน

นายไซเฮียง บี

วิทยานิพนธ์นี้เป็นส่วนหนึ่งของการศึกษาตามหลักสูตรปริญญาวิศวกรรมศาสตรมหาบัณฑิต
สาขาวิชาวิศวกรรมโยธา ภาควิชาวิศวกรรมโยธา
คณะวิศวกรรมศาสตร์ จุฬาลงกรณ์มหาวิทยาลัย
ปีการศึกษา 2558

Seismic performances of Mae Lao Bridge with elastomeric bearings and shear dowels

Mr. Syheang Be

A Thesis Submitted in Partial Fulfillment of the Requirements
for the Degree of Master of Engineering Program in Civil Engineering
Department of Civil Engineering
Faculty of Engineering
Chulalongkorn University
Academic Year 2015

Thesis Title	Seismic performances of Mae Lao Bridge with elastomeric bearings and shear dowels
By	Mr. Syheang Be
Field of Study	Civil Engineering
Thesis Advisor	Associate Professor Anat Ruangrassamee, Ph.D.

Accepted by the Faculty of Engineering, Chulalongkorn University in Partial Fulfillment of the Requirements for the Master's Degree

.....Dean of the Faculty of Engineering
(Associate Professor Supot Teachavorasinskun, D.Eng.)

THESIS COMMITTEE

.....Chairman
(Associate Professor Tospol Pinkaew, Ph.D.)
.....Thesis Advisor
(Associate Professor Anat Ruangrassamee, Ph.D.)
.....Examiner
(Assistant Professor Chatpan Chintanapakdee, Ph.D.)
.....External Examiner
(Sukit Yindeesuk, Ph.D.)

ไซเฮียง บี : สมรรถนะต้านทานแผ่นดินไหวของสะพานแม่ลาวที่ใช้แบริ่งแบบอีลาสโตเมริก และเดือยรับแรงเฉือน (Seismic performances of Mae Lao Bridge with elastomeric bearings and shear dowels) อ.ที่ปรึกษาวิทยานิพนธ์หลัก: รศ. ดร.อาณัติ เรืองรัศมี, 124 หน้า.

งานวิจัยนี้เพื่อศึกษาพฤติกรรมของสะพานแม่ลาวที่มีการปรับปรุงด้วยยางแบริ่งสะพาน และ เหล็กเดือยรับแรงเฉือน วัตถุประสงค์ของงานวิจัยคือศึกษาพฤติกรรมของสะพานภายใต้แรงกระทำเนื่องจากแผ่นดินไหวแบบต่างๆ รวมทั้งการเคลื่อนที่ของเสาตอม่อ คานสะพาน ค่าความโค้งของเสา และ กราฟความสัมพันธ์ค่าความเค้นความเครียดของวัสดุเช่น คอนกรีตที่มีการโอบรัด คอนกรีตไม่มีการโอบรัด และเหล็กเสริม นอกจากนี้ยังมีการศึกษาผลของยางแบริ่งและเหล็กเดือยรับแรงเฉือนในสะพาน รวมถึงพิจารณาเสาตอม่อริมที่ใช้และไม่ใช้แบบจำลองสปริงซึ่งเป็นตัวแทนของดิน ในการจำลองสะพานได้ใช้โปรแกรม OpenSees และจำลองแบริ่งด้วยแบบจำลองเชิงเส้น และจำลองเหล็กเดือยรับแรงเฉือนด้วยแบบจำลองไม่เชิงเส้น เสาได้แบ่งเป็นสามชิ้นส่วนได้แก่ ชิ้นส่วนแข็งเกร็ง ชิ้นส่วนจุดหมุนพลาสติค และชิ้นส่วนอีลาสติค แบบจำลองคานก็เช่นเดียวกันกับเสา การวิเคราะห์นี้มุ่งเน้นไปที่พิจารณาผลของความหนาของแบริ่งและเหล็กเดือยขนาดต่างๆกันว่าส่งผลต่อผลตอบสนองในโครงสร้างสะพานอย่างไร จากการวิเคราะห์แสดงให้เห็นว่าขนาดความหนาของแบริ่งสามารถช่วยลดการเคลื่อนที่ของเสา โดยช่วยลดการเคลื่อนที่ของตอม่อแบบผนังได้ประมาณ 10%-25% ค่าความโค้งของหน้าตัดมีค่าลดลงโดยลดลงมากที่สุดในกรณียางแบริ่งหนา 8 ซม. เหล็กเดือยรับแรงเฉือนจะช่วยลดการเคลื่อนที่ของเสาและคานได้ดี

ภาควิชา วิศวกรรมโยธา ลายมือชื่อนิสิต .....

สาขาวิชา วิศวกรรมโยธา ลายมือชื่อ อ.ที่ปรึกษาหลัก .....

ปีการศึกษา 2558

5670543921 : MAJOR CIVIL ENGINEERING
KEYWORDS: RC BRIDGE, ELASTOMERIC BEARING, SHEAR DOWEL

SYHEANG BE: Seismic performances of Mae Lao Bridge with elastomeric bearings and shear dowels. ADVISOR: ASSOC. PROF. ANAT RUANGRASSAMEE, Ph.D., 124 pp.

The research investigates the behavior of the Mae Lao Bridge, one of the damaged bridges, with elastomeric bearing and shear dowel. The objective of the research is to study the behavior of the bridge under different ground motion including the pier displacement, the girder displacement, the curvature of the column, and the stress-strain curve of the material including the confined, the unconfined concrete, and the reinforcement. Also, the effect of adding the elastomeric bearing and the shear dowel to the bridge is observed. In addition, the difference between the bridge with and without abutment soil spring is compared as well. The whole bridge is modeled using the computational program OpenSees. The bearings are modeled using linear model and the shear dowel as bilinear model; Columns are modeled with three separated parts: the rigid part, the plastic hinge part and the elastic part and so the beams. The analysis is focused on how the different thickness of bearing makes to the bridge structural reaction. The results show that the thicker thickness of bearing can help reduce the displacement of the columns, but increase the displacement on girders. The reduction of displacement on top of pier is about 10% to 25% from 2cm-thick bearing to 8cm-thick bearing of the wall-type piers. The curvature of the section is reduced as well even in some cases that the 8cm-thick bearing keep the section elastic without yielding. On the other hand, the shear dowel reaches its objective as well to help reduce both the displacement on top of pier and the girders if comparing to the case without shear dowels. Although other cases of different thickness of bearing help reduce the displacement and curvature of the column but still the 8cm-thick bearing case gives the best performances overall.

Department:	Civil Engineering	Student's Signature	.....
Field of Study:	Civil Engineering	Advisor's Signature	.....
Academic Year:	2015		

ACKNOWLEDGEMENTS

I am very thankful to my adviser for being my greatest help in my research. He always guides me and suggests me some good idea to improve the research content. Also, he also helped me with financial support in the research.

Another person I would like to thank is my mother for she is always my inspiration in my life. Every time I meet the struggle, she will stay by my side and console me with her sweet voice.

CONTENTS

Page

Page

Page

Page

TALBES

FIGURES

CHAPTER 1 : INTRODUCTION

1.1. Problem statement:

5th May 2014, the largest earthquake ever recorded occurred in Chiang Rai, the northern side of Thailand which caused enormous destruction of residences and infrastructures. With its epicenter being in Thailand, this earthquake had the magnitude of being reported as 6.3 M_L with 7 km depth (S. Soralump, 2014). Thousands of residences collapsed or almost collapsed.

Table 1.1: Top 10 earthquake magnitude recorded in Thailand (S. Soralump, 2014)

No.	Date	Magnitude	Earthquake epicenter
1	5-May-14	6.3	Pran, Chiangrai
2	22-Apr-83	5.9	Srisawat, Kanchanaburi
3	17-Feb-75	5.6	Thasongyang, Tak
4	6-May-14	5.6	Pran, Chiangrai
5	6-May-14	5.6	Maesuay, Chiangrai
6	22-Dec-96	5.5	Border Thailand and Laos
7	15-Apr-83	5.5	Srisawat, Kanchanaburi
8	22-Apr-83	5.2	Srisawat, Kanchanaburi
9	21-Dec-95	5.2	Prao, Chiangmai
10	5-May-14	5.2	Muang, Chiangrai

As reported by Department of Public Work, it was found that more than 10000 residences were damaged and 1 person was died in this event. After this striking earthquake, buildings were needed to be assessed for safety criteria. Engineers from all over the country gathered in Chiangrai Province and participated in this project of building safety evaluation. All evaluation work was finished completely in three weeks times. 475 houses were highly damaged, 2180 were partially damaged and reparable,

and 7714 has a minor damage. Beside residences, 138 temples and 56 schools were highly damaged (S. Soralump, 2014). This serious damage could happen because these constructions were designed without seismic consideration. The reconnaissance of seismic design has been recently the interesting topic for designers even the construction takes place in non-seismic zone.

Not only buildings, bridges are also the targets for safety evaluation. Particularly, bridges are very vulnerable among the structures since they are usually built on soft soils (M. N. Priestley, Seible, & Calvi, 1996). To help reduce damage in bridge structures in the area in the future, the understanding of the bridge responses under specific ground motion and the bridge structural damage estimation are needed. Additionally, when they are not completely damaged and are thought to be usable, the rehabilitation must be applied for economical purpose. Thus, many retrofit methods were proposed and studied in bridge structures. One of the proposed methods is to apply the isolation bearings, of which various types are available today, to the bridges instead of normal rubber pad. The behaviors of the bridge under earthquake load were investigated by various researches and these researches were studied with different kinds of isolation bearings.

On the other hand, without serious structural damage, bridges can face with failure of unseating of superstructures, the fall down of the deck of bridge during earthquake. This is one of the most common failure modes for the bridges (M. N. Priestley et al., 1996). Therefore, restrainers are installed to restrict the relative displacement between superstructures and substructures. Bridges equipped with restrainers were observed to have minor damage after earthquake (Jónsson, Bessason, & Haflidason, 2010). The restrainers are expected to remain in elastic range in small earthquake while restraining the displacement with reaction force and to yield when big earthquake comes and dissipate energy thus help reduce the damage of the structures (M. N. Priestley et al., 1996). In Thailand, shear dowels are generally used and are regarded to work as the shear panel. The shear dowels are installed along with elastomeric bearings in most cases as shown in figure 1. Together with shear dowels, elastomeric bearings can increase the performance of the bridge by energy dissipation of the shear dowels and also unseating failure of the bridge can be avoided.

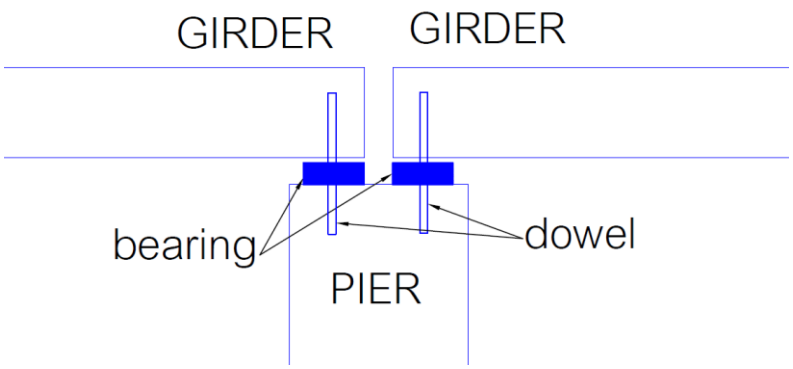

Figure 1.1: application of elastomeric bearings and shear dowels to the bridge structure

However, researches related to application of elastomeric bearings and shear dowels together were in short. Performances of the bridge with and without application of elastomeric bearings and shear dowels will be investigated in this study.

1.2. Objective of study:

Elastomeric bearings and shear dowels have been used to bridges for seismic protection over the country so detail investigation on the performance of the bridge equipped with these isolators are needed. Therefore, the objective of this study is:

1. To study the behavior of bridge elements including abutment, pier and girders without seismic isolation device after severe earthquake.
2. To observe the performance of the bridges after installation of the isolators and compare results with that of non-isolator.
3. To assess the effect of rubber bearing and shear dowels to the dynamic response of the bridge elements.

1.3. Scope of study:

Scope of this study is defined as below:

- There are three ground motions used in the analysis, such as MAECHAN, MAESAI, and PHAYAO ground motions. They were recorded during the earthquake in Chiangrai province and Phayao province.

- The ground motion is in the longitudinal direction of the bridge for the mass of the structure is put in this direction as well
- The RC bridge is Mae Lao Bridge, located in the district of Mae Lao, Chiang Rai province. The structural detailing of the bridge is based on the standard drawings for highway construction by Department of Highway, 1994.
- The computational program used in the analysis is OpenSees (Open Software for Earthquake Engineering Simulation).
- Bridge responses are analyzed and observed by dynamic analysis of 3D nonlinear fiber models.
- The geometry and property of the elastomeric bearings and of the shear dowels are the parameters for sensitivity study.
- The rotational stiffness of the bearing is ignored in the study. The big stiffness was applied instead.
- The pounding effect of the pier girder is ignored in this study.

1.4. Research methodology:

The research will be focused on the bridge structural performance during earthquake. The flowchart below shows how it process to get the analysis result.

First of all, the important literatures must be reviewed to get the idea on how to process the research. After having the basic understanding on how to do the research, the study of the bridge structural detail will be the next step. Also, the initial modeling of the bridge with various verification along will be included as well. After the verification of the model, the introduction of the elastomeric bearing model, the shear dowel model, and the abutment soil spring model will be included to the original model. Finally, all related data will be obtained and will be analyzed.

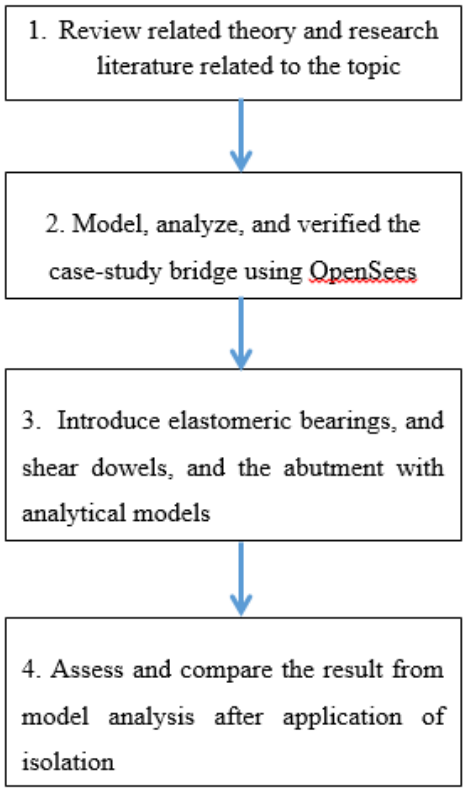

Figure 1.2: Flowchart of the research methodology

CHAPTER 2 : LITERATURE REVIEW

In this chapter is introduced an overview of previous researches related to seismic behaviors of bridge structures under earthquake with different types of bearings. Both experimental and analytical results from those researchers are briefly described in the following section. In consequence, the bridge elements perform better generally with application of bearings than without bearings. Furthermore, the performance may differ with different type of bearings and restrainer. Also, the material models are reviewed and included in this chapter in order to get options for models to use in the analysis.

2.1. Analytical models of materials:

In the nonlinear analysis, which this research is based on, the nonlinear behavior of material is needed. The analytical models of materials used in this study are comprised of unconfined concrete for cover of RC element, confined concrete for core concrete, and a longitudinal reinforcement model.

2.1.1. Unconfined concrete:

Kent and Park (1971) introduced the stress-strain relation of unconfined concrete which possesses two separated parts: first part is when $\varepsilon_c \le \varepsilon_0$ and another is $\varepsilon_c > \varepsilon_0$.

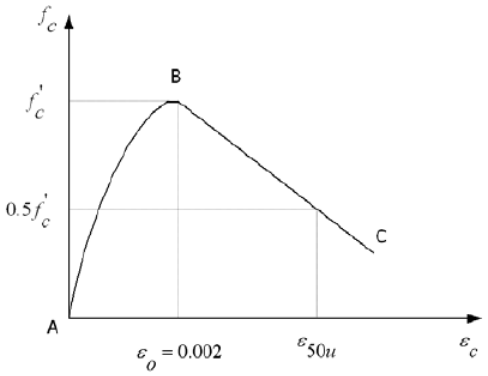

Figure 2.1 Stress-strain relation of unconfined concrete (Kent & Park, 1971)

The stress starts increasing from 0 to reach the maximum stress of the concrete, which is f_c'. It is clear that at the maximum point of stress (point B) the strain is $\varepsilon_0 = 0.002$. After that, the stress begins to decrease assumingly linearly. Both parts were represented by the equations below:

$$f_c = f_c^{'}\left[\frac{2\varepsilon_c}{\varepsilon_0} - \left(\frac{\varepsilon_c}{\varepsilon_0}\right)^2\right]$$

$$f_c = f_c^{'}\left[1 - z\left(\varepsilon_c - \varepsilon_0\right)\right]$$

$$\text{where: } z = \frac{0.5}{\varepsilon_{50u} - 0.002} \text{ and } \varepsilon_{50u} = \frac{3 + 0.002 f_c^{'}}{f_c^{'} - 1000}$$

Notation: ε_c : longitudinal compressive concrete strain

ε_0 : strain at maximum stress, assumingly 0.002

f_c : longitudinal compressive concrete stress (psi)

$f_c^{'}$: maximum stress of cylinder specimen (psi)

ε_{50u} : strain at 50% of maximum stress (obtained from material testing)

2.1.2. Confined concrete:

There are many researches related to the model application of confined concrete. Some of the most popular ones are introduced next:

Kent and Park (1971) gave the stress-strain relation of confined concrete subjected to uniaxial loading.

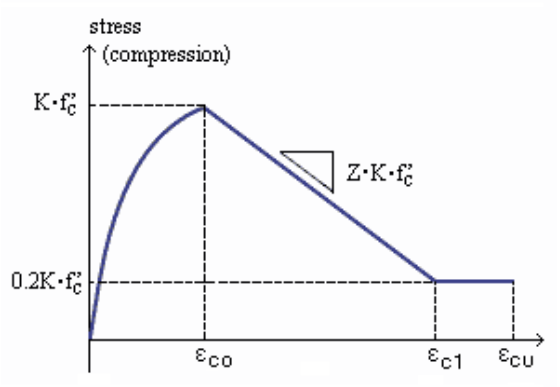

Figure 2.2:Stress-strain relation of confined concrete (Kent & Park, 1971)

The proposed model consists of three different parts:

1. When $0 \le \varepsilon_c \le \varepsilon_0$, the ascending part varies in parabolic manner with same equation of the unconfined concrete. The strain at maximum stress point is assumed to be $\varepsilon_0 = 0.002$.
2. When $\varepsilon_0 < \varepsilon_c \le \varepsilon_{20u}$, the falling part was assumed varying linearly from maximum stress f_c' to $0.2f_c$' where ε_{20u} is the strain at 20% of stress point (obtained by experimental result). However, the falling slope Z is changed and the function was proposed:

$$z = \frac{0.5}{\varepsilon_{50h} + \varepsilon_{50u} - 0.002}$$

where: ε_{50h}: additional strain due to the confinement $\varepsilon_{50h} = \frac{3}{4}\rho" \sqrt{\frac{b"}{s}}$

$\rho"$:volumetric ratio (ratio of the volume of transverse reinforcement to the volume of confined concrete core

$\rho" = \frac{2(b"+d")A_s^"}{b"d"s}$.

$b"$: shorter dimension of confined concrete core

$d"$: longer dimension of confined concrete core

$A_s^"$: cross-sectional area of the hoop bar

s: center to center of the hoops

3. When $\varepsilon_c > \varepsilon_{20u}$, this part was called the sustaining branch since it was assumed to be a constant value equal to 0.2 of the maximum stress of cylinder specimen. The equation was proposed as followed:

$$f_c = 0.2 f_c^{'}$$

Mander, Priestley, and Park (1988) also proposed a material model for confined concrete in the form of stress-strain relation, which considered the transverse and longitudinal reinforcement for both rectangular and circular sections. The figure below is the stress-strain relation of confined and unconfined concrete under monotonic loading and the constitutional equations were proposed:

$$f_c = \frac{f_{cc}^{'} xr}{r - 1 + x^r}$$

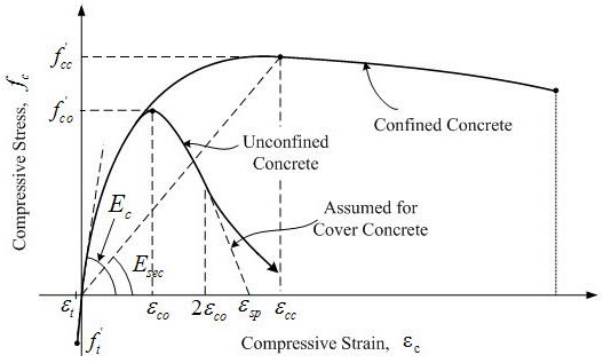

Figure 2.3: Stress-strain relation of confined and unconfined concrete under monotonic loading (Mander et al., 1988)

where: f_c : longitudinal compressive concrete stress

$$x = \frac{\varepsilon_c}{\varepsilon_{cc}} \text{ with } \varepsilon_{cc} = \varepsilon_{c0}\left[1 + 5\left(\frac{f_{cc}^{'}}{f_{co}^{'}} - 1\right)\right] \text{ and } \varepsilon_{c0} = 0.002$$

$f_{co}^{'}$: unconfined concrete compressive stress calculated by formula

$$f_{cc}^{'} = f_{c0}^{'}\left(2.254\sqrt{1 + \frac{7.94 f_l^{'}}{f_{co}^{'}}} - 2\frac{f_l^{'}}{f_{co}^{'}} - 1.254\right)$$

ε_c : longitudinal compressive concrete stress

ε_{cc} : unconfined concrete compressive strain

$$r = \frac{E_c}{E_c - E_{\sec}} \text{ with } E_{\sec} = \frac{f_{cc}^{'}}{\varepsilon_{cc}}$$

E_c : tangent modulus of elasticity of the concrete $E_c = 5000\sqrt{f_{co}^{'}}$

$f_l^{'}$: effective lateral confining pressure $f_l^{'} = f_l \cdot k_e$

f_l : lateral confining pressure

k_e :confinement effectiveness coefficient $k_e = \frac{A_e}{A_{cc}}$

A_{cc} : area of the confined concrete $A_{cc} = A_c\left(1 - \rho_{cc}\right)$

ρ_{cc} : ratio of area of longitudinal reinforcement to area of section

A_e : area of an effective confined concrete core at midway between the levels of the transverse reinforcement

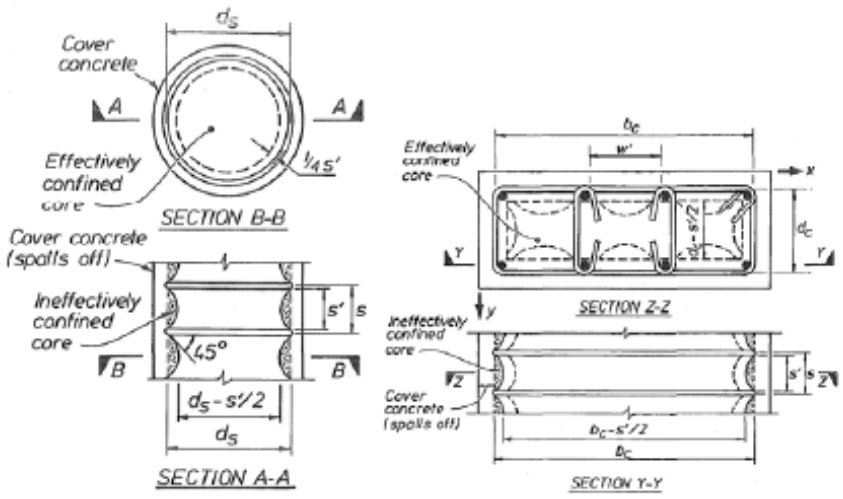

(a) Circular hoop reinforcement (b) Rectangular hoop reinforcement

Figure 2.4: Effectively confined of concrete core (Mander et al., 1988)

For circular section, the area of core concrete is defined as $A_c = \frac{\pi}{4} d_s^2$. The effective area of confined concrete core area was proposed:

$$A_e = \frac{\pi}{4}\left(d_s - \frac{s'}{2}\right)^2 = \frac{\pi}{4} d_s^2 \left(1 - \frac{s'}{2d_s}\right)^2$$

$$\text{Thus, } k_e = \frac{\left(1 - \frac{s'}{2d_s}\right)^2}{1 - \rho_{cc}}$$

For rectangular section, the core concrete section area is $A_c = b_c d_c$. The effective confined concrete area of a regular hoop with the initial tangent slope of 45° was proposed in the equation below:

$$A_e = \left(b_c d_c - \sum_{i=1}^{n} \frac{\left(w_i^{'}\right)^2}{6} \right) \left(1 - \frac{s'}{2b_c}\right) \left(1 - \frac{s'}{2d_c}\right)$$

Thus,
$$k_e = \frac{\left(1 - \sum_{i=1}^{n} \frac{\left(w_i^{'}\right)^2}{6 b_c d_c}\right) \left(1 - \frac{s'}{2b_c}\right) \left(1 - \frac{s'}{2d_c}\right)}{1 - \rho_{cc}}$$

Hoshikuma, Kawashima, Nagaya, and Taylor (1997) introduced the relationship between stress and strain of the confined concrete obtained from analysis of experimental results for low volumetric ratio ranging from 0.3% to 0.5%. Several parameters including sectional shape, volumetric ratio, hoop spacing, hook configuration and cross tie, were varied and all specimens were tested under uniaxial loading. This model agreed well with the experimental results and it satisfied with boundary conditions at point A, B, and C.

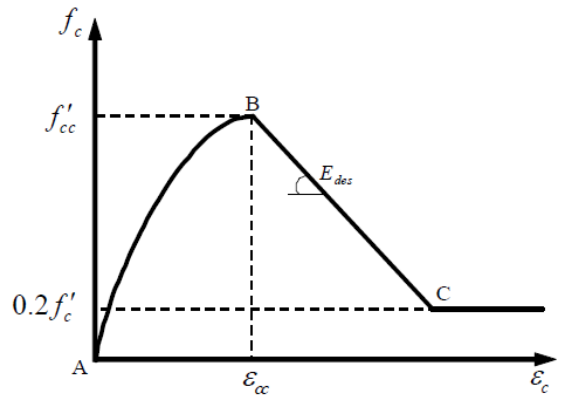

Figure 2.5: Stress-strain model of confined concrete (Hoshikuma et al., 1997)

This model is similar to that of Kent and Park (1971) that it consists of three parts: the ascending part, the falling part, and the sustain part. All three equations were proposed respectively as below:

$$f_c = E_c \varepsilon_c \left[1 - \frac{1}{n} \left(\frac{\varepsilon_c}{\varepsilon_{cc}} \right)^{n-1} \right]$$

$$f_c = f_{cc} + E_{\text{det}} \left(\varepsilon_c - \varepsilon_{cc} \right)$$

$$f_c = 0.2 f_c^{'}$$

Where:

$$n = \frac{E_c \varepsilon_{cc}}{E_c \varepsilon_{cc} - f_{cc}}$$

ε_{cu} : ultimate strain with proposed equation $\varepsilon_{cu} = \varepsilon_{cc} + \frac{f_{cc}}{2E_{\text{det}}}$

f_{cc} : maximum longitudinal compressive concrete stress, $f_{cc} = f_{c0} + 3.8\alpha\rho_s f_{yh}$

ε_{cc} : longitudinal compressive strain at maximum stress $\varepsilon_{cc} = 0.002 + 0.033\beta\frac{\rho_s f_{yh}}{f_{co}}$

E_{det} : deterioration rate with $E_{\text{det}} = 11.2\frac{f_{co}^2}{\rho_s f_{yh}}$

E_c : initial stiffness

f_{co} : unconfined concrete compressive stress

ρ_s : volumetric ratio (ratio between the volume of transverse reinforcement and volume of confined concrete core).

f_{yh} : yield strength of the transverse reinforcement

α and β are modification factors depending on confined sectional shape

For circular section $\alpha = 1.0$ and $\beta = 1.0$

For square section $\alpha = 0.2$ and $\beta = 0.4$

2.1.3. Longitudinal reinforcement model:

Gomes and Appleton (1997) presented the modified nonlinear stress-strain model of longitudinal reinforcement including buckling under cyclic loading from the model proposed by Menegotto and Pinto (1973). This modified model comprised of four different parts: elastic, yielding, hardening and Baushinger effect.

The equation of Menegotto and Pinto (1973) was modified as follow:

$$\sigma_s^* = \beta\varepsilon_s^* + (1-\beta)\frac{\varepsilon_s^*}{\left[1+\left(\varepsilon_s^*\right)^R\right]^{1/R}}$$

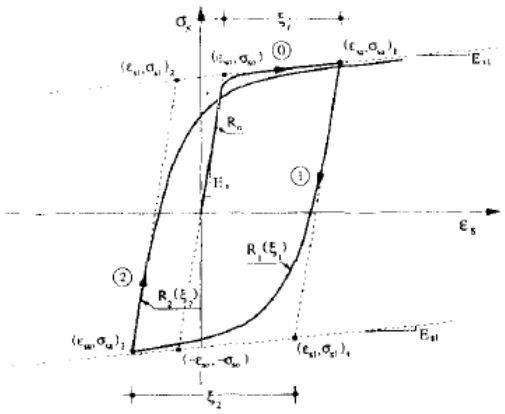

Figure 2.6: Stress-strain relation of reinforcement (Gomes & Appleton, 1997)

Where:

σ_s^* : normalized stress defined as followed:

$$\text{First load: } \sigma_s^* = \frac{\sigma_s}{\sigma_{s0}}$$

$$\text{First load reverse: } \sigma_s^* = \frac{\sigma_s - \sigma_{sa}}{2\sigma_{s0}}$$

ε_s^* : normalized strain defined as followed:

$$\text{First load: } \varepsilon_s^* = \frac{\varepsilon_s}{\varepsilon_{s0}}$$

$$\text{First load reverse: } \varepsilon_s^* = \frac{\varepsilon_s - \varepsilon_{sa}}{2\varepsilon_{s0}}$$

$\sigma_{so}, \varepsilon_{so}$: stress and strain respectively at the yield point of the bilinear envelope

$\sigma_{sa}, \varepsilon_{sa}$: stress and strain respectively at the inversion point

β : ratio between the hardening stiffness and the tangent modulus of elasticity at the origin $\beta = \frac{E_{s1}}{E_s}$

R: constant taking into account the Baushinger effect $R = R_0 - \frac{a_1 \xi}{a_2 + \xi}$

R_0, a_1, and a_2: constants of materials equals to 20, 19, 0.3 respectively suggested by Gomes and Appleton (1997).

2.2. Analytical models of Elastomeric bearing:

Akogul and Celik (2008) studied the effect of elastomeric bearing modeling parameters on the seismic performance of highway bridges with precast concrete girders. The simplified SDF model and the full 3D model were proposed to satisfy the objective of the study. The linear and nonlinear analyses of the bridge performance were studied. Results from the both analysis were compared.

Elastomeric bearings were modeled as link elements as shown below.

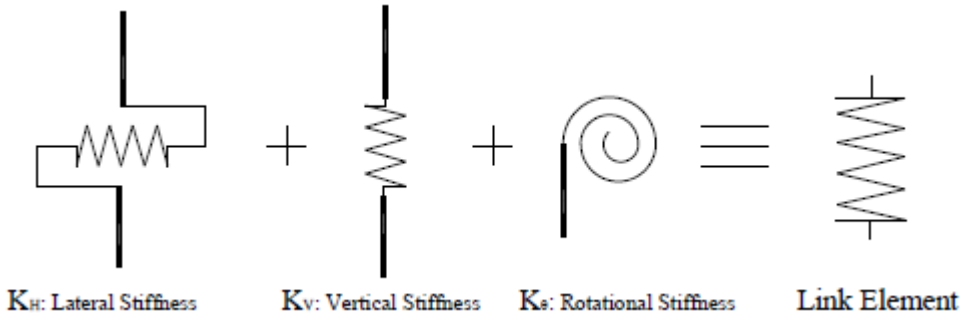

Figure 2.7: Link element model of elastomeric bearing (Akogul & Celik, 2008)

The bridge chosen to be studied was the Akcaova Bridge in Turkey. However, to show the effect of rigidity of the substructure on the seismic response, the bridge with shorter or stiffer pier was also analyzed.

The full model of the bridge with elastomeric bearing was created using SAP2000 with some important assumption.

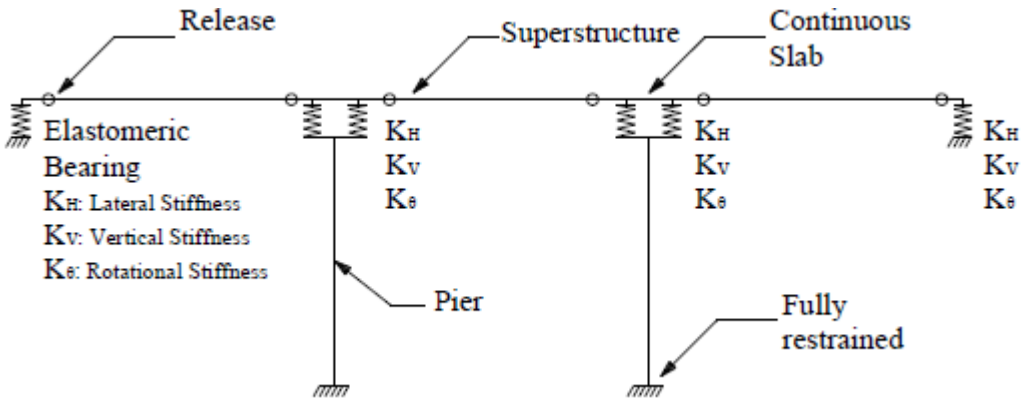

Figure 2.8: Model of bridge with elastomeric bearings (Akogul & Celik, 2008)

The results were discussed in the special case of seismic performance of the bridge with and without elastomeric bearing. It could be observed that elastomeric bearings help perform better the bridge response but there were some other parameters that affected the performance as well such as geometry of bridge or specifically the pier rigidities. Also discussion included that elastomeric bearings has bigger effect on bridges with short and rigid piers than those with long and flexible columns. As in the analysis, the natural period is elongated by 80% and internal forces are reduced by 60%.

2.3. Analytical model of Shear dowels:

One of the most general failure modes of bridges, particularly multi-span bridges with tall columns, under severe earthquake is the unseating of the superstructures or decks. To prevent this, installation of restrainers between superstructures and substructures was proposed to add extra energy dissipation and reduce the displacement of the superstructures (Priestley, 1996).

Zhang, Zhang, and Zhang (2012) studied the cyclic performance of both static and dynamic of a low-yield-strength steel shear panel damper. From the basic of previous research of the performance of steel shear panel under static incremental cyclic loading, the author developed it further by including the fatigue characteristic by static and dynamic constant cyclic tests. The research was focused on the performance of steel with four different shear strain amplitudes (20%, 30%, 40% and 50%) in both static and dynamic test while in dynamic test, two frequencies 0.5Hz and 1 Hz, were adopted.

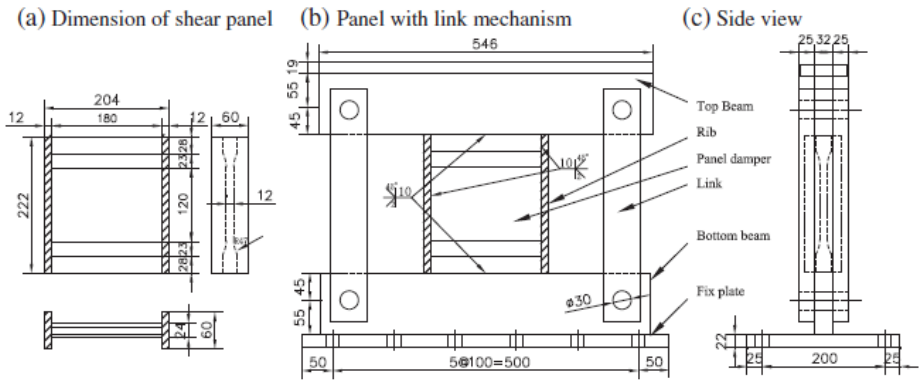

Figure 2.9: Specimen for the test (Zhang et al., 2012)

The results showed that for the static test, the hysteresis curves were as spindle while they were almost rectangular in the dynamic test. It could be concluded that the maximum damper force could be taken as the effective damper force in the plastic range and the hysteresis loops for both tests could be modeled simply as perfect elastic-plastic, which was adopted by AASHTO also. This was because in both test, the stress hardening including strain hardening, cyclic hardening, and strain rate hardening only occurred in the first cycle and reached the MDF.

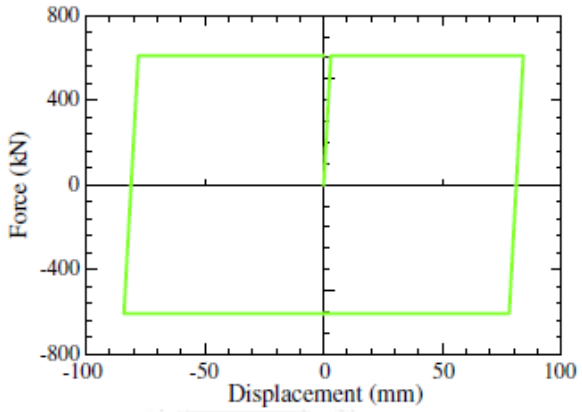

Figure 2.10: Perfect elastic-plastic model (Zhang et al., 2012)

Failure modes of the specimens were similar for all static tests, which were caused by the expansion of the crack starting from the panel corners. In contrast, the dynamic tests gave a different cause for the failure mode. In the dynamic test, the in-plane shear deformation is dominant, which could be reason for failure of specimens.

It was concluded that the damper force was getting stable until failure after the maximum force in the first cycle for static tests. However, the cyclic damper force deterioration towards failure with the increasing cycles in dynamic tests was observed.

Deng, Pan, Su, Ran, and Xue (2014) developed a new energy dissipation restrainer for bridges using a steel shear panel. The restrainers remain elastic and provide a reaction force to help decrease the deck displacement in small earthquake for maintaining the functionality of the bridge, and to yield and dissipate energy to reduce deformation of superstructure and pier for big earthquake.

There were 5 specimens for doing the experiment with different geometries. They were tested using displacement control under cyclic loading with the maximum

loading amplitude was 54mm. Also, the finite element models of the restrainers were proposed using ABAQUES.

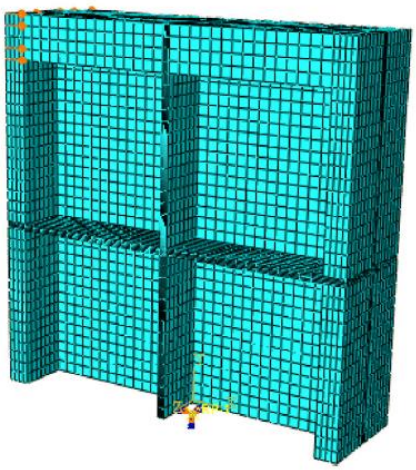

Figure 2.11: Finite element model of energy dissipation plate (Deng et al., 2014)

The FE models provided a good prediction of deformation which agreed well with the physical tests. However, in the specimen S5, the strength obtained from experiment decreased in the last cycle while the FE model did not show this characteristic. This is because there was no low-cycle fatigue damage that was not included in the material properties of the model and that the restoring force of the FE model would not decrease due to the low-cycle fatigue of the restrainer.

Parameters study was also conducted to investigate the relation of shear panel property to the ultimate strength of the restrainer. An equation was proposed to easily estimate this ultimate strength of the steel restrainers. This equation provided a small relative error of the ultimate strength obtained from FE simulation.

$$Q = \alpha \left(\frac{b}{h} \right)^{\beta} \frac{f_u t_w w}{\sqrt{3}}$$

where:

f_u : ultimate stress of the steel

t_w : thickness of the web

α : 1.134 and β : 0.1125

The authors concluded that with the proposed energy dissipation restrainer, the appropriate design of restrainers can provide a stable and saturated hysteresis curve.

Also, the horizontal steel stiffeners were needed to restrict the buckling of the webs and side flange at the same time.

2.4. Seismic behaviors/responses of bridges under earthquake:

Dimitriadou (2007) showed the seismic bridge responses through time-history nonlinear dynamic analyses. Seven different ground motions were chosen and applied to the three-span bridge model using the advanced computational program, ANSRuop-Bridge. Lead-rubber bearing was the selected isolator for the bridge and its design was based on Eurocode-8. Result of the seismic performance of the bridge in 3D model was obtained and assessed with and without installation of isolation devices.

The deck and the piers were modeled as prismatic beam elements in 3D and masses are automatically lumped at the nearest node of the model. Piers were considered as fixed and the bridge as simply supported to the abutment. P-delta effect is included in the analysis.

Figure 2.12: Discretization of the bridge (Dimitriadou, 2007)

The result showed that as the PGA level of the model of the bridge without isolation devices increases from 0.25g, 0.35g and 0.45g, the responses of the bridge increases in pier but the values of the deck responses stay at the same level. In addition, it is proven that the left pier varied only 10% and the right pier maintained the same pattern of response. The bridge containing limited ductile design may suffer shear failure since the shear strength corresponding to the maximum flexural strength was not considered.

Mechanical characteristics of lead-plug bearings were studied and designed to fit with the existing bridge model to prevent it from any failure. Bilinear approximation of hysteretic force-displacement behavior of the bearings was assumed. The standard used for design was Eurocode-8.

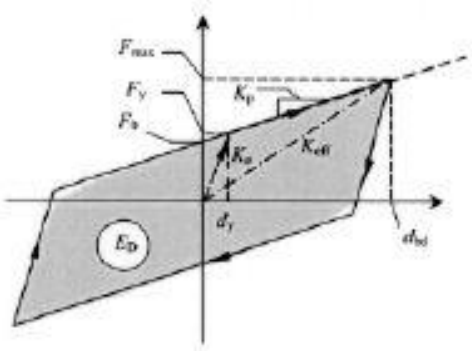

Figure 2.13: Bilinear approximation of hysteretic force-displacement behavior (Dimitriadou, 2007)

After the implementation of seismic isolation to the model, the flexural damage indices was reduced notably of 10% to 45% and the shear damage indices of 70% to 80%, which reached the objective of the study to lengthen the period, to reduce the shear forces and to increase the energy dissipation. The bridge responded exactly the same with or without isolation except that the peak values increase proportionally.

Ghosh, Singh, and Thakkar (2011) stated that failure of bearings and insufficient seat length cause the unseating of bridges. Their paper evaluated the performance of four different types of protection devices to limit the displacement of the superstructure during earthquake.

3D model of bridge has been developed using the program SAP2000 Nonlinear and applying five accelerograms design response spectrum. Masses were lumped at discrete point in the model in SAP 2000 with 3D frame elements. In addition, different types of bearings and protection devices were modeled differently. Elastomeric bearings modeled using elastic link elements, rigid stopper modeled using a link elements having high stiffness, yielding stopper and steel restrainer modeled by elasto-plastic bi-linear link elements, and SMA modeled through the parallel combination of 2 elastic multi-linear link elements and one plastic bilinear element in series with a hook element.

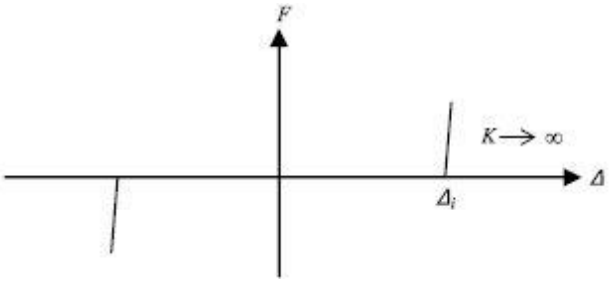

Figure 2.14: Force-displacement behavior of a rigid stopper device (Ghosh et al., 2011)

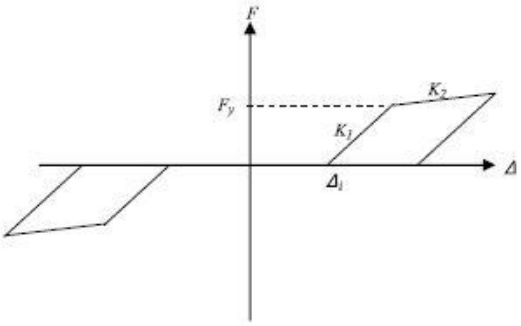

Figure 2.15: Force-displacement behavior of a yielding stopper and a steel restrainer (Ghosh et al., 2011)

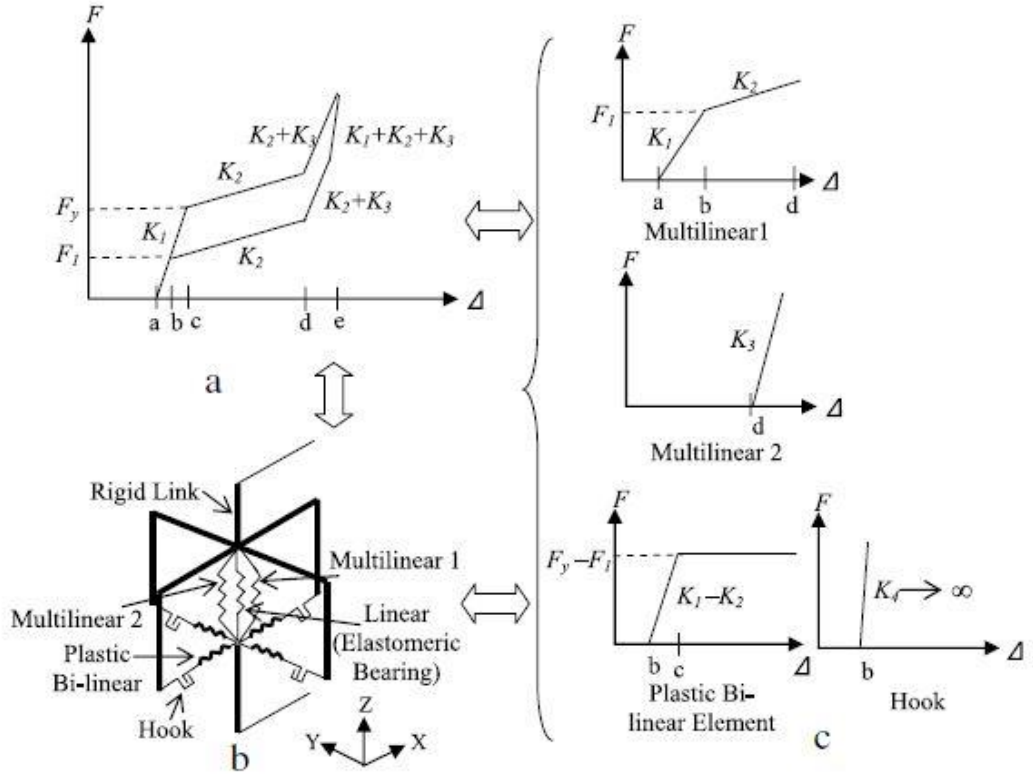

Figure 2.16: Force-displacement behavior of superelastic SMA restrainer device (Ghosh et al., 2011)

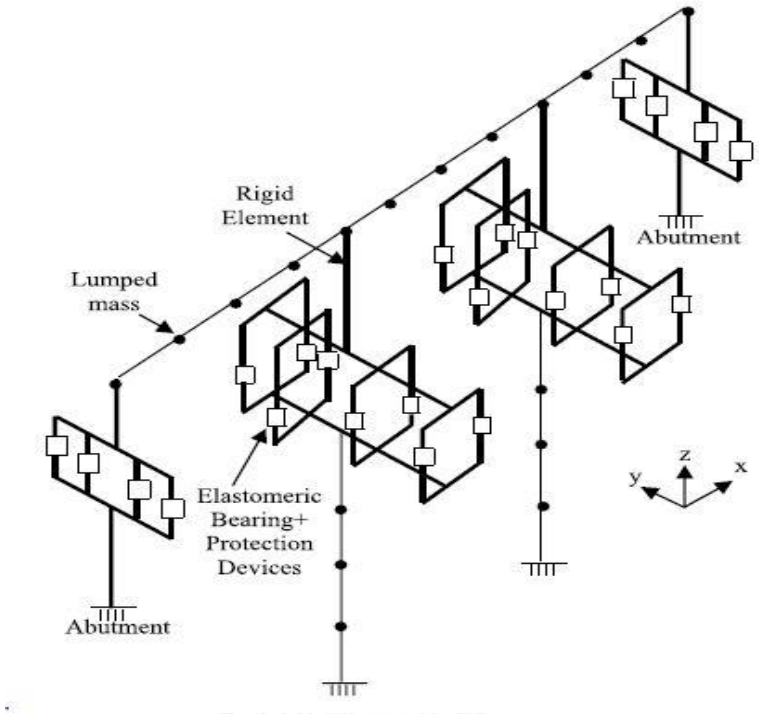

Figure 2.17: 3D model of the bridge (Ghosh et al., 2011)

Five earthquakes record were scaled in the frequency domain to simulate the design response spectrum. The bridge was analyzed in case of elastomeric bearings without protection device while nonlinear time history analysis in case of elastomeric bearings with protection devices.

From the analysis result, authors concluded that along the longitudinal direction could the displacement of the bearings be controlled but it resulted in higher pier and abutment force. Among the four devices, the rigid stopper gave the least pier force but higher abutment force due to the installation of device in the piers. The yielding stopper device, on the other hand, resulted in minimum pier displacement and forces in case of MCE loading. Under DBE, however, the steel restrainer device was slightly better than SMA restrainer and yielding stopper devices with minimum displacement of pier and bearings, and minimum forces in pier and abutment. Contrarily, it was noted that SMA had higher energy dissipation as compared to other protection devices and had additional protection against higher ground motion level due to strain hardening effect at larger strains. Along the transverse direction, all devices performed comparably while rigid stopper was not as good as in the longitudinal direction.

Siqueira, Sanda, Paultre, and Padgett (2014) evaluated the performance of natural rubber seismic isolators as a retrofit method for typical multi-span concrete bridge in eastern Canada. The research also focused on the vulnerability of concrete girder bridge retrofitted with the natural rubber bearing by development of fragility curves. The analytical result showed that the parameters that affected the bridge responses were the effective stiffness of isolator, the abutment stiffness, and the gap between deck and abutment. Also variations in gross bridge geometry and ground acceleration contents were also included in the critical parameters. In addition, it was proven that utilization of seismic isolators reduced the curvature demand on columns but increased the deformation demand on abutment walls.

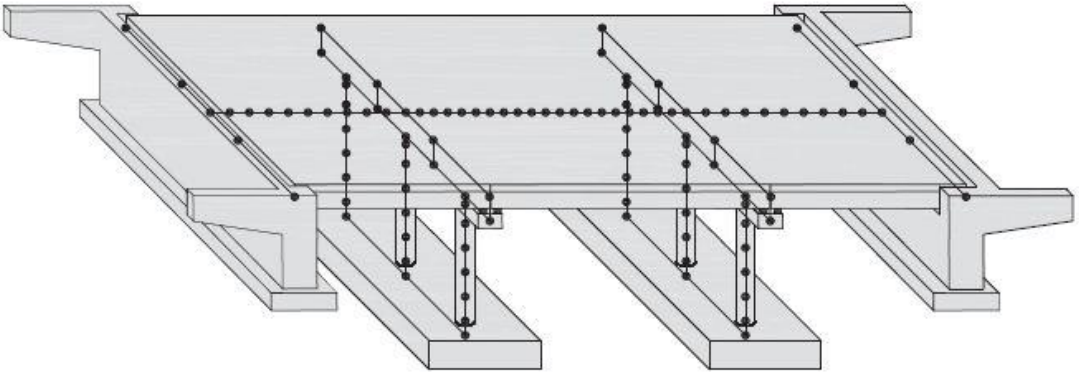

Figure 2.18: Bridge 3D model (Siqueira et al., 2014)

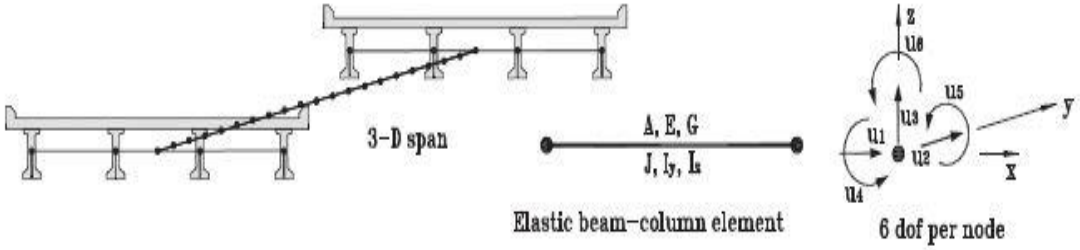

Figure 2.19: General superstructure model (Siqueira et al., 2014)

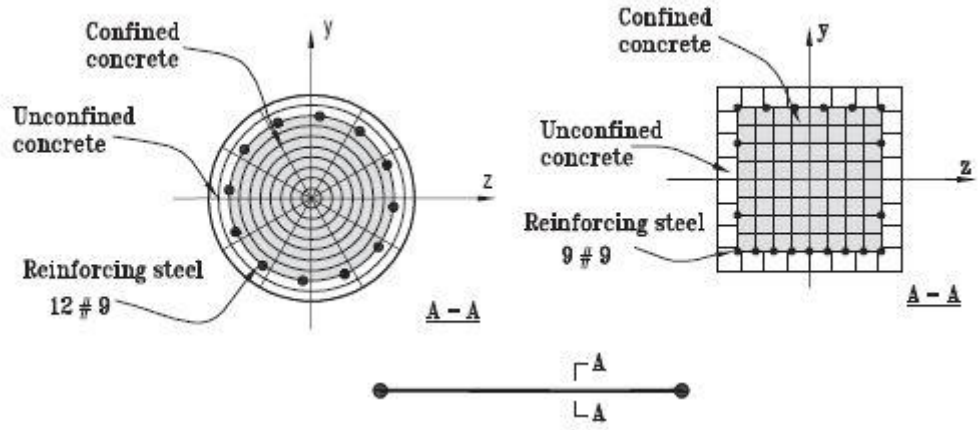

Figure 2.20: Nonlinear beam-column element with fiber section (Siqueira et al., 2014)

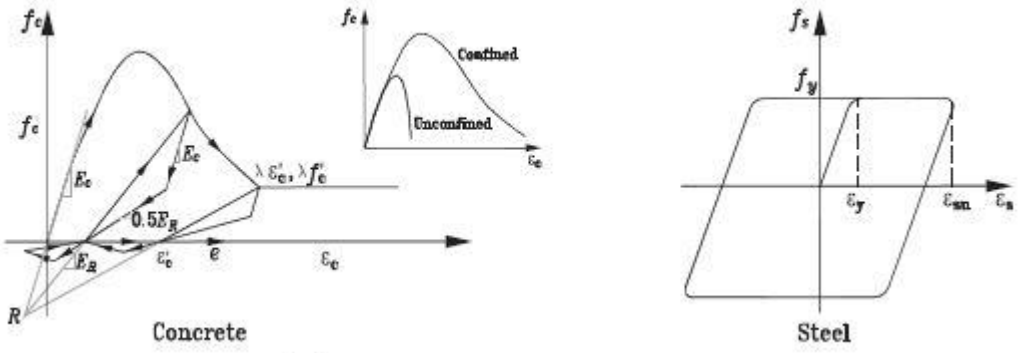

Figure 2.21: Uniaxial materials in fiber sections (Siqueira et al., 2014)

Finite element models in OpenSees for all bridge elements are in figure above. Deck and concrete girders were modeled using elastic beam-column elements and represented by a single element in the center of the cross section. All mechanical properties were defined in figure above as well. Zero-length elements were used to be the connections between bents or abutment with superstructure. Pounding effect was modeled by bilinear element to represent the energy dissipation during the contact between decks or deck-abutment. Abutment model was taken from Wilson (1988). Since the simply-supported three-span bridges were constructed with elastomeric bearing, the retrofit methods were to design the new bearings as isolation devices.

Most of the bridges needed to be retrofitted were accompanied with elastomeric bearing and retrofit concept was to replace this type of bearings to isolation devices.

The isolation bearings were considered as bilinear model from Naeim and Kelly (1999) to obtain the period of 2 seconds with shear modulus of 0.75 MPa and damping of 7.5%. The characteristic ratio of elastic and post-elastic stiffness was taken as 4 and 10% of yield deformation of total height of bearings.

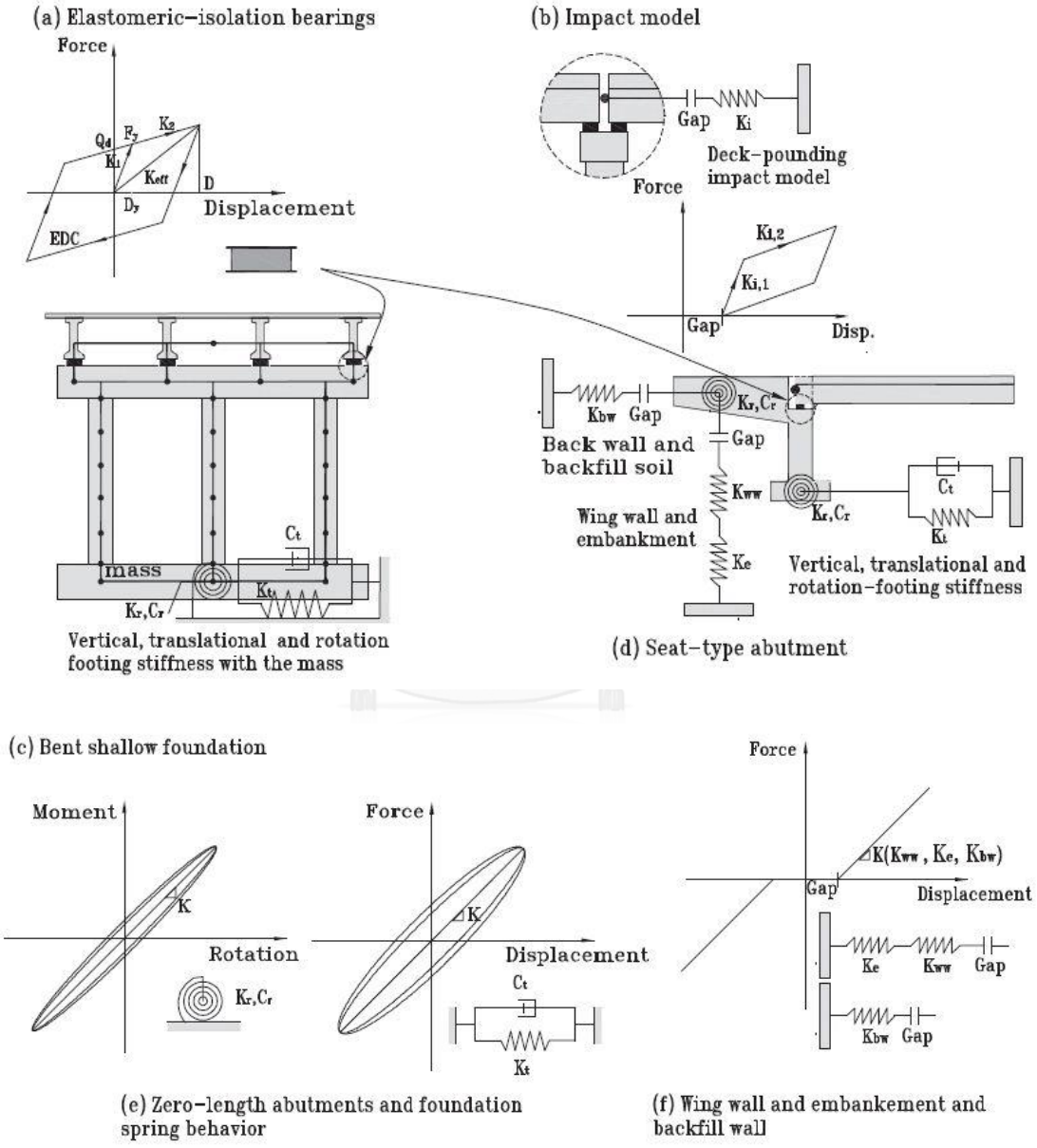

Figure 2.22: Bridge zero length elements (Siqueira et al., 2014)

For a given ground motion input, the complete 3D nonlinear analysis of bridge model proved the essential distribution of pier flexibility, mass distribution and the

variability of ground motion in the response of RC bridge. The seismic isolation of the model helped reduce the abutment-footing deformation but also helped decrease the demand of columns.

A sensitivity study was conducted applying the design-of-experiments (DOE) principles to assess the different parameters affecting the responses of the bridges in Quebec, Canada. The dynamic analysis showed that variation of study parameters changed the responses of bridge elements and that the use of seismic isolators reduced the abutment-footing deformation and reduced the column strength demand and variability of component responses in both cases of bridges from contribution of natural rubber bearings. Deformation demand of the abutment back and wing walls, however, increased due to the increased deformation of bearings.

The study also revealed that among the sensitivity parameters the isolator effective stiffness, abutment initial stiffness, and abutment gaps played an important role in the screening study to affect the most in bridge responses.

2.5. Abutment soil spring stiffness:

Bozorgzadeh, Ashford, Restrepo, and Nimityongskul (2008) investigated the stiffness and ultimate strength of bridge abutment using the soil-dependent model. The research was divided into 2 phases: the experimental phase and the nonlinear computational model phase. The theoretical reviews focused on different methods of calculating abutment soil spring stiffness including Log Spiral method, Coulomb method, Rankine method, and Caltrans method.

Table 2.1: Comparison of methods for computing the passive pressure on abutment wall (Bozorgzadeh et al., 2008)

Method / Soil type	Log Spiral (kips)	Coulomb (kips)	Rankine (kips)	Caltrans (kips)
Sand (ϕ=38°, c=0, γ=125 pcf	698	525	229	793
Clayey sand (ϕ=33°, c=500 psf, γ=120 pcf)	923	617	392	793

Caltrans method gave the same soil spring capacity since it does not regard of soil type (Caltrans, 2004). However, the Log Spiral gave different soil capacity for these

two types of soil and Rankine method underestimated the capacity. In short, both Log Spiral method and Caltrans gave acceptable range of soil spring stiffness.

The Caltrans method is based on the results from large scale abutment testing at UC Davis (Maroney, 1995). It suggests that the linear elastic demand model shall include an effective abutment stiffness that accounts for expansion gaps and incorporates a realistic value for the embankment fill response. The initial embankment fill stiffness regardless of soil types is $K_i = 20\frac{kip/in}{ft}\left(11.5\frac{kN/mm}{m}\right)$. Also, the initial stiffness should be adjusted proportional to the back wall height in the equation below:

$$K_{abut} = \begin{cases} K_i \times w \times \left(\frac{h}{5.5}\right) & \text{U.S. units} \\ K_i \times w \times \left(\frac{h}{1.7}\right) & \text{S.I. units} \end{cases}$$

Where, w is the width of the back wall for seat and diaphragm abutments, respectively.

CHAPTER 3 : STRUCTURAL MODEL AND PARAMETERS

This chapter is all about how to model the targeted bridge and about introducing all the related parameters for the modeling.

3.1. Bridge description:

A RC bridge, Mae Lao Bridge, was chosen to be studied in this project and OpenSees is considered to be the most appropriate computational program for modeling the case study bridge since it is proven by many researches to be the most suitable program for nonlinear dynamic analysis.

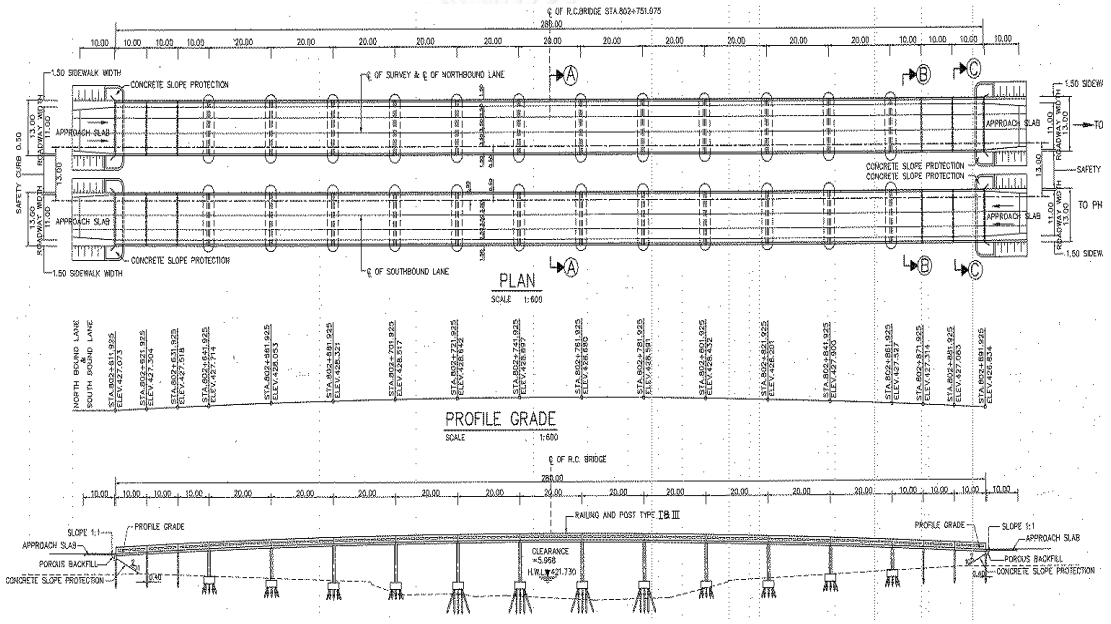

Figure 3.1: General view of Mae Lao Bridge (DOH, 1994)

The bridge is comprised of 18 spans with 2 different kinds of span length, 10 meters and 20 meters. There are 6 spans of 10-meter length of which 3 are at both end. 12 spans of 20 meters are located in the middle of the bridge. The roadway width is 13 meters along the bridge. There are 2 types of piers in this bridge: the piers that support the shorter spans and the piers that support the longer spans. The piers with shorter span is the pile-bent type with 7-meter height and the longer-span piers is the wall-type piers with 10-meter height. The height of the pier types is assumed to be equal in the model.

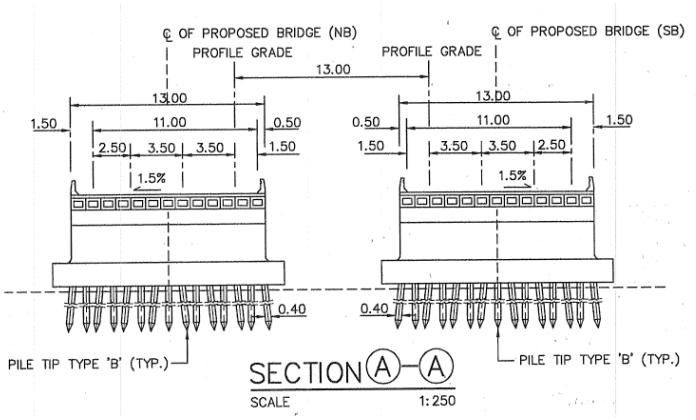

(a): The wall-type pier view

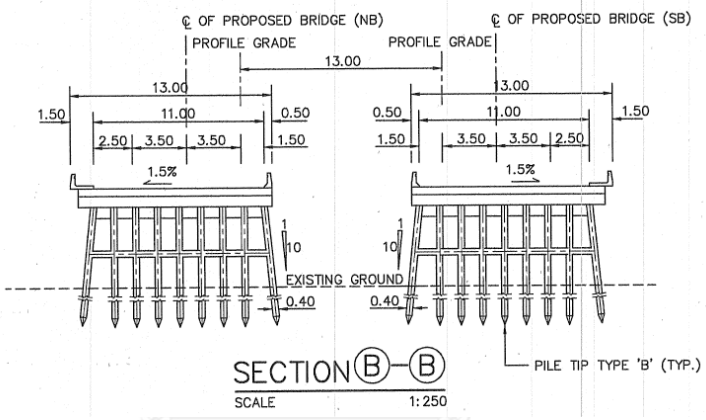

(b): The pile-bent pier view

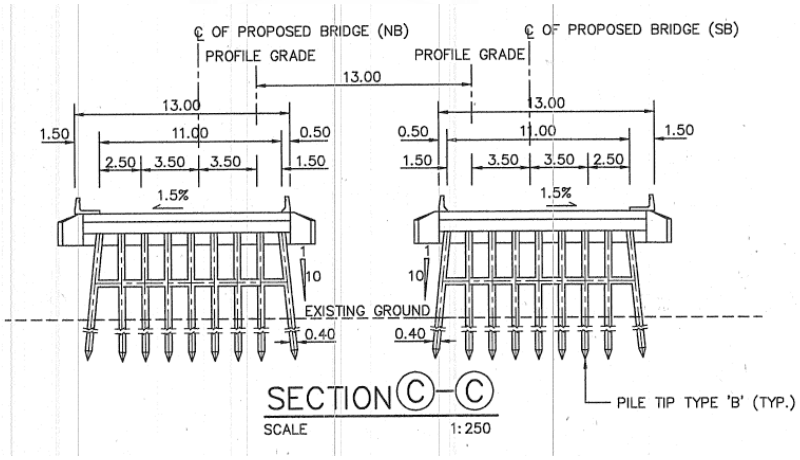

(c): The pile-bent pier view at the abutment

Figure 3.2: Section of piers of the bridge (DOH, 1994)

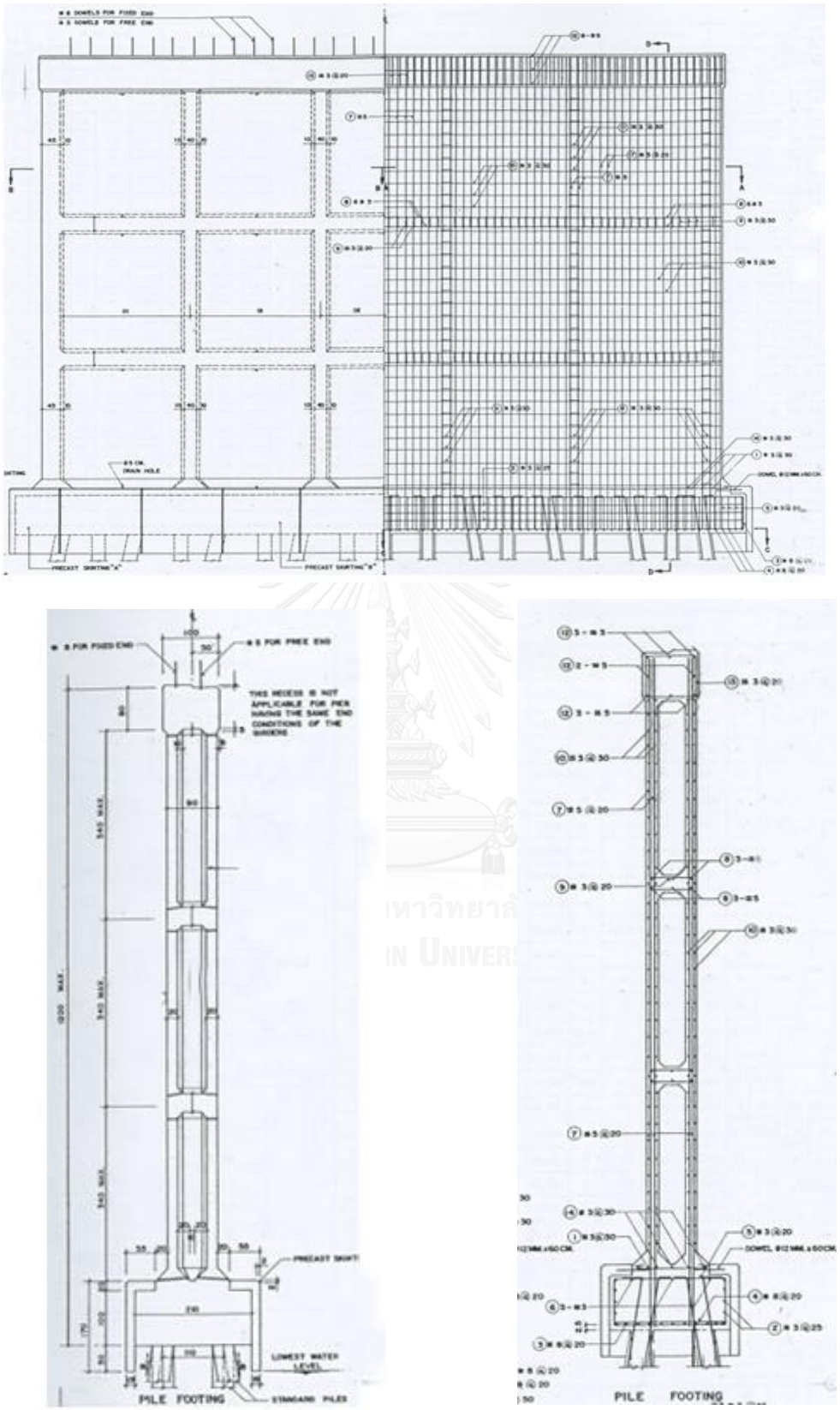

Figure 3.3: Front view of Reinforcement detail of the wall pier (DOH, 1994)

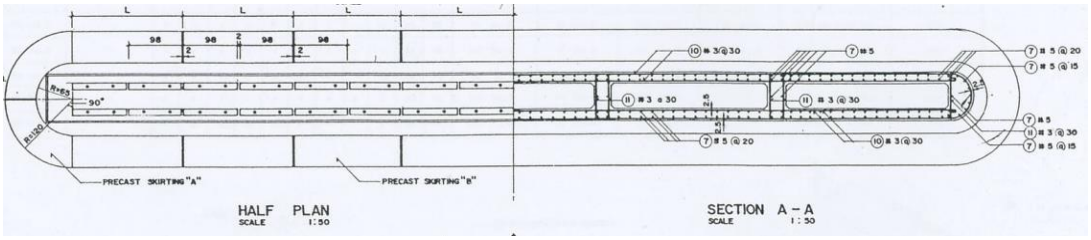

Figure 3.4: Top view of elastomeric bearings and shear dowel and reinforcement of pile caps (DOH, 1994)

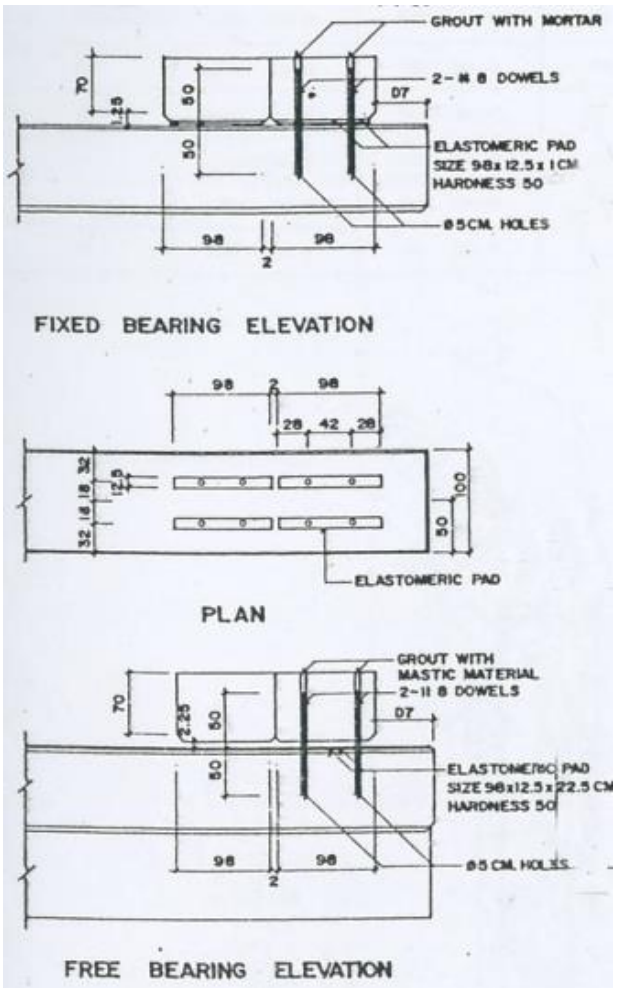

Figure 3.5: Detail of elastomeric bearings and shear dowel (DOH, 1994)

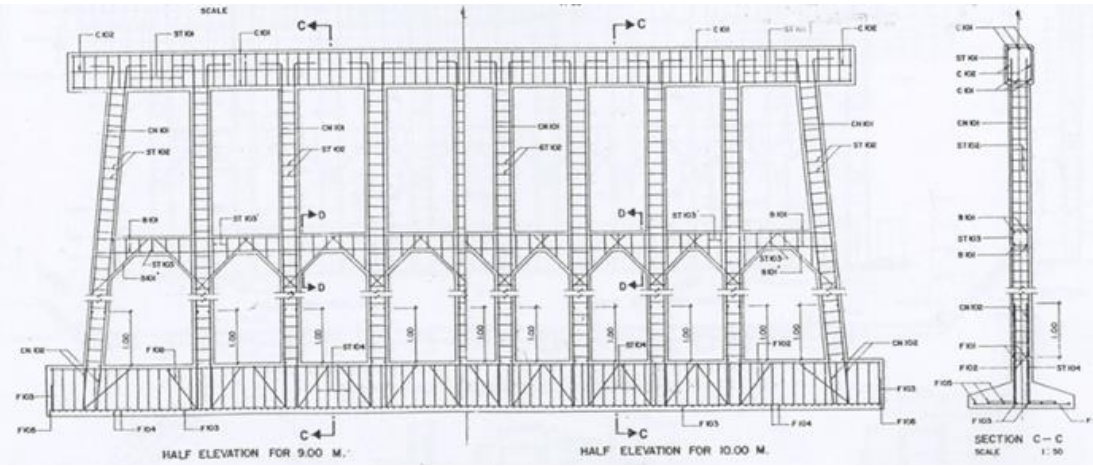

Figure 3.6: Reinforcement detail of pier for 9.0m and 10.0m span (DOH, 1994)

3.2. Structural elements:

3.2.1. Fiber elements:

Fiber elements play an important roles in the nonlinear analysis. In OpenSees, the fiber elements are composed of fiber sections and then many sections are combined together to be a fiber element.

3.2.1.1. Fiber section:

A fiber section has a general geometric configuration formed by sub-regions of simpler, regular shapes, which can be a normal quadrilateral, triangular, or circular regions called *patches*. Also, the reinforcement of the elements can be specified in order to make the section more realistic to the real reinforced concrete section (Silvia Mazzoni, 2007).

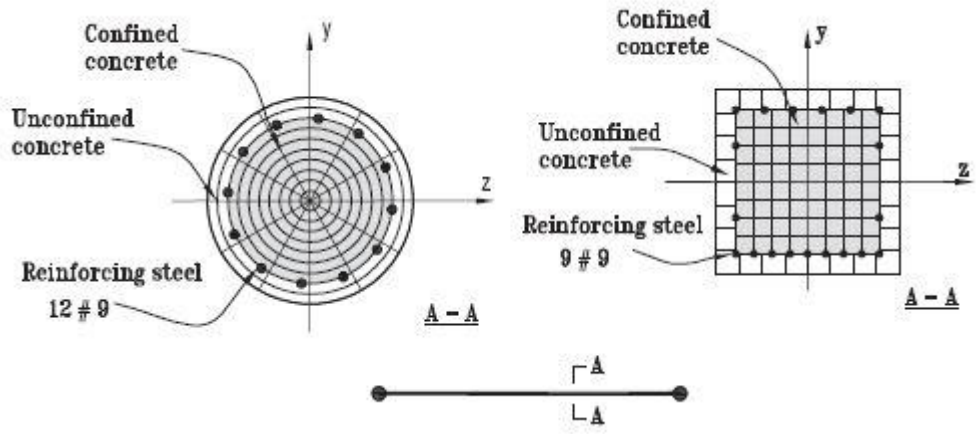

Figure 3.7: Nonlinear beam-column element with fiber section ((Siqueira et al., 2014)

The figure above shows the example of fiber section in both circular and rectangular section. In OpenSees, we can control the number of sub-region to optimize the generation of the result.

3.2.1.2. Plastic hinge:

The length of plastic hinge is also one of the most important parameters in the nonlinear analysis. In many previous researches specified the most appropriate lengths of plastic hinge to both give better analytical results and save time in the analysis.

$$L_p = 0.022 d_b f_y \quad \text{(Priestley, 1996)}$$

where:

d_b : diameter of longitudinal reinforcement in meters.

f_y : yield stress of longitudinal reinforcement in MPa.

So:

$$L_p = 0.022 d_b f_y = 0.022 \times 0.025 \times 493 = 0.271 m$$

3.2.2. Elastic elements:

In 3D modeling, elastic elements are modeled with more parameters than in the 2D modeling. The basic parameters for elastic elements include:

- **A** : Area of section
- **I_y, I_z** : Moment of inertia
- **J** : Torsional constant

For rectangular section, the formula is followed:

$$J = ab^3 \left(\frac{1}{3} - 0.21 \frac{b}{a} \left(1 - \frac{b^4}{12a^4} \right) \right)$$

Where:

a: the length of the long side

b: the length of the short side

- **Ec** : Young modulus or Elastic modulus of material (in most case, the value of Young modulus is from concrete material excluding reinforcement's).
- **Gshear** : shear modulus of material.

3.2.3. Rigid elements:

Theoretically, the rigid elements are usually located at the connection between column and beam. The rigid elements are similar to the elastic elements in term of characteristic but the value of each parameters is changed.

The recommended values are below:

- Area of section: $A_{rigid} = A \times 10^{6} (m^2)$
- Moment of inertia: $I_{rigid} = I \times 10^{4} (m^4)$

3.3. Fiber modeling of RC column:

This part of the chapter is about the modeling of a RC column. This step is the beginning of the whole bridge modeling. Since we have the previous researches, we can compare the analytical result of current model with the previous one.

3.3.1. Data from previous research (Vorakorn, 2008):

Table 3.1: Property of unconfined and confined concrete obtained from test (Vorakorn, 2008)

Type concrete	Ec (MPa)	fc1 (MPa)	Ɛ1 (m/m)	fc2 (MPa)	Ɛ2 (m/m)
Unconfined	27203	-33.5	-0.002	0	-0.0045
confined	27203	-34.6	-0.0025	7.1	-0.0053

Table 3.2: Property of unconfined and confined concrete obtained from test (Vorakorn, 2008)

Type steel	Es (MPa)	fy (MPa)	Strain hardening
Deformed Bar	194000	493	0.008

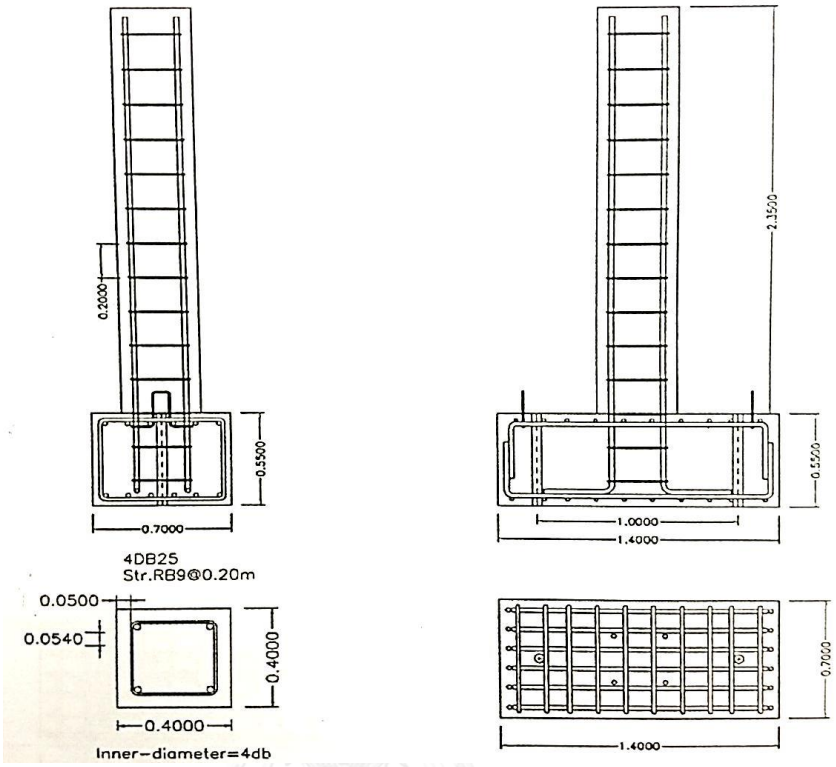

Figure 3.8: Reinforcement detail of tested RC column (Vorakorn, 2008)

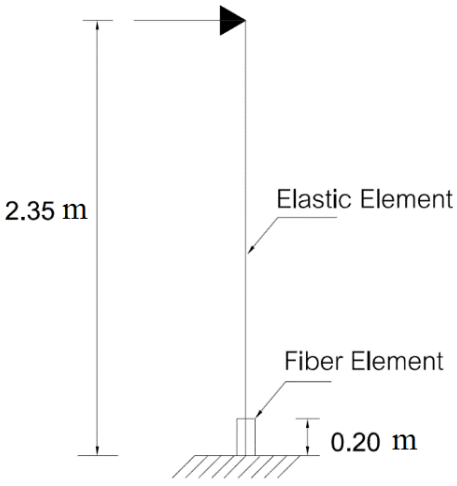

Figure 3.9: Model of RC column

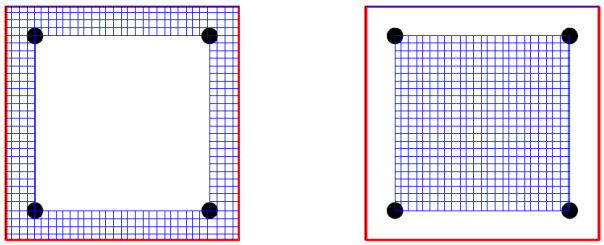

Unconfined concrete fiber model Confined concrete fiber model

Figure 3.10: Model of fiber section of RC column

3.3.2. Analytical results from OpenSees:

3.3.2.1. Moment-curvature graph of section:

First of all, the graph of moment-curvature of the section of the column was shown below. The comparison of section between two computational programs: OpenSees and Xtract.

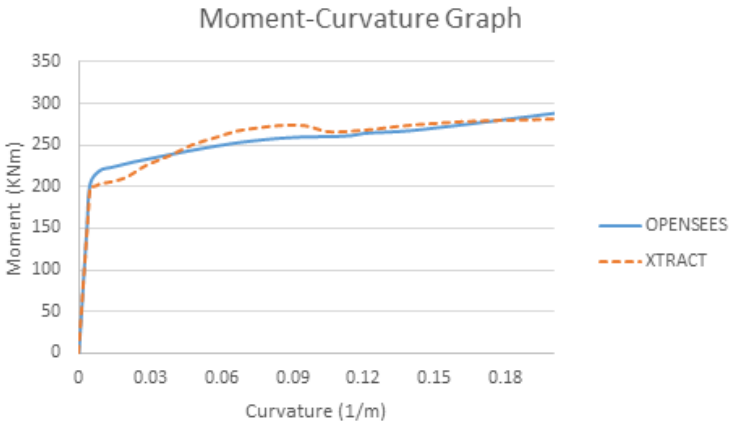

Figure 3.11: Moment – Curvature graph of section of the column

Both graphs give similar results at the beginning for it has the same elastic material when it has not yielded yet. The section yields, in OpenSees, at 0.00879/m of curvature, 203.2 KNm of moment. Xtract gave the yielding point at 0.006837/m of curvature, 200.3 KNm of moment. In short, the similar result helps prove the trustable coding in OpenSees.

3.3.2.2. Stress-strain curve of materials:

The full model of column was built in OpenSees as figure above and the cyclic loading was applied to the model. After cyclic loading analysis, the comparison of

stress-strain curves of unconfined concrete, confined concrete, and reinforcement are shown in graphs below:

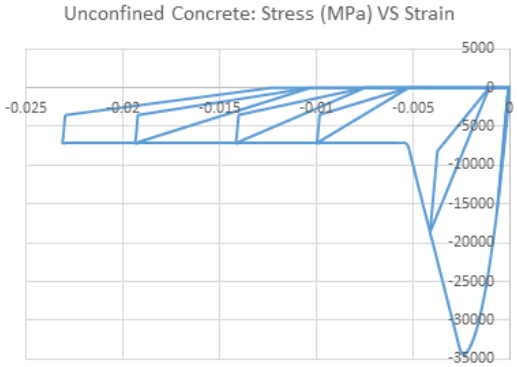

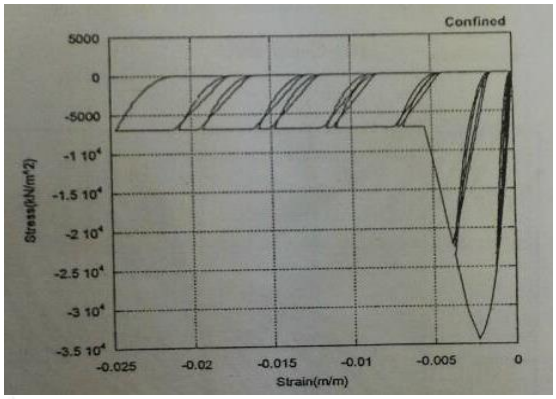

(a): Stress strain curve of the unconfined concrete of the column

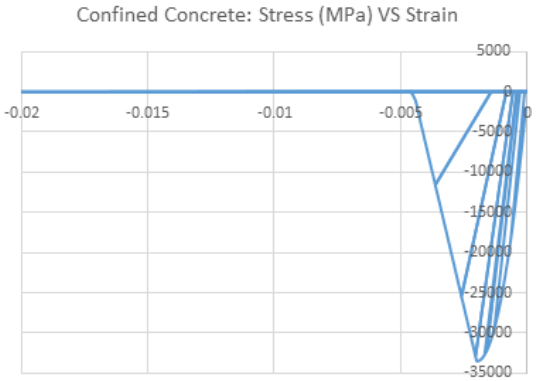

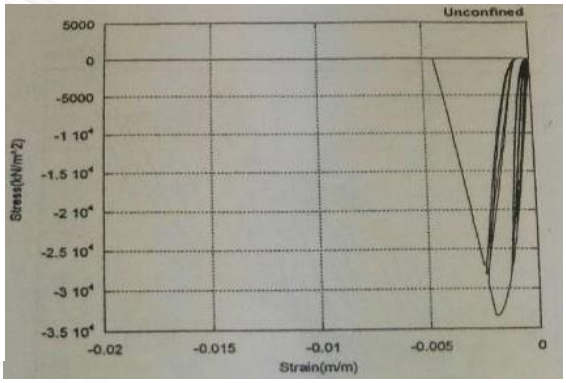

(b): Stress strain curve of the confined concrete of the column

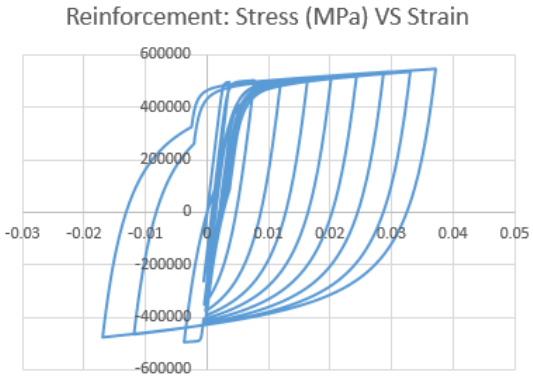

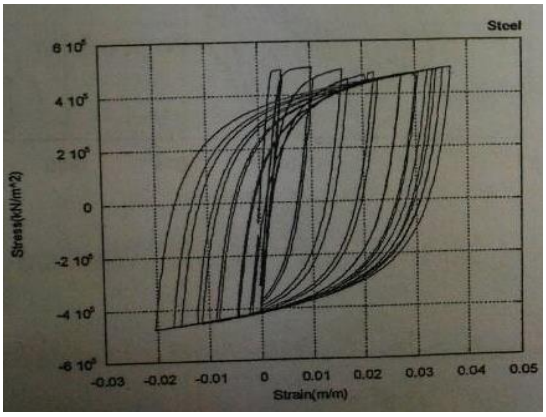

(c): Stress strain curve of the reinforcement of the column

Figure 3.12: Stress-strain curve of the confined concrete, the unconfined concrete and the reinforcement

3.3.2.3. Load-Displacement curve:

The load-displacement curve was computed by OpenSees and compared also with the result from experimental test. The load-displacement curve was composed of the load, which is the reaction of the column at the support and the displacement at the top of the column.

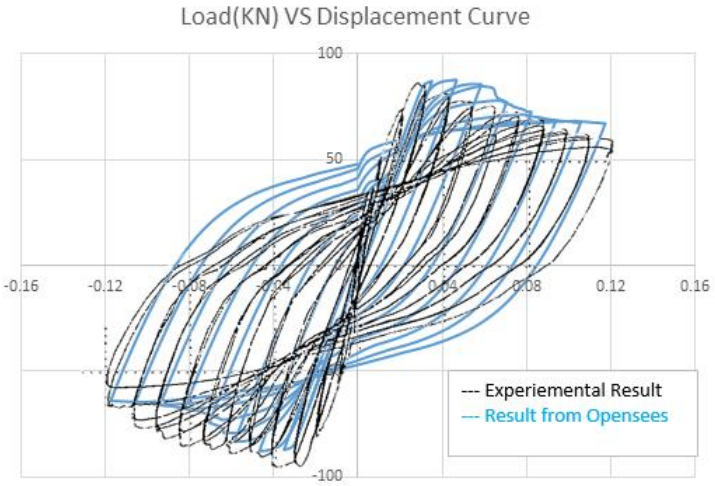

Figure 3.13: Load-displacement graph of the column

The result obtained from OpenSees is acceptable comparing with that from experiment. After the column, the structure was improved into a simple frame.

3.4. Fiber modeling of RC frame:

3.4.1. Data from previous research:

The material property of the frame was listed in the table below:

Table 3.3: Parameters of concrete and reinforcement (Anil & Altin, 2007)

Compressive strength of Concrete (Mpa)	Yield strength of reinforcement bars (Mpa)				
	D=16mm	D=10mm	D=8mm	D=6mm	D=4mm
21.8	425	475	592	427	326

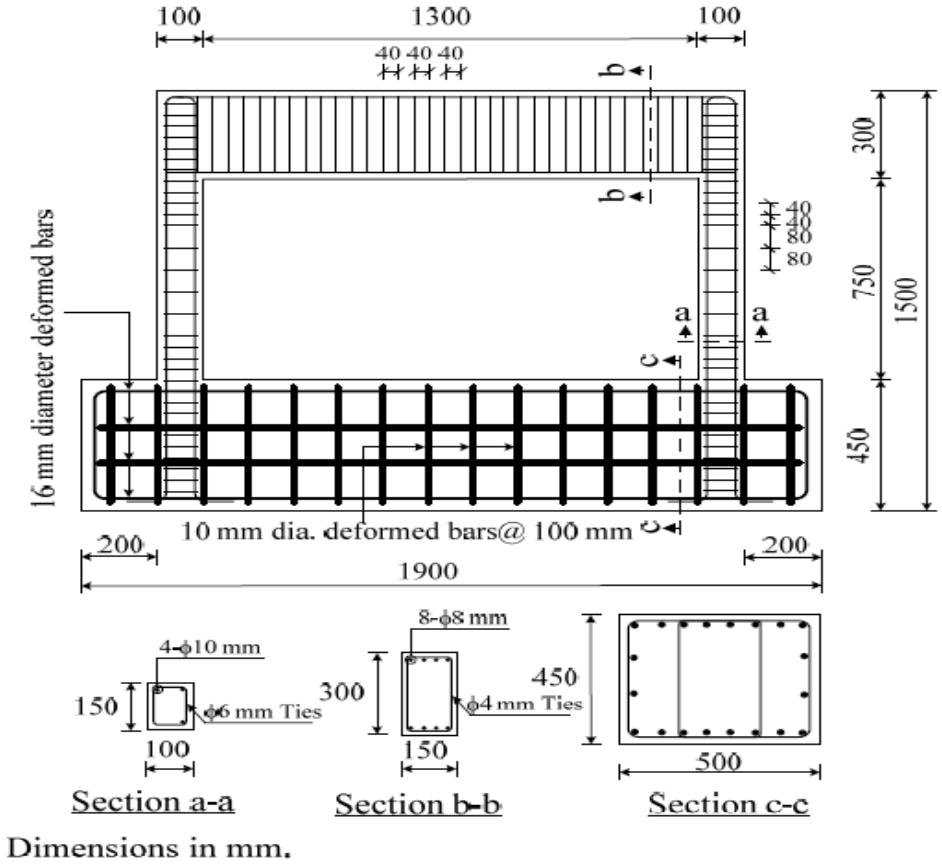

Figure 3.14: Reinforcement detail of RC frame (Anil & Altin, 2007)

The structure was modeled in 2D the same as Anil and Altin (2007). There are fiber element at the bottom of the column with fixed support. The upper side are the elastic elements and rigid elements at the connection of column and beam.

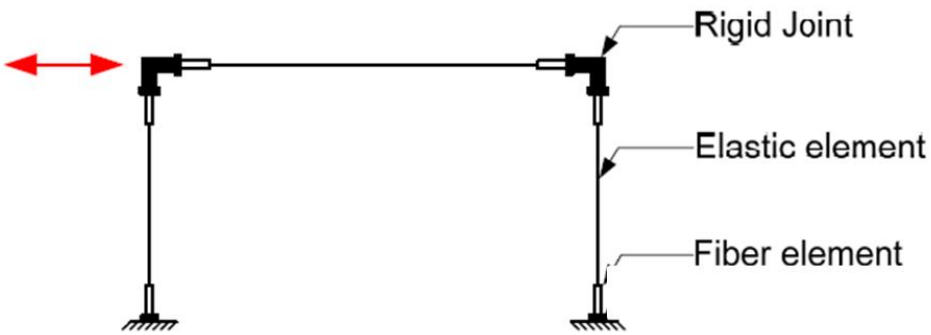

Figure 3.15: Structural model of the RC frame

3.4.2. Analytical results from OpenSees:

3.4.2.1. Stress-strain curve of the materials:

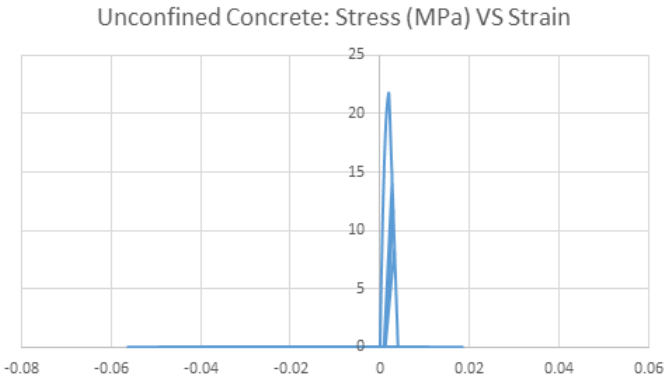

(a): Stress strain curve of the unconfined concrete of the frame's column

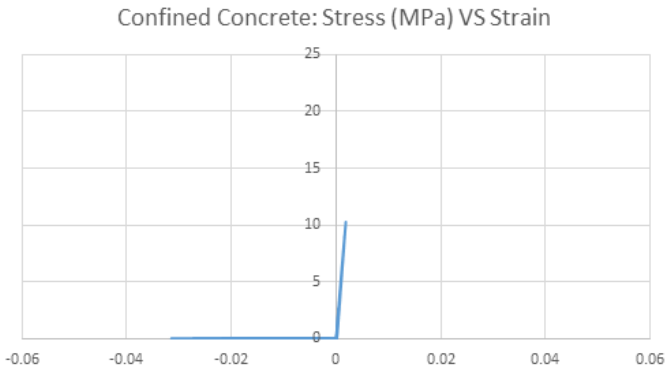

(b): Stress strain curve of the confined concrete of the frame's column

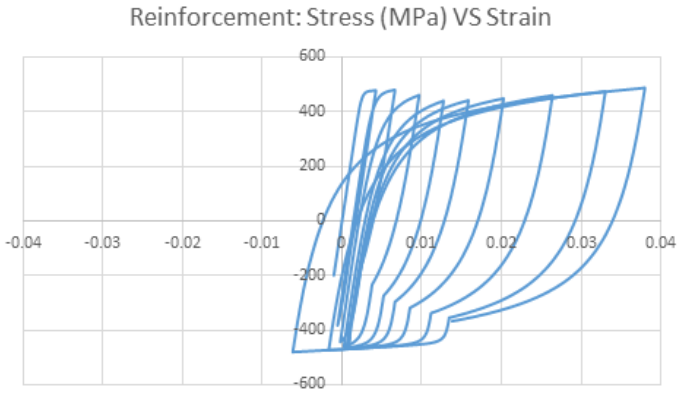

(c): Stress strain curve of the reinforcement of the frame's column

Figure 3.16: Stress-strain curve of the confined concrete, the unconfined concrete, and the reinforcement of the frame

3.4.2.2. Load – Displacement curve:

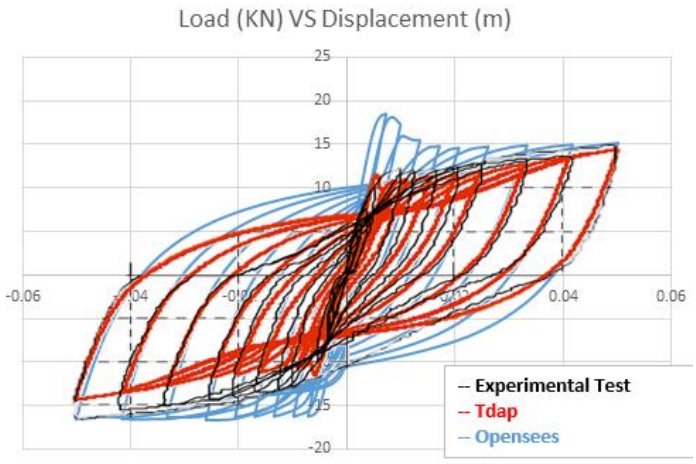

Figure 3.17: Load-displacement graph of the frame

The load-displacement curve is shown in figure above. As seen, the results from OpenSees might be a bit different from the experimental test and the TDAP model from Piyawat (2012). However, the result from OpenSees is still acceptable comparing to the two previous results.

3.5. Fiber modeling of the pile bent:

3.5.1. Geometry of the pile bent:

The target contains of 6 piles bent at both end of the bridge. The geometrical detail of the pile bent is as followed. The height is 7 meters and the width of the pile bent is 13 meters.

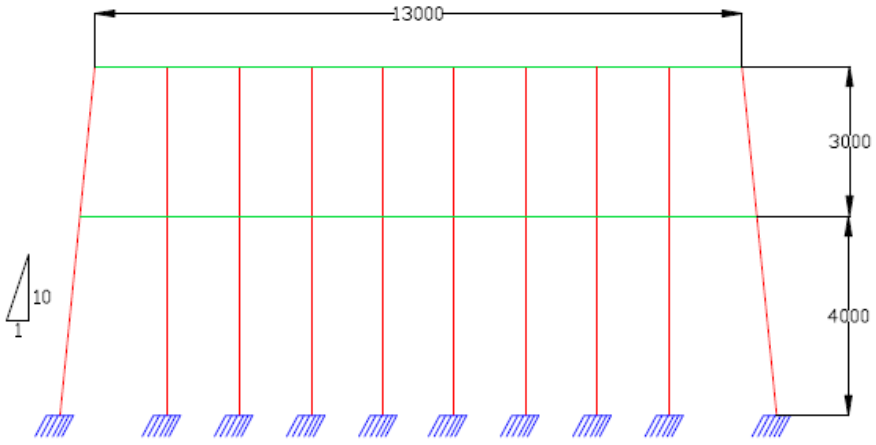

Figure 3.18: Geometry of the pile bent

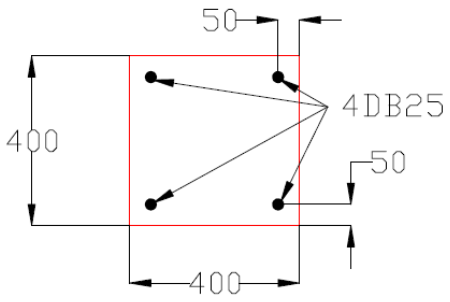

Figure 3.19: Detail of section of column and beam

The column and the beam of the pile bent are the same and with the same reinforcement as well.

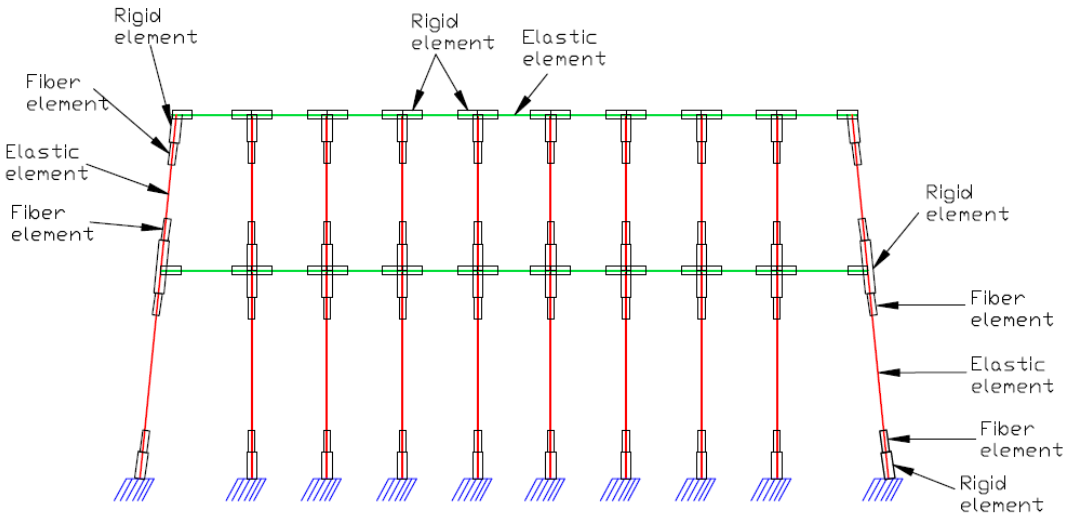

Figure 3.20: Model of pile bent

The column of the pile bent is separated into fiber element, elastic element, and rigid element while the beam is separated into elastic and rigid elements only. This is due to the applied direction of the ground motion.

On top of the pier, the load from girders was put. Half of left and right side of the girder load was calculated and lumped as masses there.

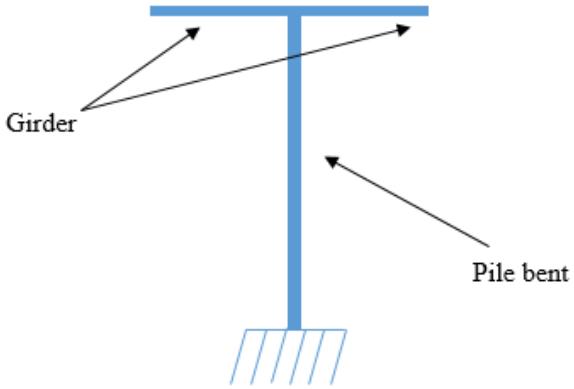

Figure 3.21: Side view of the pile bent

3.5.2. Analytical results:

3.5.2.1. Natural periods:

The natural periods of the pile bent were generated in OpenSees. Meanwhile, the structure was built in SAP2000 as well. Hand calculation based on assumption of SDF multiplying the number of column was calculated. The result was shown in table below.

T (OpenSees)	1.16 s
T (SAP2000)	1.26 s
T (Hand calculation)	1.36s

The difference of the natural periods between these three methods occurred because the structure was modeled in inelastic range with full elastic strength in some part but others were modeled in elastic range with reduction factors from ACI318-05 (0.7 in column and 0.35 in beam) in OpenSees, but in SAP2000 the model was built in elastic range with reduced strength of materials. It means the model in OpenSees was stiffer than in SAP2000, which made the natural period from OpenSees was less than from SAP2000.

3.5.2.2. Time-history displacement:

Both models were put under MAECHAN ground motion with PGA of 0.05G. The small PGA of ground motion was selected to not make the fiber structure yield so that the results can be compared.

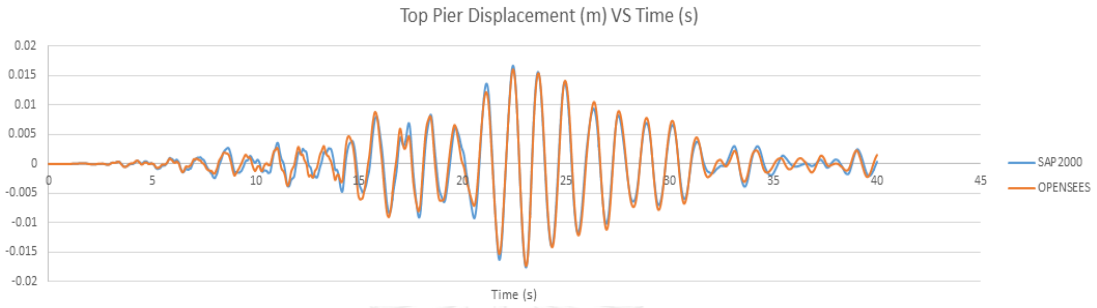

Figure 3.22: Time-history displacement on top of the pier under MAECHAN ground motion

There was a slight difference between both results. This is due to the small different stiffness of the model. However, the results from both analysis are acceptable.

3.5.2.3. Moment-curvature graph of fiber element:

The moment-curvature graph of the section was generated and plotted. The ground motion was changed with two options: 0.05G and 0.4G of PGA.

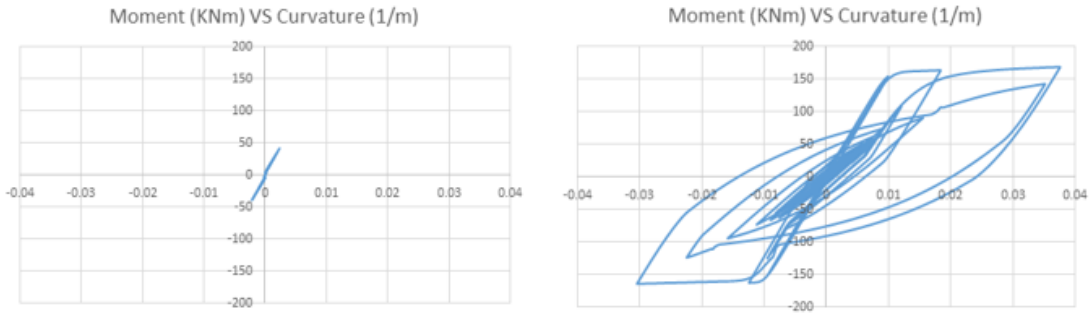

Figure 3.23: Moment-curvature of the 5th column of pile bent with 0.05G and 0.4G PGA of MAECHAN ground motion

The moment-curvature in the 0.05G was still elastic while in 0.4G ground motion, the section started yielding and gave the nonlinear curve.

In short, the structural modeling of the pile bent in OpenSees can be reliable.

3.6. Fiber modeling of the wall-type pier:

3.6.1. Geometry of the wall-type pier:

There are 12 wall-type piers in the bridge. The wall is 10.5m tall and 13m width. The wall is 0.9m thick with vide in the center. The cutting section of the wall is shown below.

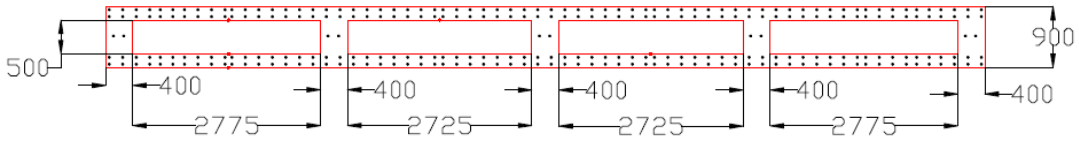

Figure 3.24: Cut section of the wall

The section was divided into 5 small sections. The column at both end were moved to get the I section. There are all in I shape and there are two kinds of I sections as shown as followed.

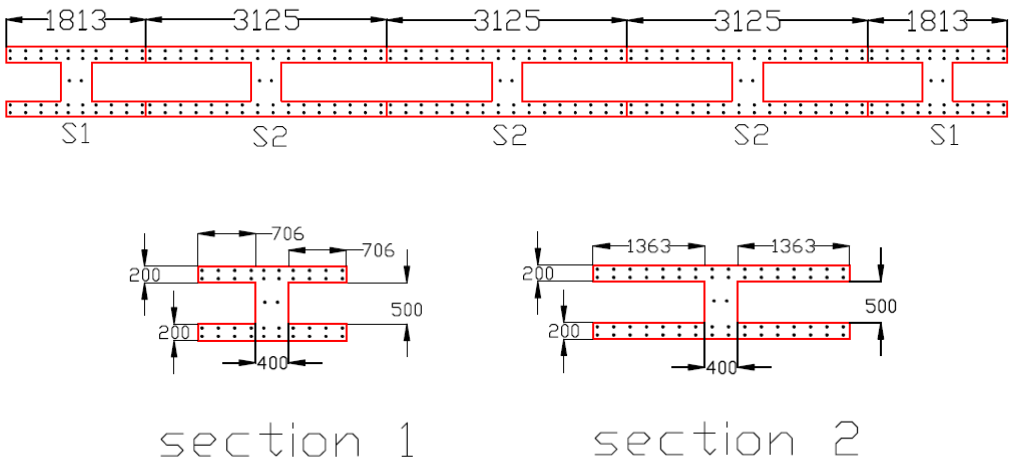

Figure 3.25: Division of sections

The wall structure was modeled as various columns and beams with only fiber section at the bottom of the column. This is because the structure is very stiff and the cracking of concrete and yielding of reinforcement might occur only at the bottom.

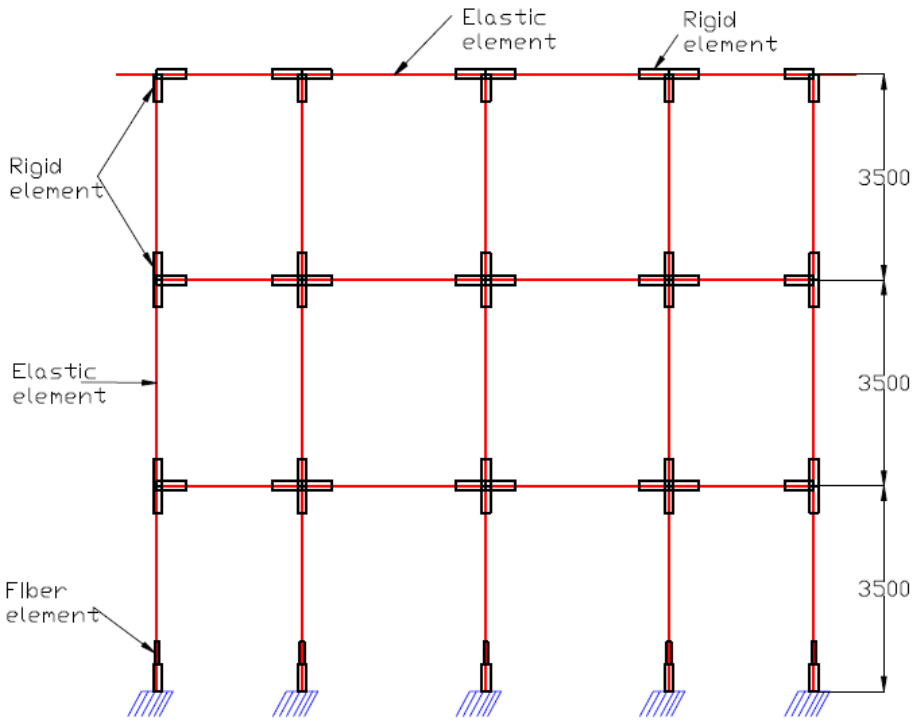

Figure 3.26: Structural model of wall-type pier

3.6.2. Analytical results:

3.6.2.1 Natural periods:

The natural periods of the pier in different computing methods are shown in table below:

T (OpenSees)	0.75 s
T (SAP2000)	0.80 s
T (Hand calculation)	0.89 s

The difference is because the fiber elements in OpenSees were modeled with fully section while in SAP2000, all elements were modeled with reduction factors. In hand calculation, the model was more flexible since there was not rigid elements but there was in OpenSees and SAP2000.

3.6.2.2. Time-history displacement:

Similar to the case of pile bent, both models were put under MAECHAN ground motion with PGA of 0.05G.

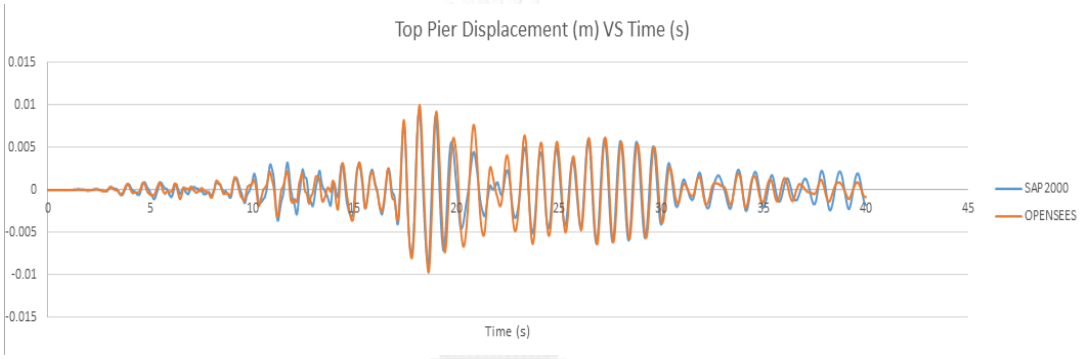

Figure 3.27: Time-history displacement on top of the pier under MAECHAN ground motion

As previous case, the slight difference between both results is due to the small different stiffness of the model. However, the acceptable results are verified.

3.2.2.3. Moment-curvature graph of fiber element:

The moment-curvature graph of the section was generated and plotted. The ground motion was changed with two options: 0.05G and 0.4G of PGA.

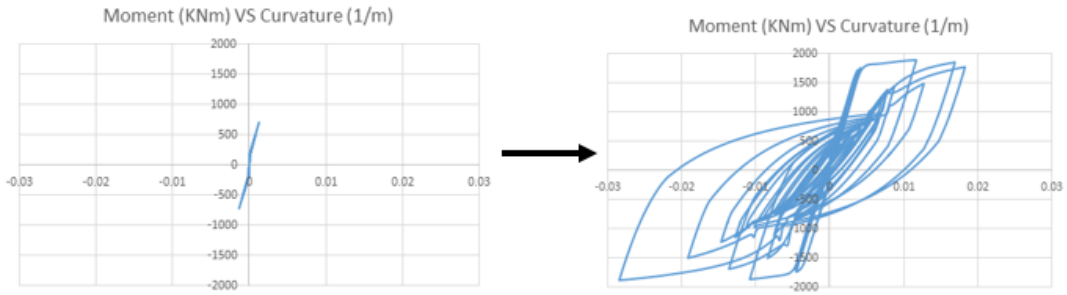

Figure 3.28: Moment-curvature of the 5th column of wall-type pier with 0.05G and 0.4G PGA of MAECHAN ground motion

The moment-curvature in the 0.05G was still elastic while in 0.4G ground motion, the section started yielding and gave the nonlinear curve.

In short, the structural modeling of the wall-type pier in OpenSees can be reliable.

3.7. Fiber modeling of MAE LAO Bridge:

3.7.1. Elastic modeling of bridge's girders:

3.7.1.1. Elastic modeling of bridge's girders on pile bents:

There is only slab girders on the pile-bent piers and the slab girders were modeled as numerous rectangular girders.

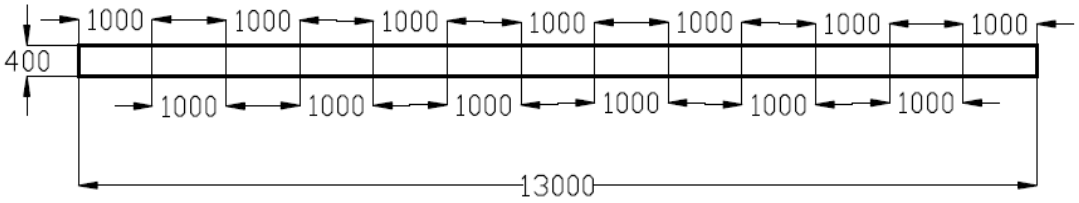

Figure 3.29: Geometry of slab girders

The girders were modeled as elastic beam element with section of 1m x 0.4m with span length between piers.

3.7.1.2. Elastic modeling of bridge's girders on wall-type piers:

On the wall-type piers, there are 13 box girders with the span length of 20m. The box girder has the geometry of 1m x 1m. There is a hole in the middle of girder with the length and width of 0.36m x 0.63m.

Therefore, the area of the girder is $A = 1 \times 1 - 0.63 \times 0.36 = 0.7732 m^2$

Therefore, the volume of the girder in 20m is $V = 0.7732 \times 20 = 15.464 m^3$

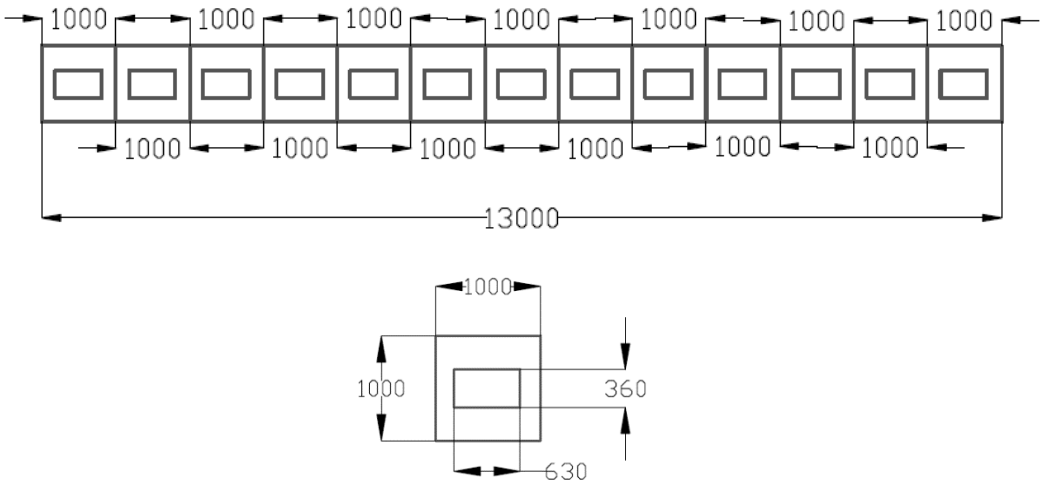

Figure 3.30: Geometry of box girders

Same to slab girders, the box girders were modeled as elastic elements with calculated properties.

3.7.2. Fiber modeling of the whole bridge:

The bridge is composed of three pile-bent piers at both end and twelve wall-type piers. All piers are connected to each other by girders of which there are 13 per span.

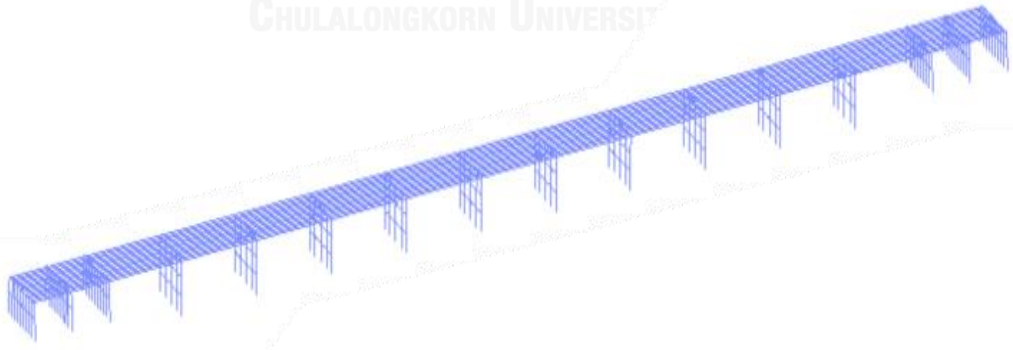

Figure 3.31: Structural model of MAE LAO Bridge in OpenSees

3.7.3. Analytical results:

3.7.3.1. Natural periods:

The full model of the bridge were modeled in OpenSees and SAP2000 and the natural periods were computed and shown below:

T (OpenSees)	0.75 s
T (SAP2000)	0.80 s

The different periods are because all elements in the model in SAP2000 are all reduced by recommended factors while, in OpenSees, some parts of the structure are in full section.

3.7.3.2. Time-history displacement:

Both models were put under the MAECHAN ground motion with PGA of 0.05G and 0.4G. The displacement on top of the pile-bent and wall-type piers in term of time was generated.

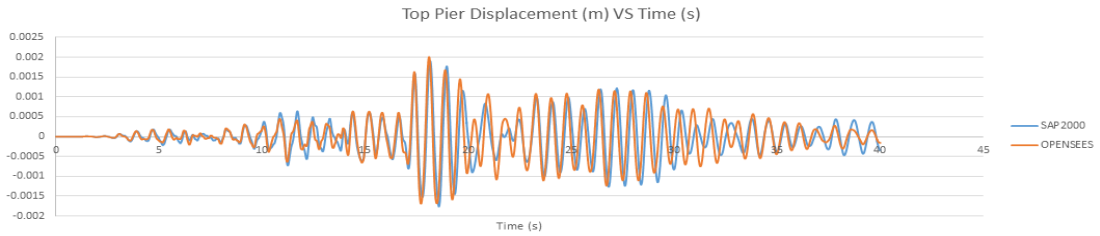

(a) Time-history displacement on top of pier 1

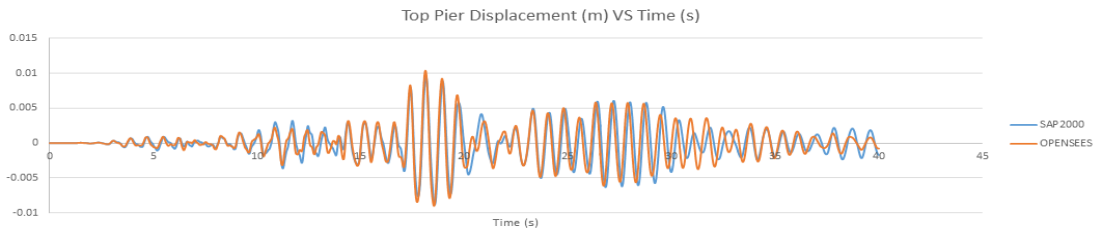

(b) Time-history displacement on top of pier 4

Figure 3.32: Time-history displacement on top of piers in term of time in MAECHAN ground motion of 0.4G PGA

The displacements in term of time were recorded and plotted. As a result, the displacements from both programs are quite similar and acceptable. The displacement from OpenSees is a bit bigger than from SAP2000 in case of peak point of ground motion because at this stage of time, the fiber materials started yielding and gave nonlinear properties. Meanwhile, at other stage of time where the materials do not yield, the displacement from SAP2000 is slightly more than from OpenSees since the model in SAP2000 is more flexible in elastic range than in OpenSees.

In short, the accuracy of the model in OpenSees can be verified.

3.8. Modeling of elastomeric bearing:

The elastomeric bearing is one of many isolators used to increase bridge's performances. In the model, the elastomeric bearing is in elastic range. Properties of the bearing were calculated.

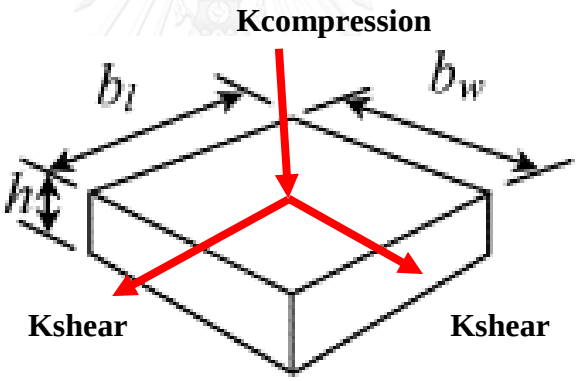

Figure 3.33: Property of elastomeric bearing

The formulas for calculating the stiffness of bearing in horizontal and vertical directions are proposed by Priestley (1996):

$$K_{compression} = \frac{6G_{shear} \times S^2 \times A \times G_{bulk}}{\left(6G_{shear} \times S^2 + G_{bulk}\right) \times T}$$

$$K_{shear} = \frac{G_{shear} \times A}{T}$$

Where: $S = \frac{A'}{A}$

The bending stiffness of bearing is modeled as hinge with high stiffness in all three directions.

The size of bearing is chosen to be 0.3m X 0.4m with various height.

The shear modulus of bearing $G_{shear} = 0.9MPa$

The bulk modulus of bearing $G_{bulk} = 2000MPa$

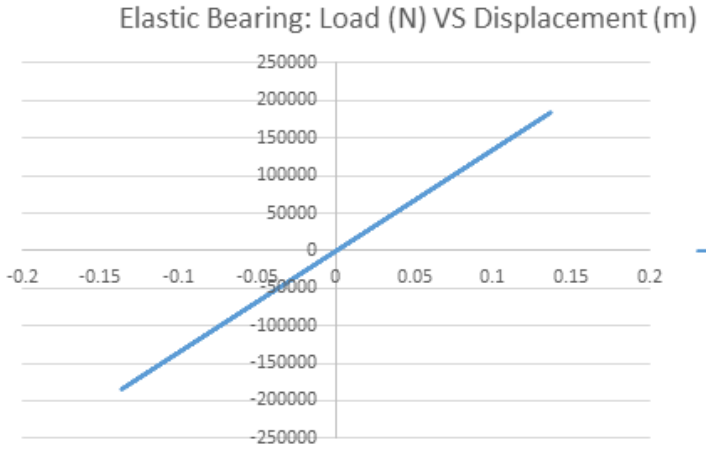

Figure 3.34: Load-displacement curve of elastomeric bearing in horizontal direction

The elastomeric bearing is modeled as elastic material. However, the real elastomeric bearing is not the same height as the model because inside the bearing there are steel plates as well. The steel plate height is approximately about 3.5mm while the bearing slide is about 10mm.

Table 3.4: Real elastomeric bearing height

Rubber Height (mm)	Steel Plate Number	Steel Plate Total height (mm)	Bearing Total Height (mm)
20	1	3.5	23.5
40	3	10.5	50.5
60	5	17.5	77.5
80	7	24.5	104.5

3.9. Modeling of shear dowels:

Shear dowel is a steel bar embedded between piers and girder of the bridge. The usage of this kind of structure is to help prevent unseating phenomenon and also help in dissipating energy from bridge structures. Therefore, the dowel must not too stiff to not yield at all during the application of ground motion.

3.9.1. Fiber modeling of steel bar:

Since the dowel is located between the girders and the top of the pier, the top and bottom of the dowel are considered to be fixed. The height of dowel is also the same as the bearing's height.

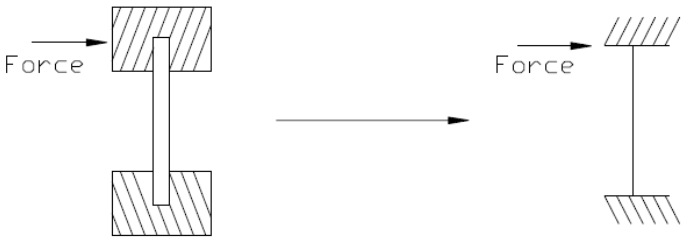

Figure 3.35: Structural model of steel bar

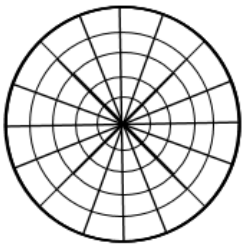

Figure 3.36: Fiber section of steel bar

The circular section of the steel bar were divided into many small sections. The variation of dowel height and dowel area to investigate the yielding strength to selection the most appropriate dowel for each case study.

Table 3.5: Parameters of shear dowel

Yielding strength of steel bar according to its diameter		
D=10mm	D=12mm	D=25mm
400 Mpa	400 Mpa	400 Mpa

3.9.2. Verification of shear dowel model:

3.9.2.1. The appropriate number of fiber section:

Tension and Pushover Test of a steel bar are done with different number of fiber element in section.

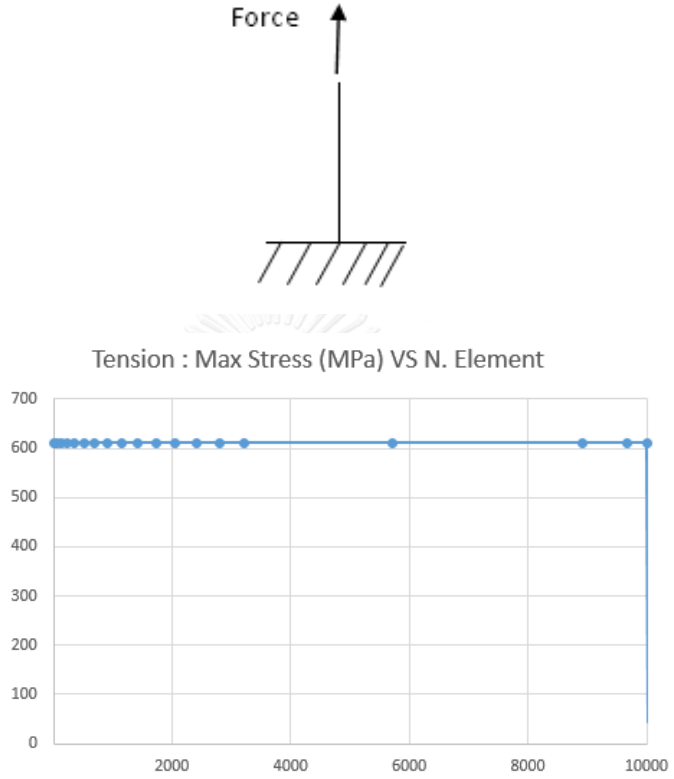

(a): Maximum stress in function of number of fiber

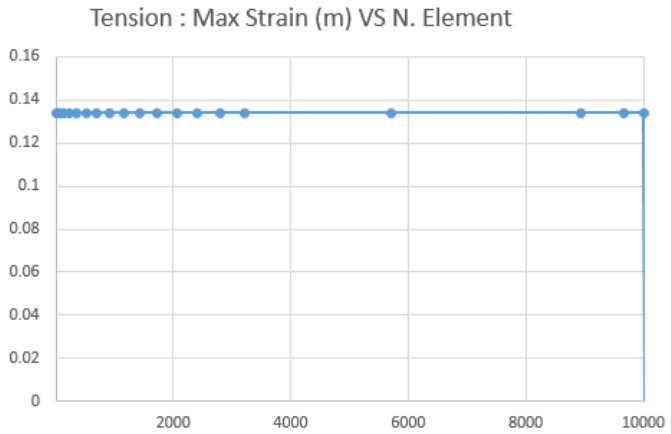

(b): Maximum strain in function of number of fiber

Figure 3.37: Maximum stress and strain of the steel bar in tension loading

Both stress and strain of the element are the same no matter how many fiber element it has. This is because for tension, the stress and strain of the section does not related to the section size, it depends only with Young Modulus, which was set to be fixed 200 GPa.

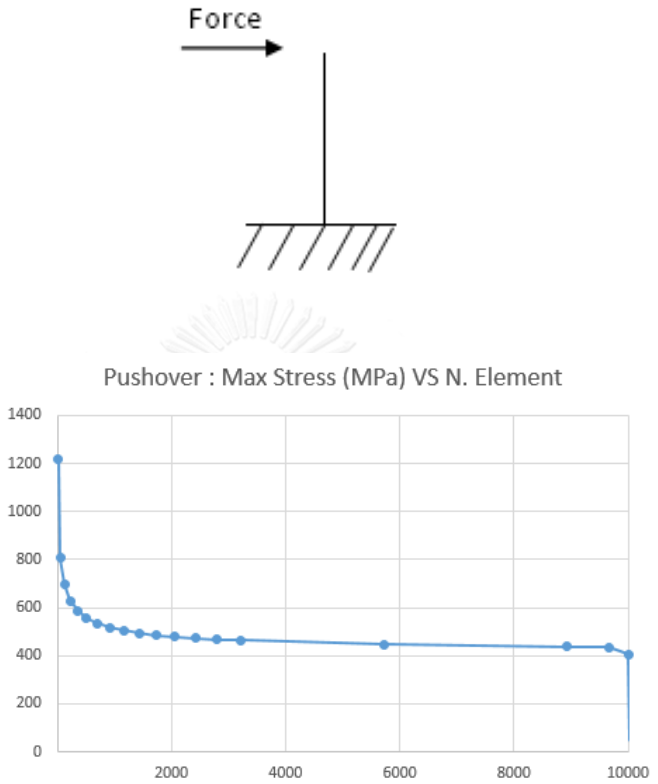

(a): Maximum stress in function of number of fiber

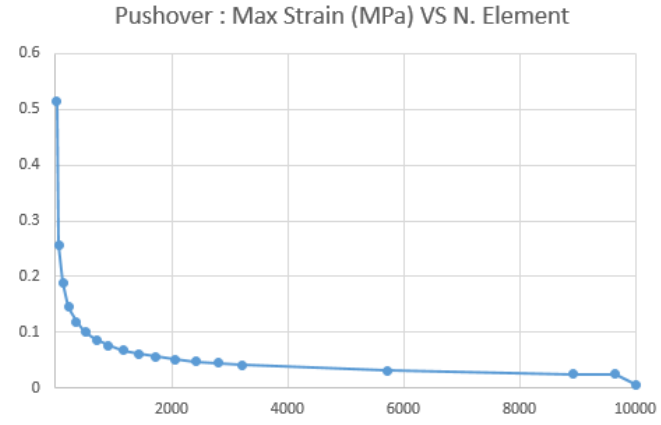

(b): Maximum strain in function of number of fiber

Figure 3.38: Maximum stress and strain of the steel bar in lateral loading

Both stress and strain converge in parabolic shape toward 10000 fibers that error happens. This convergence is caused by the shear modulus, which is in function of area of section.

Conclusion: From graph, **6000 to 7000 fibers** in one section can provide good analytical result already.

3.9.2.2. The displacement on top of the steel bar:

- **Tension Test:**

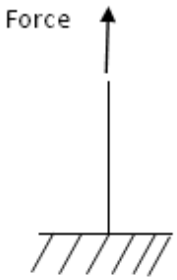

Provided a small force, which will not cause the section to yield, the displacement must agree with that of hand calculation.

+ In case of $F = 50KN, L = 0.15m$

$$A = \frac{\pi d^2}{4} = \frac{3.14 \times 0.025^2}{4} = 4.90625 \times 10^{-4} m^2 \rightarrow K = \frac{AE}{L} = 654.167MN/m$$

$$\rightarrow \Delta = \frac{F}{K} = \frac{50KN}{654.167MN/m} = 0.0000764m = \Delta_{opensees}$$

+ In case of $F = 100KN, L = 0.15m$

$$\rightarrow \Delta = \frac{F}{K} = \frac{100KN}{654.167MN/m} = 0.000153m = \Delta_{opensees}$$

- **Pushover Test:**

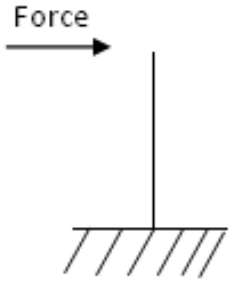

Provided a small force, which will not cause the section to yield, the displacement must agree with that of hand calculation.

+ In case of $F = 4KN$, $L = 0.15m$

$$A = \frac{\pi d^2}{4} = \frac{3.14 \times 0.025^2}{4} = 4.90625 \times 10^{-4} m^2$$

$$\rightarrow K = \frac{3EI}{L^3} = 3.407 MN/m$$

$$\rightarrow \Delta = \frac{F}{K} = \frac{4KN}{3.407 MN/m} = 0.001174m = \Delta_{opensees}$$

3.9.2.3. The transformation to the model with fixed-end at both side:

The model of fix-free was verified to be correct but our shear dowel is not fix-free structure. It ought to be fix-fix one. Now, the model is transformed into fix-fix one.

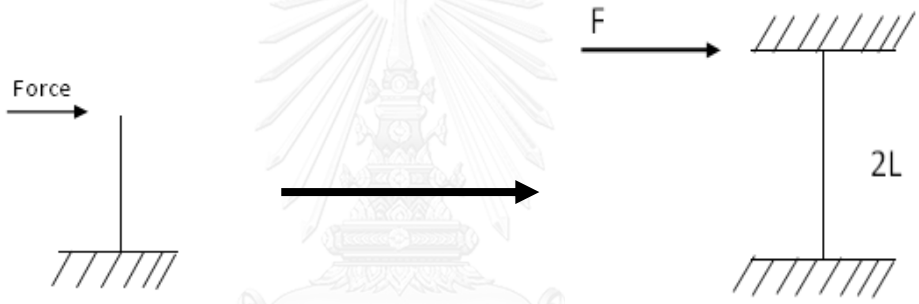

Figure 3.39: Transformation to fix-fix steel bar model

The new model is with length of 2L and fix at another end. This model must provide a result of the same shear force and 2 times of displacement.

Since in first case, the displacement is $\Delta_1 = \frac{F}{K} = 0.001174m$

Applying the same force, $\Delta_{opensees} = 0.002348m = 2\Delta_1$

Therefore, the shear dowel is verified!

3.9.3. The assumption of the shear dowel model:

The cyclic loading was applied to the shear dowel fiber dowel and the hysteresis loop of the load-displacement curve was obtained. Therefore, the assumption for the bilinear model to be put in the full bridge model was made because it was incapable to use the full fiber model of the shear dowel for its taking too much time for the analysis.

Below is the result obtained from the steel bar with 0.08m height and 0.0025mm diameter. The yielding strength is 400 MPa.

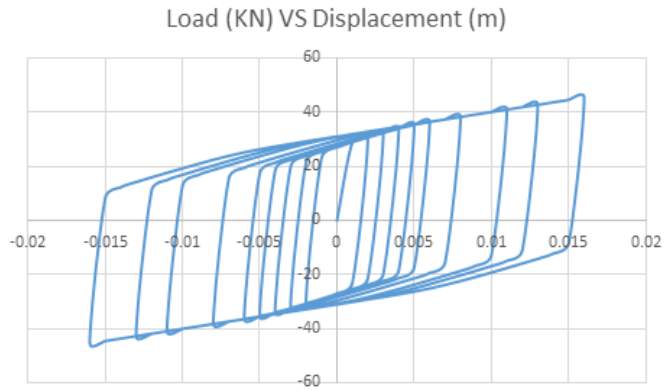

Figure 3.40: The hysteresis loop of load-displacement curve of the shear dowel fiber model

The bilinear model of the shear dowel was made as the figure below:

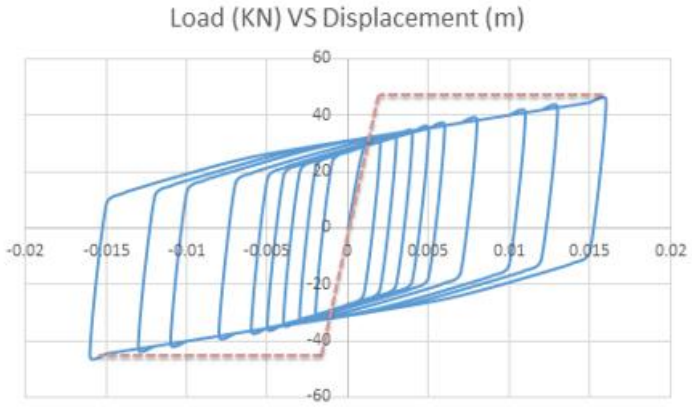

Figure 3.41: The bilinear model assumption of the shear dowel

The dash line is the bilinear model of the shear dowel to be used. The initial stiffness was obtained and the yielding force was assumed to be equal to the ultimate strength.

3.10. Structural modeling of elastomeric bearing and shear dowels:

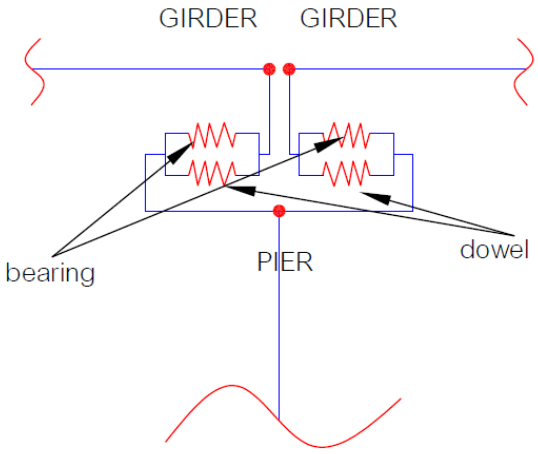

Figure 3.42: Structural modeling of elastomeric bearing and shear dowel connected to the structural elements

The elastomeric bearings and shear dowels are modeled with link element containing two spring stiffness connected from the pier to two sides of girders. The girders are two separated elements and are connected to the same pier with two different link elements of the bearing and shear dowels.

3.11. Abutment soil spring stiffness:

In the target bridge, the width of back wall is 13m, and abutment height is equal to the pier, which is 7m. Therefore, the formula is:

$$K_{abut} = \frac{11.5KN/mm}{m} \times 13m \times \frac{7m}{1.7m} = 615.588KN/mm$$

Then distribute the stiffness of the abutment to each of 13 girder connection.

So we get $$K_{abut,each} = \frac{615.588KN/mm}{13} = 47.35KN/mm$$

The abutment stiffness was applied to the top of the piers at both end. Also, the abutment stiffness will be added to the model for only the cases of 6cm and 8cm-thick bearing since they are the most significant according to the performance description in the previous part. In addition, only the strong ground motion is chosen to apply to the structure. They are MAECHAN and MAESAI ground motion. However, since the

stiffness is very large, the reduction of the stiffness while applying to the model is included with the reduction factor of 25%, 50% and 100%.

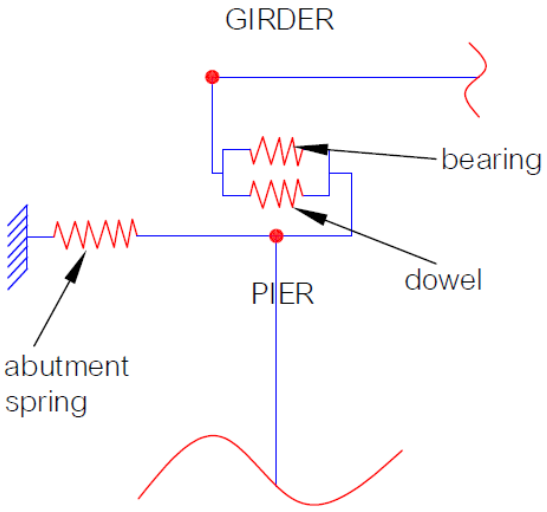

Figure 3.43: Structural modeling of abutment together with the pier and girder

3.12. Ground motions:

There are three different ground motions used in this research. They are MAECHAN ground motion, MAESAI ground motion, and PHAYAO ground motion. The following sections are details of these three ground motions.

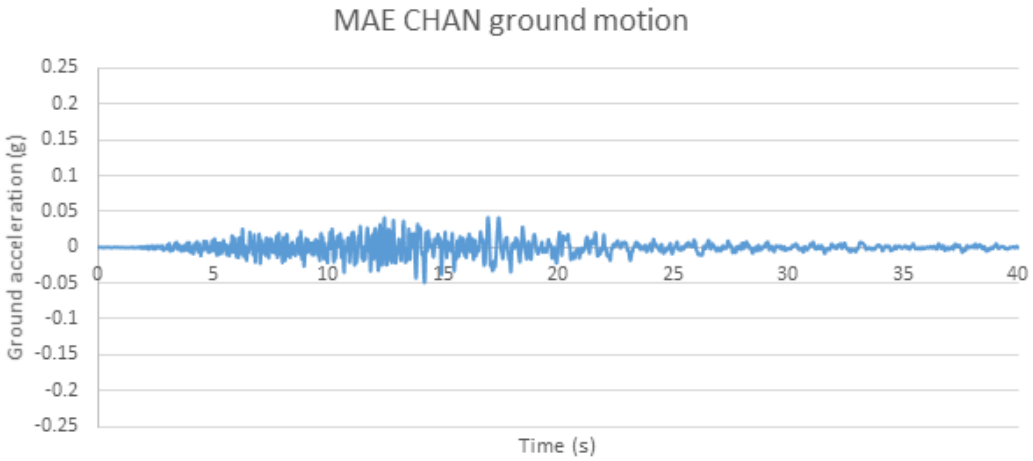

Figure 3.44: MAECHAN time-history ground acceleration

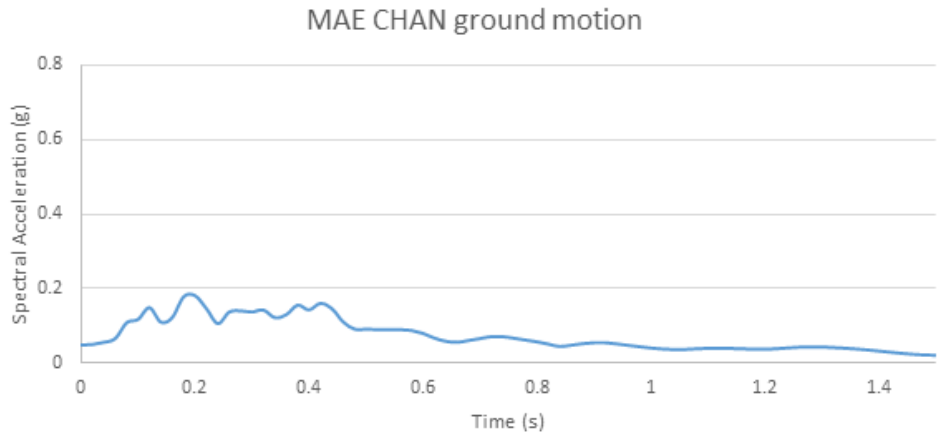

Figure 3.45: MAECHAN spectral acceleration

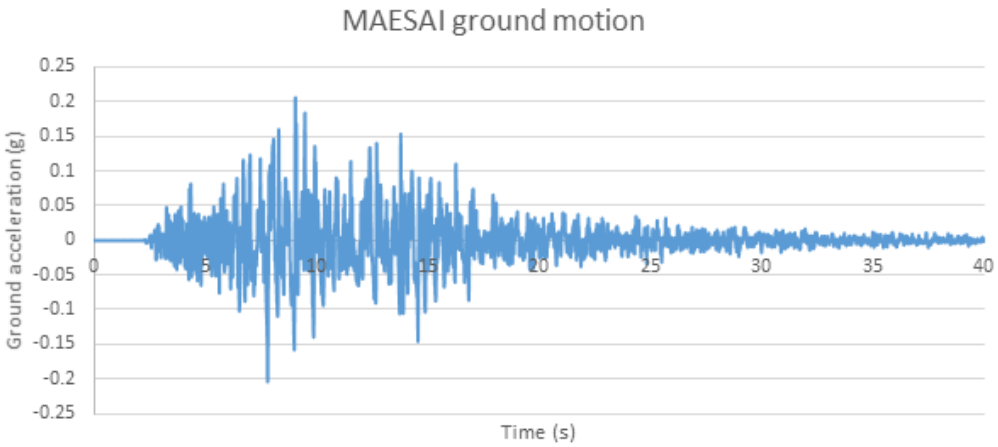

Figure 3.46: MAESAI time-history ground acceleration

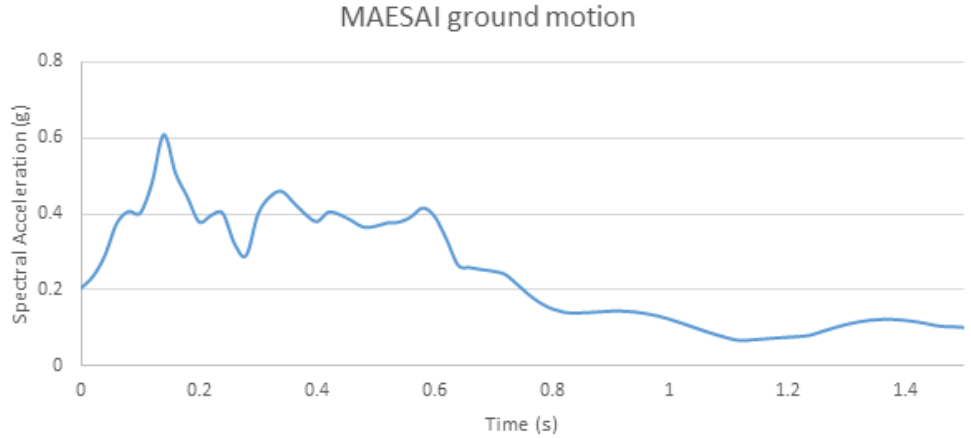

Figure 3.47: MAESAI spectral acceleration

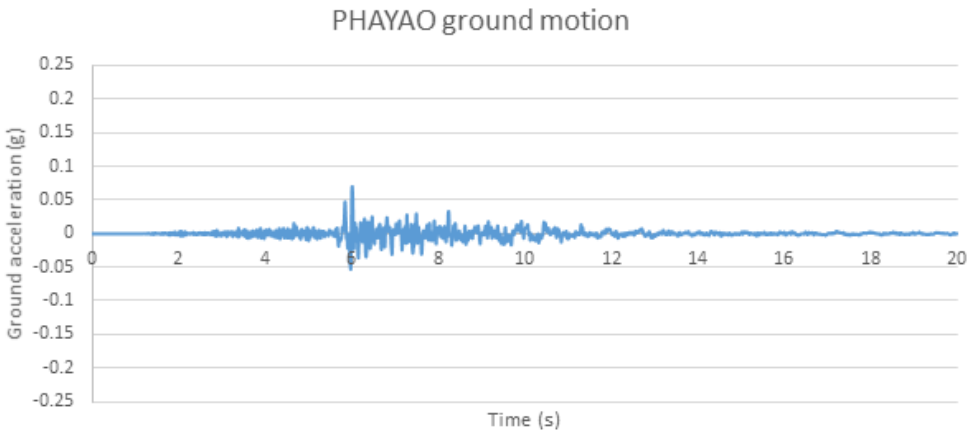

Figure 3.48: PHAYAO time-history ground acceleration

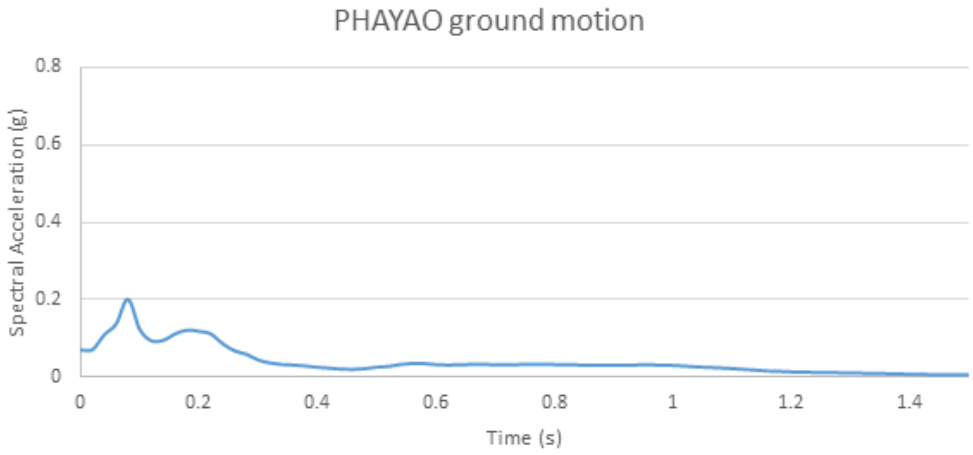

Figure 3.49: PHAYAO spectral acceleration

The model of MAE LAO Bridge was analyzed and the natural period of the bridge was at 0.75s. However, after the installation of elastomeric bearing to the bridge model, the range of natural period is between 0.85s for 0.02m thick bearing and 1.05s for 0.08m thick bearing. The following graphs of spectral accelerations are scaled to PGA of 0.4g.

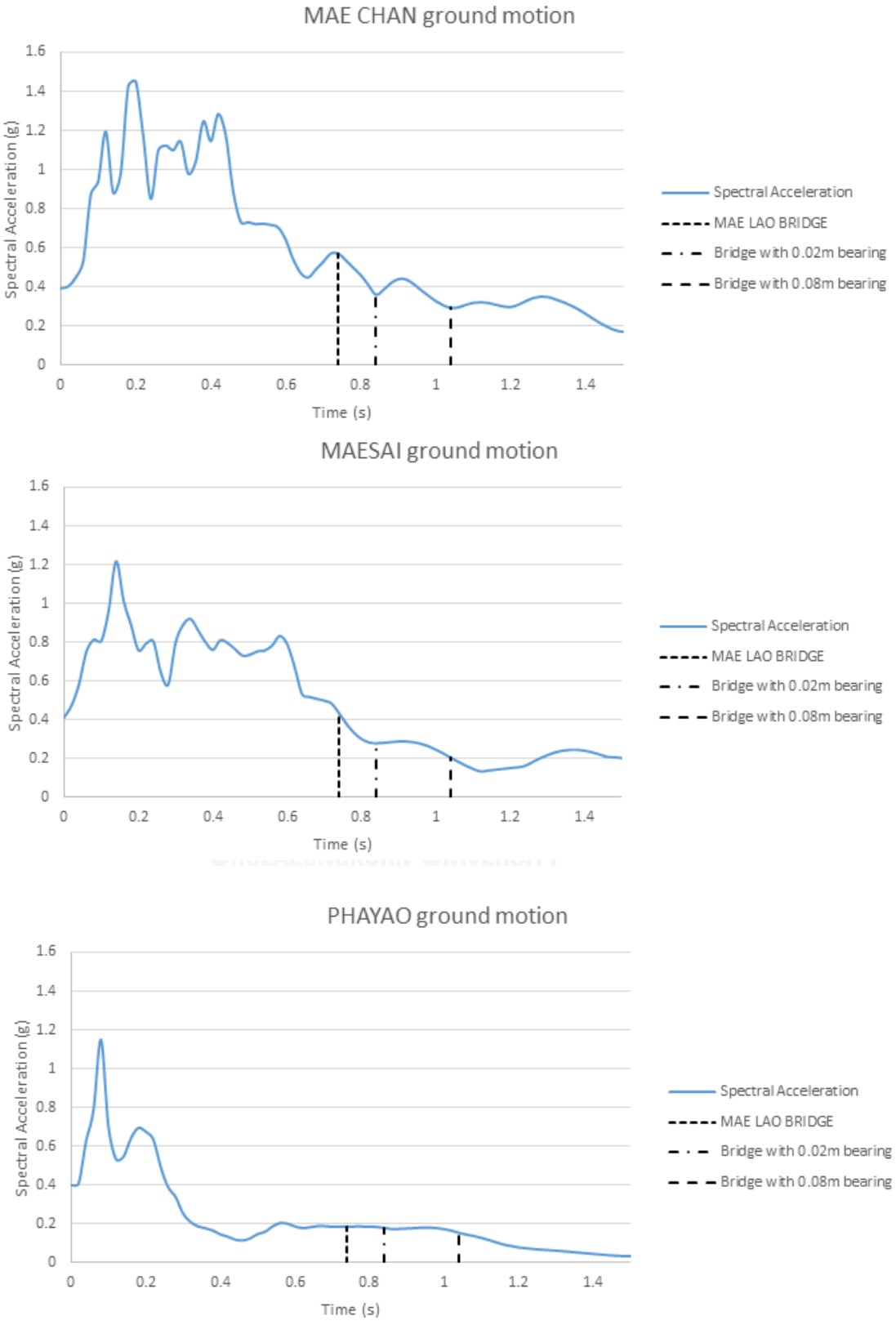

Figure 3.50: Spectral acceleration of each ground motion at PGA of 0.4g

The seismic demand of all three ground motion is different. For MAECHAN ground motion, the demand is reduced from 0.6g in case without bearing to about 0.3g. For MAESAI ground motion, the demand also is reduced from 0.4g in case without bearing to about 0.2g in case with 8cm-thick bearing. Also, the last ground motion, PHAYAO ground motion, which has the smallest spectral acceleration if comparing with other two ground motions, also is reduced from 0.2g in case without bearing to 0.16g in case with 8cm-thick bearing. As above, the demanding in these three ground motion is reduced after the installation of bearing especially the one with 8cm-thick bearing.

The figures above show the spectral acceleration of each type of structures including bridge without bearing and with different thickness of bearing. As shown, MAECHAN ground motion gives the strongest acceleration among the three at around 0.6g with bridge model without bearing. The next is MAESAI ground motion, which is about 0.4g and the weakest acceleration is given by PHAYAO ground motion with PGA of 0.2g only.

The three ground motion is considered to be enough for the analysis in this study because these three ground motions were ones of the strongest ground motion ever recorded in the area. Also, the ground motions are considered to be strong enough for the structural damage.

CHAPTER 4 : ANALYTICAL RESULTS

This chapter is about to show the results obtained from the previous chapter. All data were computed by the computational program OpenSees only. There are THREE ground motions chosen to be applied to the model: MAE CHAN ground motion, MAE SAI ground motion, and PHAYAO ground motion. In addition, all three ground motions are scaled with different PGA (Peak Ground Acceleration) including 0.2g, 0.4g, and 0.6g.

The analysis includes four important elements:

- **Material level**: the stress-strain of unconfined, confined concrete and reinforcement
- **Cross sectional level**: the moment-curvature graph of the fiber section
- **Structural level**: the load-deflection curve of the structure

Many cases are to be analyzed. There are four parameters to study: 2cm, 4cm, 6cm, and 8cm thickness of bearing. Meanwhile, there are three different ground motions which are MAECHAN, MAESAI, and PHAYAO ground motion with different PGA of 0.2g, 0.4g, and 0.6g. Totally, there are 36 cases. On the other hand, these cases will be twice when we separate them in case with soil spring and without soil spring. So, there are 72 cases. In addition, the introduction of the shear dowel to the model is added which means there are 144 cases in total.

However, some cases must be deleted since the analysis takes time and the obtained may not be interesting such as in cases of 0.2g and 0.4g of PGA of PHAYAO ground motion where the elements are still in elastic range in all cases of variation of bearing thickness and in cases of 0.6g of PGA of PHAYAO ground motion where they slightly yielded. Also, the cases of 2cm and 4cm-thick bearing does not have much effect in helping the structure to perform better so these will be eliminated as well. The below is the table of summary of cases needed to be analyzed.

Table 4.1: Summary of all cases to be analyzed and discussed

		PGA of ground motion		Bearing thickness
Case of Elastomeric bearing	without abutment soil spring stiffness	MAECHAN EQ	0.2g	2cm
				4cm
				6cm
				8cm
			0.4g	2cm
				4cm
				6cm
				8cm
			0.6g	2cm
				4cm
				6cm
				8cm
		MAESAI EQ	0.2g	2cm
				4cm
				6cm
				8cm
			0.4g	2cm
				4cm
				6cm
				8cm
			0.6g	2cm
				4cm
				6cm
				8cm
		PHAYAO EQ	0.2g	2cm
				4cm
				6cm
				8cm
			0.4g	2cm
				4cm
				6cm
				8cm
			0.6g	2cm
				4cm
				6cm
				8cm
	With abutment soil spring stiffness	MAECHAN EQ	0.4g	6cm
				8cm
			0.6g	6cm
				8cm
		MAESAI EQ	0.4g	6cm
				8cm

			0.6g	6cm	
				8cm	

		PGA of ground motion		Bearing Thickness	Dowel diameter
Elastomeric bearing and shear dowel	without abutment	MAECHAN EQ	0.4 g	8cm	10mm
				8cm	12mm
				8cm	25mm
			0.6 g	8cm	10mm
				8cm	12mm
				8cm	25mm
		MAESAI EQ	0.4 g	8cm	10mm
				8cm	12mm
				8cm	25mm
			0.6 g	8cm	10mm
				8cm	12mm
				8cm	25mm

In the case of elastomeric bearing and shear dowel, the application of abutment soil spring stiffness to the model is neglected since the focus of the study is on the effect of shear dowel to the structure.

4.1. The bridge with elastomeric bearing:

4.1.1. The bridge without abutment soil spring:

The bridge was modeled in 3D with ground motion only applied to longitudinal direction. The results are plotted in many different type of graphs including time-history displacement on top of the pier, moment-curvature curve, and time-history bearing displacement. Since there are so many columns and piers to be investigated, there are also graphs of summary of data showing the maximum value in pier and bearing displacement.

There are 18 different piers for the whole bridge with different number of columns at pile-bent type and wall type. Only four piers are chosen to show here. They are:

1. The first pier at the beginning of the bridge
2. The third pier which is the last pile-bent pier connected to the wall-type pier
3. The fourth pier which is the first wall-type pier connected from the pile-bent pier
4. The ninth pier which is the wall-type pier located in the middle of the bridge.

Also, since the bridge is symmetric longitudinally, the performance of the pier is the same between the left side and the right side.

4.1.1.1. Natural period of the bridge:

The natural period of the bridge is calculated with OpenSees. The natural period in case with and without elastomeric bearing is shown in the table below:

Table 4.2: Natural period of the bridge model

Cases	Natural Periods (s)
Bridge without elastomeric bearing	0.74
Bridge with 2cm-thick bearing	0.82
Bridge with 4cm-thick bearing	0.89
Bridge with 6cm-thick bearing	0.96
Bridge with 8cm-thick bearing	1.02

The natural period of the bridge elongates from 0.74s in case without elastomeric bearing to 1.02s in case with 8cm-thick bearing. The elongation is about 10% in case of 2cm-thick bearing to 38% in case of 8cm-thick bearing. This kind of elongation helps reduce up to 50% the seismic demand of the structure according to the spectral acceleration graph in section 3.11.

4.1.1.2. Time-history displacement on top of the pier:

- 0.4G of PGA of MAECHAN ground motion:

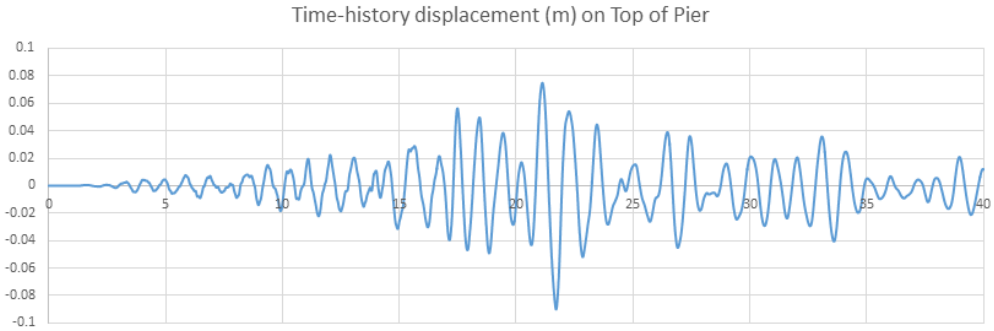

(a) Time-history displacement of pier1

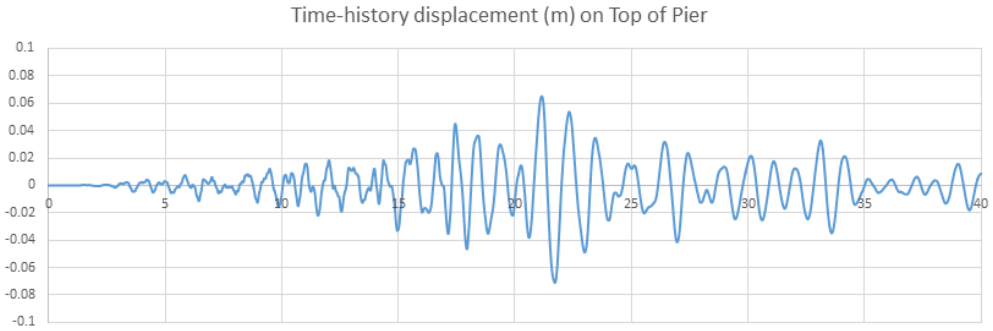

(b) Time-history displacement of pier3

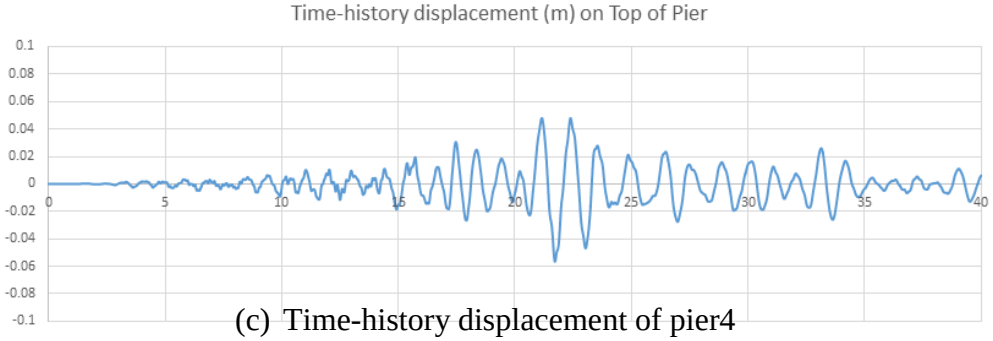

(c) Time-history displacement of pier4

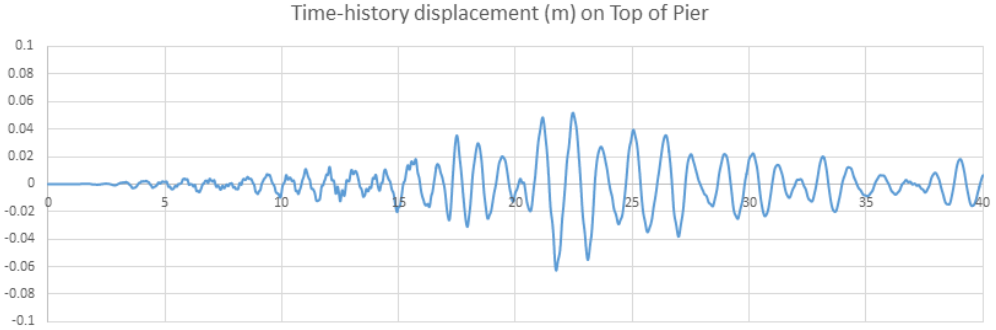

(d) Time-history displacement of pier9

Figure 4.1: Time-history displacement (m) on top of Pier1, Pier3, Pier4, and Pier9 in case of 6cm-thick bearing

The time-history displacement of all four piers is in the same trend where it reached its maximum displacement in the time of 20s to 25s. In the figure, the displacement of pier1 has the biggest scale. This is because it is at the end of the bridge where there is not abutment to support it. Therefore, its displacement is much bigger than others. The maximum displacement is 0.09m, 0.07m, 0.056m, and 0.06 in the pier1, 3, 4, and 9 respectively.

4.1.1.3. Time-history girder displacement:

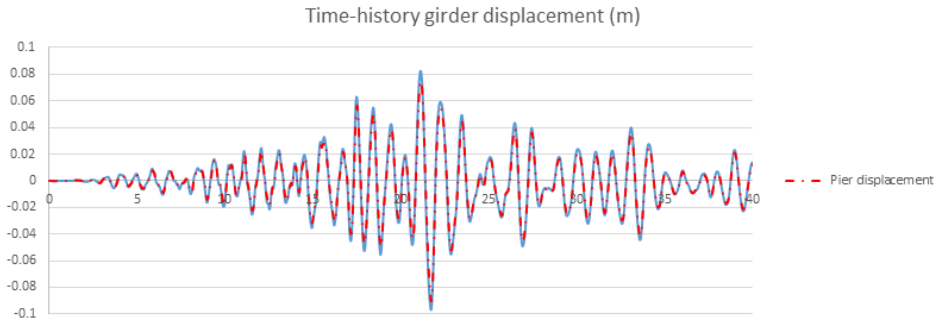

(a) Time-history girder displacement of pier 1

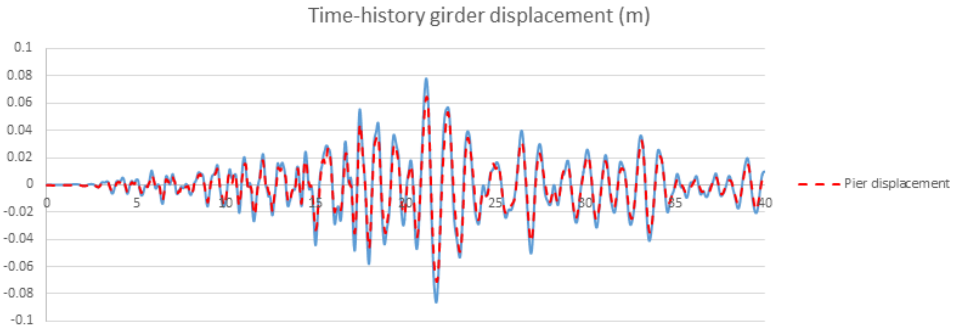

(b) Time-history girder displacement of pier 3

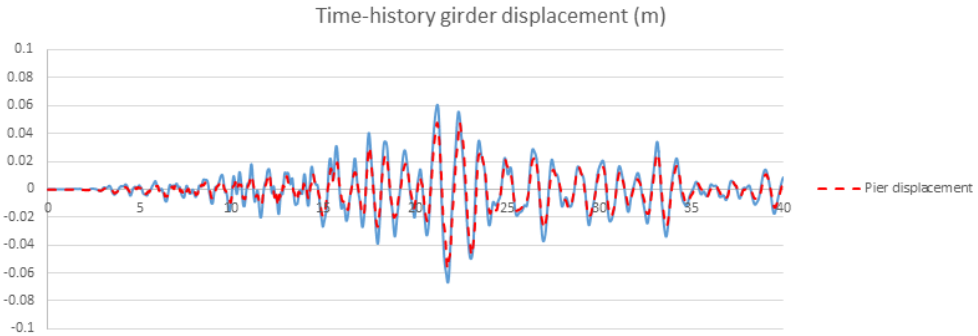

(c) Time-history girder displacement of pier 4

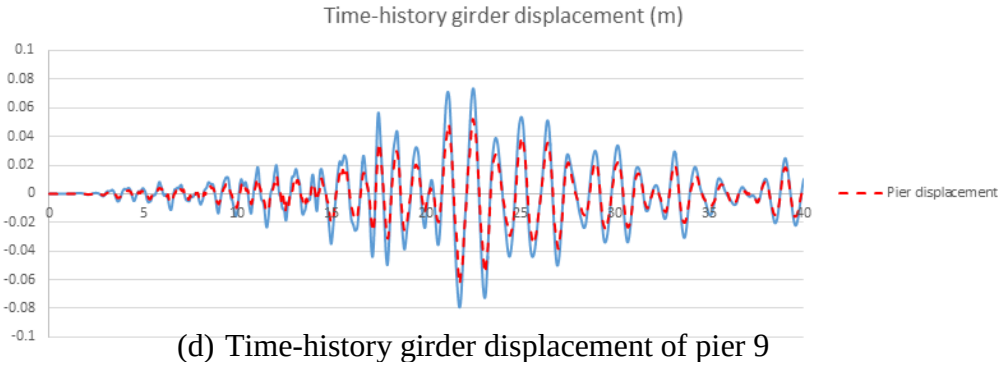

(d) Time-history girder displacement of pier 9

Figure 4.2: Time-history girder displacement (m) of Pier1, Pier3, Pier4, and Pier9 in case of 6cm-thick bearing comparing to the pier displacement in dash line

The girder displacement is simply larger than the pier displacement from 5% to 22% where the pier9, the middle pier of the bridge, has the largest difference.

4.1.1.4. Moment-curvature curve of the pier section:

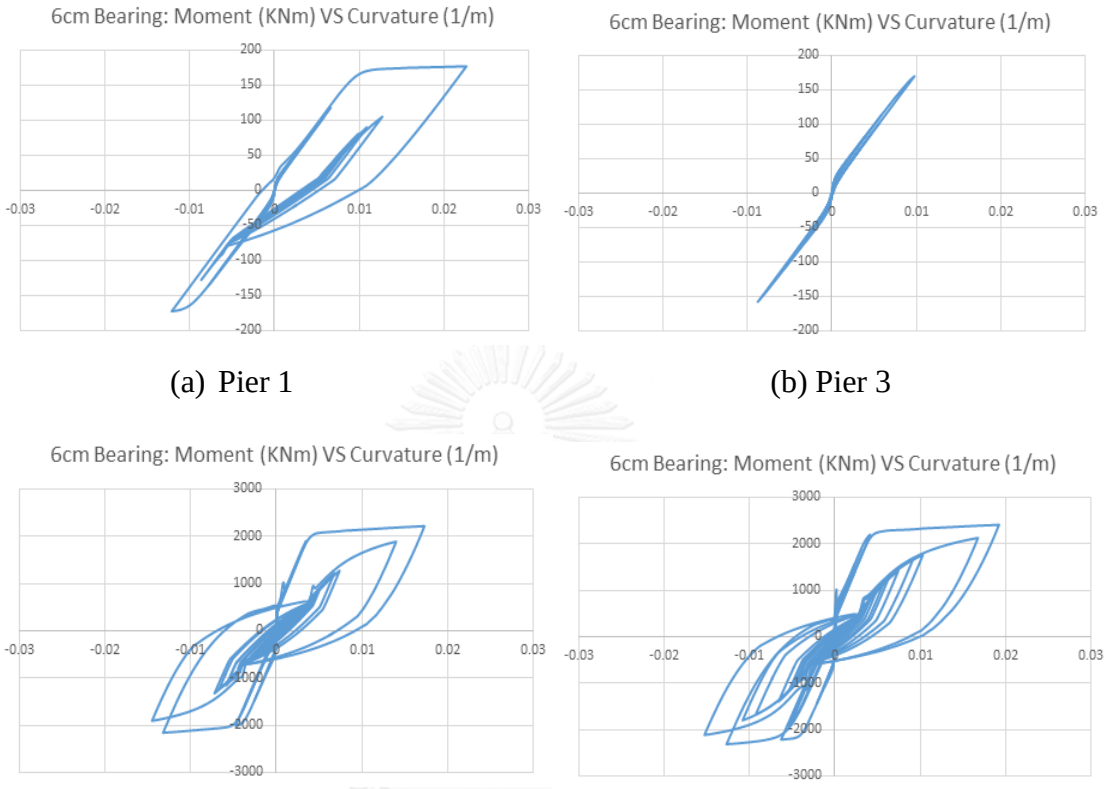

(a) Pier 1 (b) Pier 3

(c) Pier 4 (d) Pier 9

Figure 4.3: Moment-curvature graph of Pier1, Pier3, Pier4, and Pier9 in case of 6cm-thick bearing

The moment-curvature curve also reflects the displacement in the previous section especially the wall-type pier 4 and pier 9 because they have only one fiber section at the bottom of the column while the pile-bent pier 1 and pier 3 also has four different location of fiber element in one column. Even though the maximum displacement is similar, the section in the wall-type pier damages more seriously than that of the pile-bent pier. This is because the wall-type pier is much stiffer and its column section is bigger. Also, it can be observed that only one or two loops that cause the maximum curvature of the column which means the column is not in a serious damage state yet.

The yielding curvature was calculated to be 0.009/m for the column's section of the pile bent and 0.004/m for the column's section of the wall-type pier. The ductility of the section was calculated easily with the formula $Ductility = \frac{\varphi_{ultimate}}{\varphi_{yielding}}$. Therefore, the ductility of the section (not including the pier3 because its section does not yield yet) are: $\mu_{\phi\, pier1} = \frac{0.022}{0.009} = 2.44$, $\mu_{\phi\, pier4} = \frac{0.018}{0.004} = 4.5$, and $\mu_{\phi\, pier9} = \frac{0.019}{0.004} = 4.75$.

4.1.1.5. Stress-strain curve of the pier section:

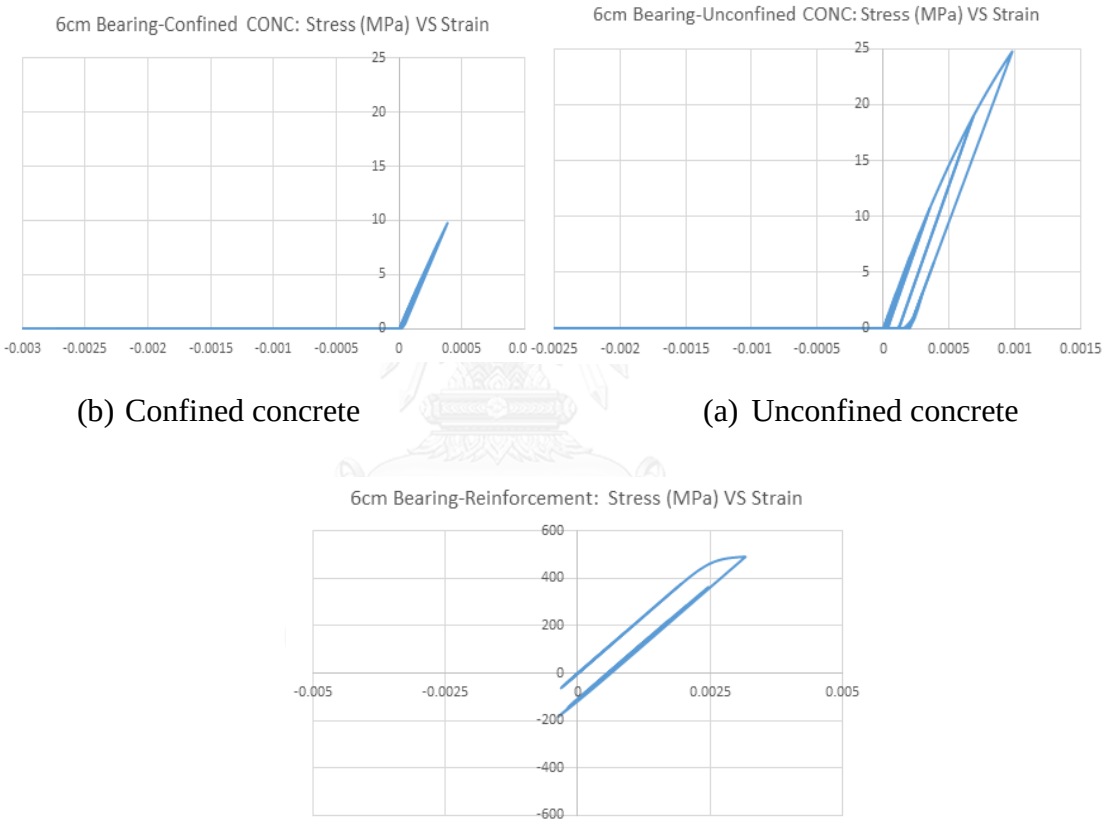

(b) Confined concrete (a) Unconfined concrete

(c) Reinforcement

Figure 4.4: Stress-strain curve of Confined concrete, Unconfined concrete, and Reinforcement in Pier 1

In pier1, the unconfined concrete got slightly yielding where the confined concrete is still in elastic range. Also, the reinforcement also yielded very little. The big loop of the moment-curvature is due to the damage of unconfined concrete.

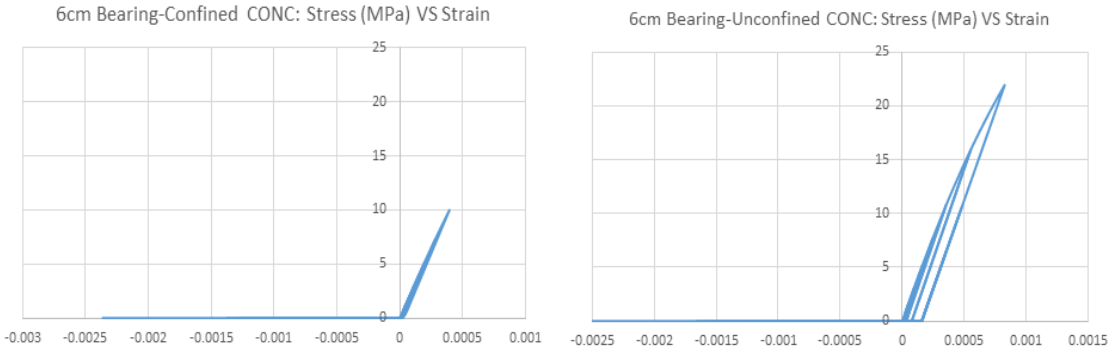

(a) Confined concrete (b) Unconfined concrete

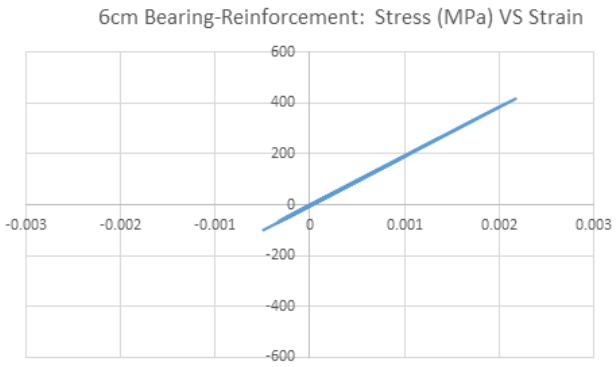

(c) Reinforcement

Figure 4.5: Stress-strain curve of Confined concrete, Unconfined concrete, and Reinforcement in Pier 3

All three materials of the section help prove the linearity of the section. Only the unconfined concrete yielded slight while it does not reach its yielding strength yet while the confined concrete and the reinforcement is still elastic. This matches with the linear graph of moment curvature of the pier.

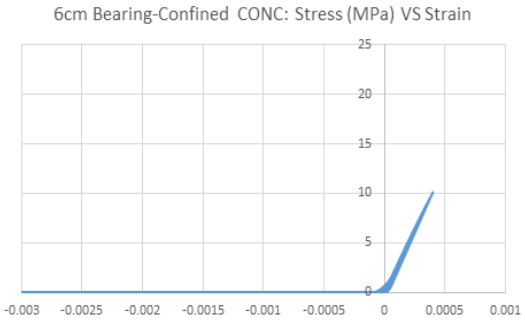

(a) Confined concrete

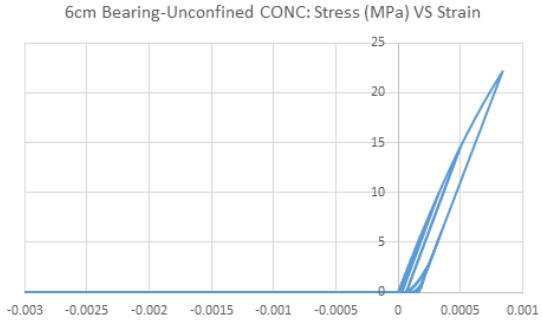

(b) Unconfined concrete

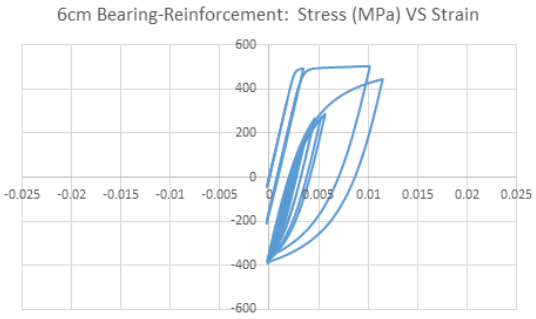

(c) Reinforcement

Figure 4.6: Stress-strain curve of Confined concrete, Unconfined concrete, and Reinforcement in Pier 4

The confined and unconfined concrete of this pier is similar to the previous two. However, the reinforcement of this pier yielded which means the column suffer stronger tension than other piers and this leads to the bigger loop of moment-curvature.

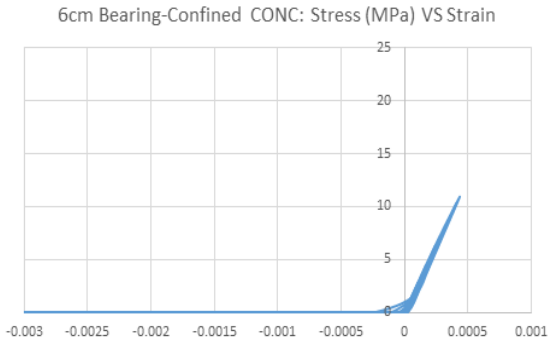

(a) Confined concrete

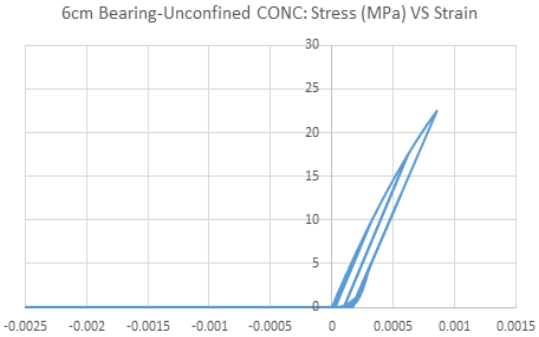

(b) Unconfined concrete

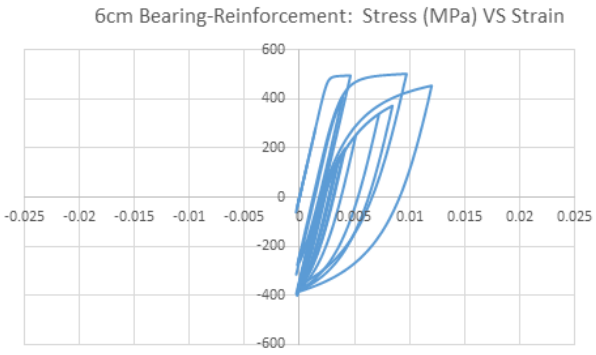

(c) Reinforcement

Figure 4.7: Stress-strain curve of Confined concrete, Unconfined concrete, and Reinforcement in Pier 9

The pier 9 has the same material performances as the pier 4. The confined concrete is elastic while the unconfined concrete slightly yielded. The reinforcement yielded in same level as the previous one.

4.1.1.6. Maximum displacement of all piers of the bridge:

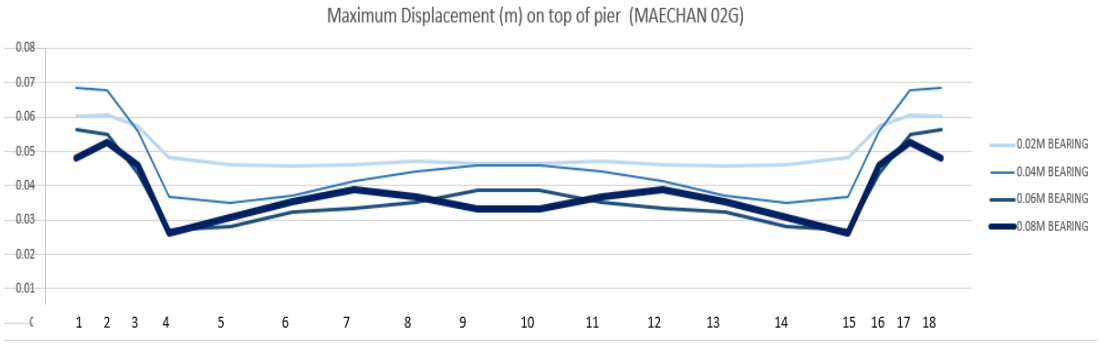

(a) Maximum displacement on top of pier in MAECHAN 0.2G

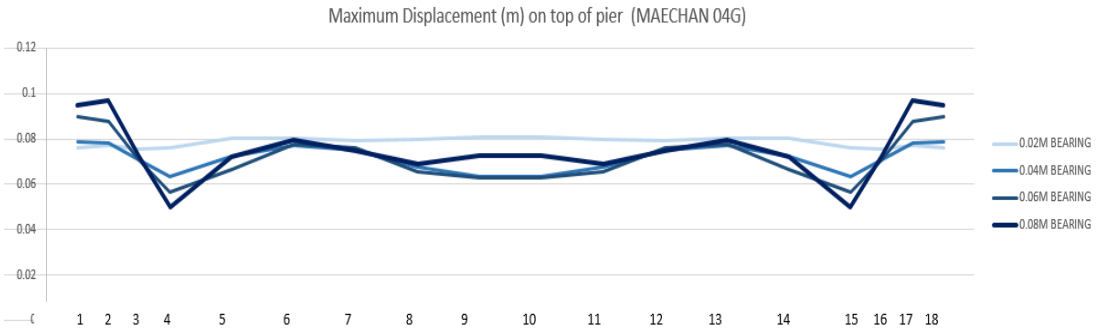

(b) Maximum displacement on top of pier in MAECHAN 0.4G

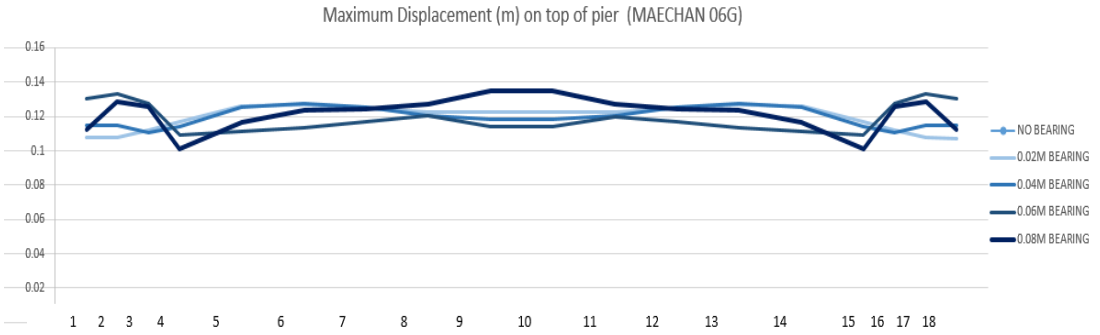

(c) Maximum displacement on top of pier in MAECHAN 0.6G

Figure 4.8: Maximum displacement on top of pier according to the pier number in MAECHAN ground motion

The graph above shows the maximum displacement on top of each pier. The number in the horizontal axis is the number of pier along the bridge. The vertical axis declares the amount of displacement each pier gave after application of ground motion.

For 0.2g PGA, the maximum displacement ranges from 0.07m the biggest to 0.025m the smallest. The biggest maximum displacement occurs at the end of the bridge because there is not abutment soil spring stiffness to handle the force, which makes it more flexible than other piers, while other piers will have piers at both side to help share the stiffness. Meanwhile, the smallest maximum displacement is at the first wall-type pier connected to the pile-bent pier. This is due to the smaller mass from slab girder of pile bent with bigger stiffness of the wall. Overall, the bridge performs better in term of displacement with the thicker bearing and the 0.08m thick bearing made the least displacement for the pier among the four cases. This maximum displacement also reflects with the maximum curvature of fiber section at the bottom of the pier column. They both are proportionally relative. Also, the displacement jump between pile bent and wall-type pier is due to the enormous difference of stiffness of both structures. Since the wall-type pier is stiffer than the pile-bent pier, it moves less than the pile-bent pier. In the 0.4G of MAECHAN ground motion, the similar trend of displacement curve was obtained in the part of wall-type pier and pile bent. In the figure, still the piers at both end give the largest displacement about 0.1m and the smallest is also still at the wall-type pier with 0.05m displacement. As shown, at the pile-bent part, the bearing thickness of 0.02m is enough because it gave the smallest displacement but the wall gives the best performance with 0.06m or 0.08m of bearing thickness. The scaled 0.6g of MAECHAN ground motion might be too strong for the structure. Apparently, the displacement jump is not as much as before. This is due to the stronger scaled earthquake force. The force made the displacement reach its maximum already and the structure will false.

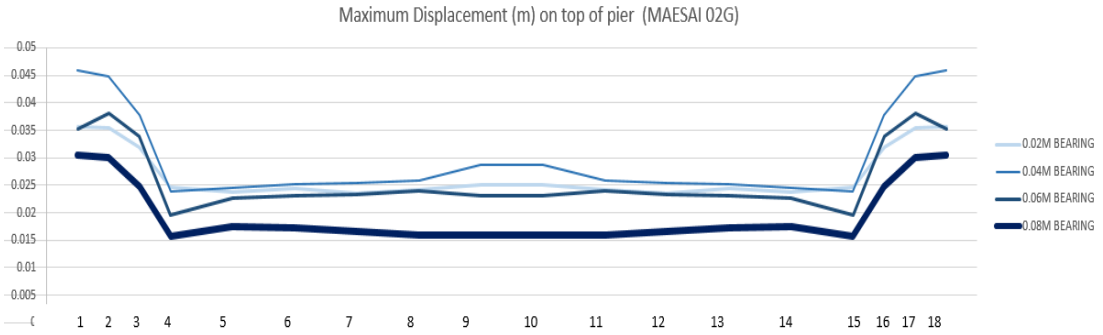

(a) Maximum displacement on top of pier in MAESAI 0.2G

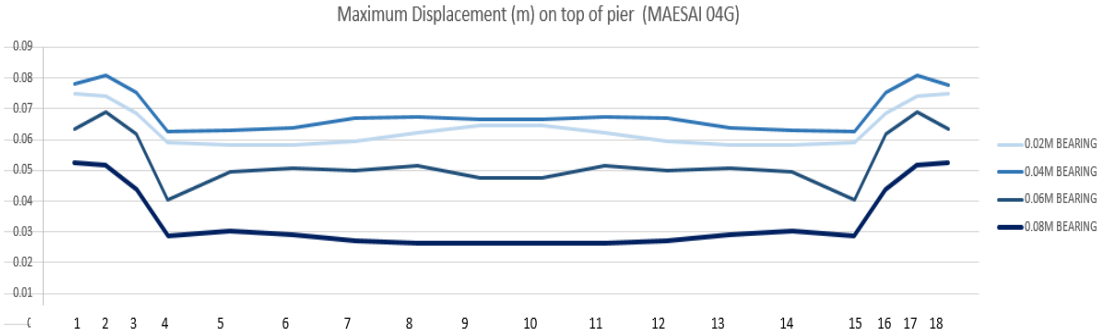

(b) Maximum displacement on top of pier in MAESAI 0.4G

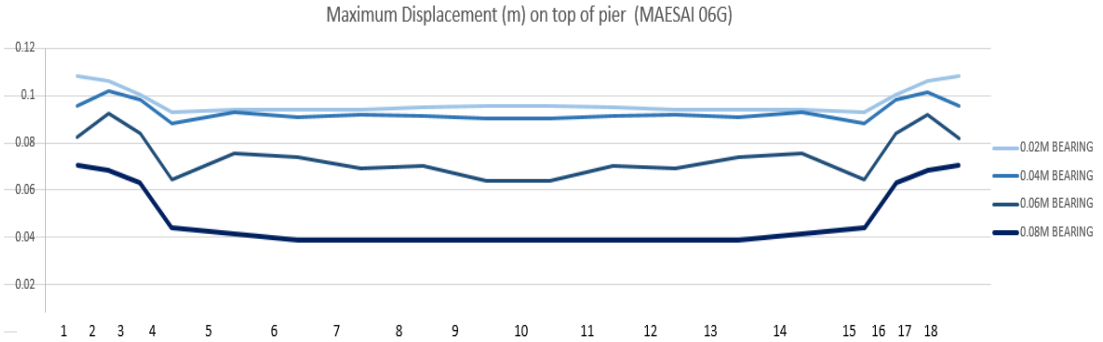

(c) Maximum displacement on top of pier in MAESAI 0.6G

Figure 4.9: Maximum displacement on top of pier according to the pier number of MAESAI ground motion

For MAESAI ground motion, no matter how much the ground motion was scaled, the same trends of displacement were obtained.

For 0.2g of PGA, the biggest displacement is at 0.045m at the end of the bridge and the smallest is 0.015 at the fourth and fifteenth piers, which are the first wall piers from the pile bent. For 0.4g of PGA, the biggest displacement is about 0.08m which is approximately twice comparing to 0.2g of PGA and the smallest displacement is at

0.03m, which also agrees well with the previous conclusion. Last but not least, at 0.6g of PGA, the largest displacement is at the end of the bridge as well with 0.11m which is about three times of 0.2g of PGA and the smallest is 0.04m.

The best bearing thickness for this ground motion is 0.08m since it gave the smallest displacement on top of all piers. Since the dynamic force from this ground motion is not as strong as MAECHAN ground motion, the bridge structure did not happen to be heavily damage. Therefore, the trend was kept although the structure already yielded.

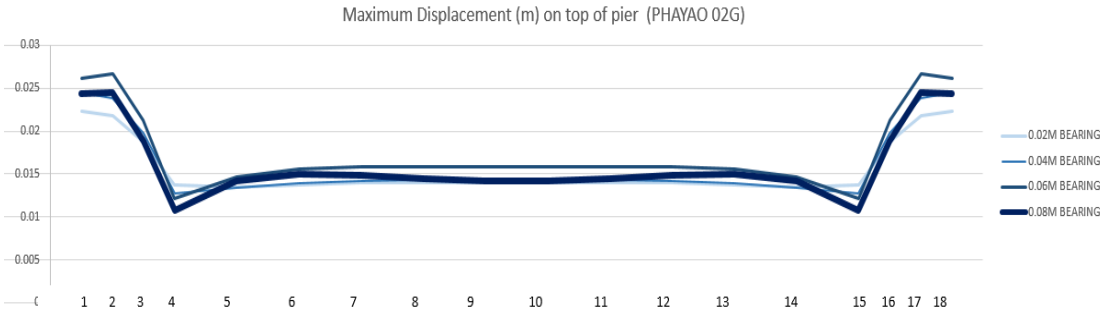

(a) Maximum displacement on top of pier in PHAYAO 0.2G

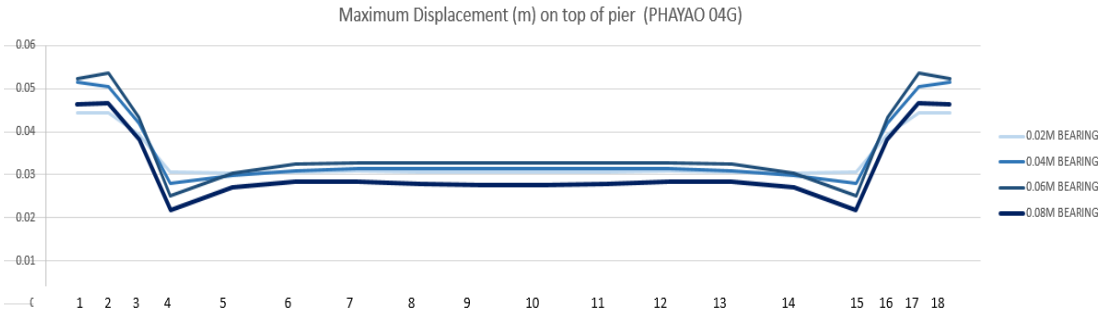

(b) Maximum displacement on top of pier in PHAYAO 0.4G

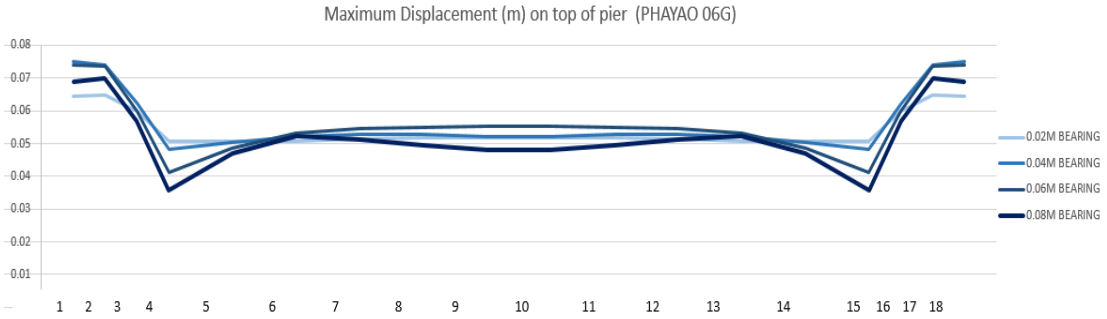

(c) Maximum displacement on top of pier in PHAYAO 0.6G

Figure 4.10: Maximum displacement on top of pier according to the pier number of PHAYAO ground motion

Overall, the responses from all three scaled ground motion of PHAYAO earthquake are in the same trend. The largest maximum displacement was given by the pile bent at the end of the bridge with value of 0.026m, 0.052m, and 0.076m respectively corresponding to 0.2g, 0.4g, and 0.6g of PGA. In contrast, the smallest maximum displacement is at the wall-type pier next to the pile bent, which is about 0.01m, 0.02m, and 0.035m respectively corresponding to 0.2g, 0.4g, and 0.6g of PGA. Since the spectral acceleration curve of the earthquake shows that PHAYAO ground motion has twice smaller accelerations than PGA, the displacement is the smaller.

4.1.1.7. Maximum relative displacement on top of the pier:

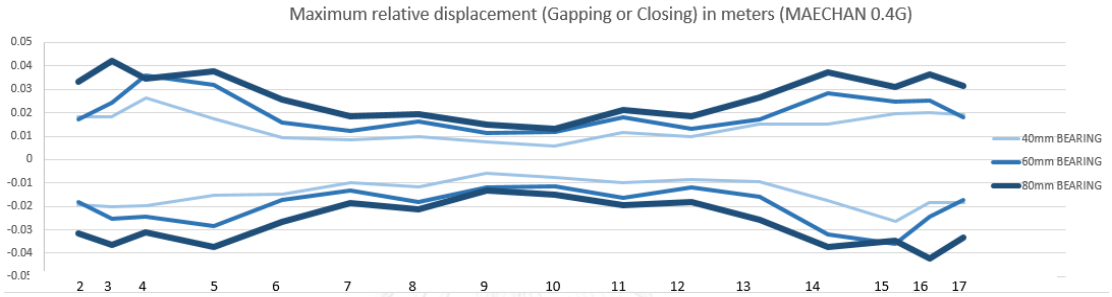

(a) Maximum relative displacement in MAECHAN 0.4G

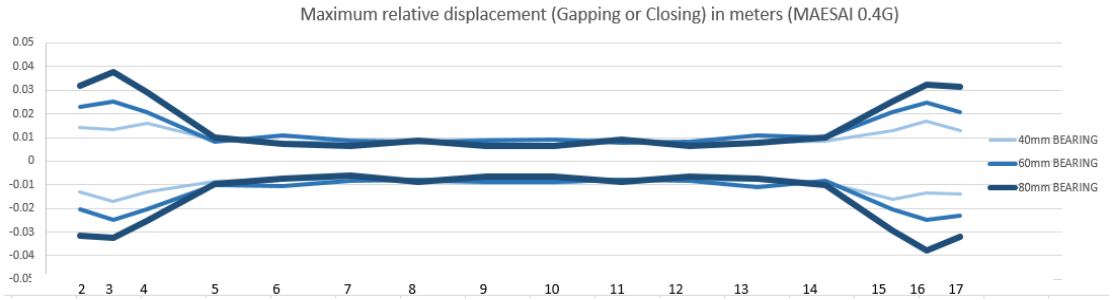

(b) Maximum relative displacement in MAESAI 0.4G

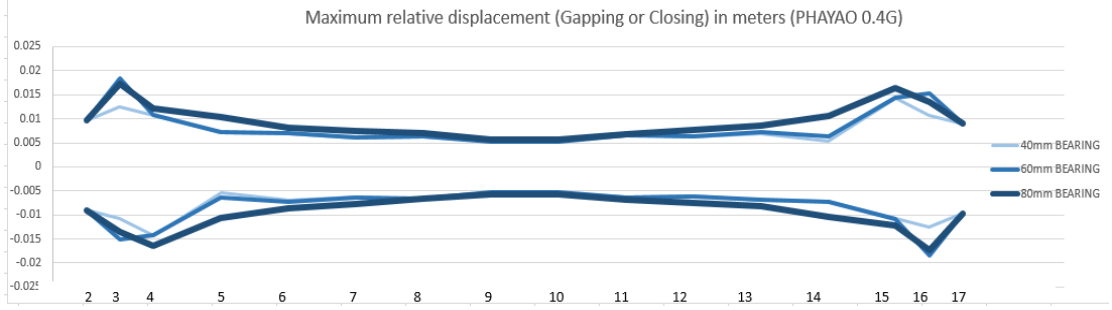

(c) Maximum relative displacement in PHAYAO 0.4G

Figure 4.11: Maximum relative displacement on top of pier in three ground motions

The relative displacement is the result of subtraction of the girder displacement and the pier displacement in time. Then the maximum displacement is shortlisted. The graphs show both the maximum gapping space and the maximum closing space since the pounding effect was ignored. In all three ground motions, the maximum relative displacement is all located at both end of the bridge. The middle piers get the similar gapping or closing space in all three cases of different thickness of bearing which is about 0.02m, 0.01m, and 0.005m respectively in the MAECHAN, MAESAI, and PHAYAO ground motion. At both end of the pier, the relative displacement is up to 100% more than the middle piers. This is because the RC-slab girders of the pile-bent pier are lighter than the box girder piers of the wall that causes the bigger movement of the girders that leads to the larger relative displacement.

4.1.1.8. Maximum bearing displacement on top of pier:

The bearing displacement is calculated by subtraction of the girder displacement and the pier displacement. There are two sides of the bearing location on one pier, the left side and the right side.

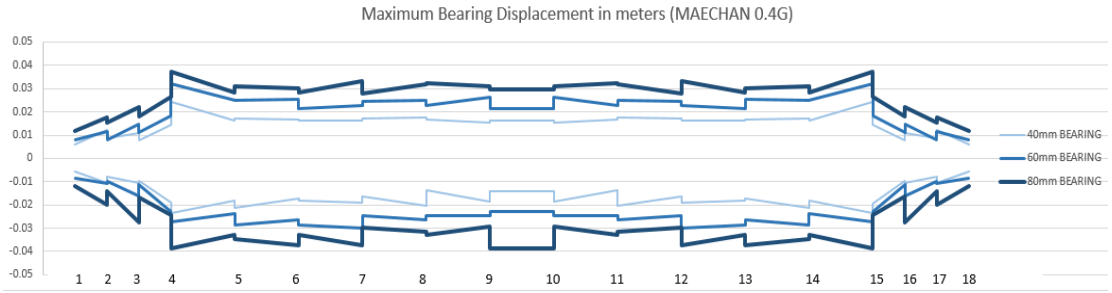

(a) Maximum bearing displacement in MAECHAN 0.4G

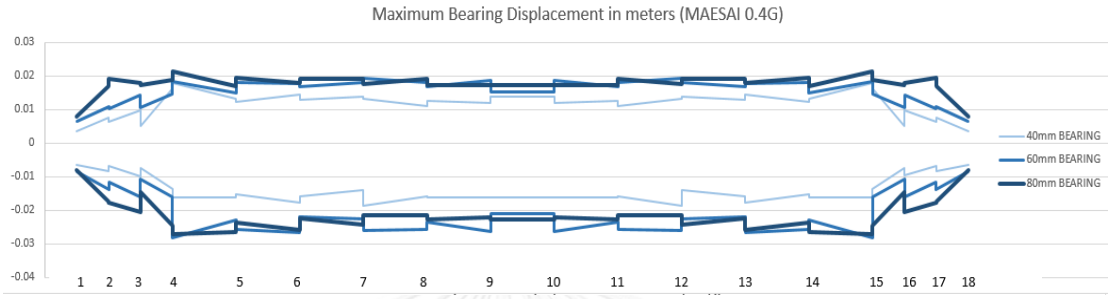

(b) Maximum bearing displacement in MAESAI 0.4G

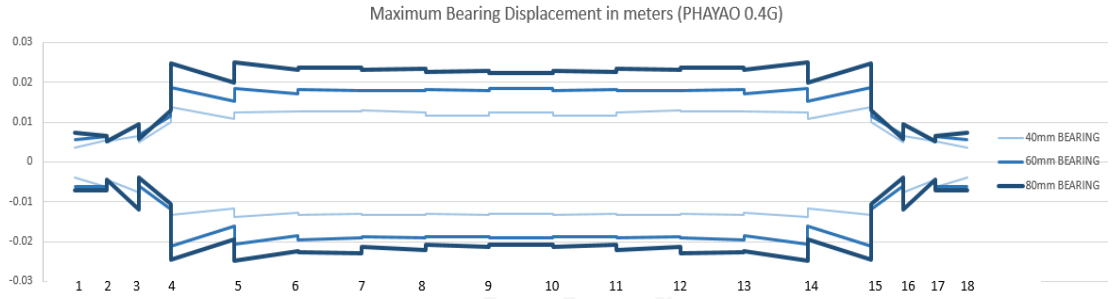

(c) Maximum bearing displacement in PHAYAO 0.4G

Figure 4.12: Maximum bearing displacement on top of pier for three different ground motion

In the graphs above, there are two points on one pier signifying the left hand and right hand displacement of the bearing. The bearing displacement as seen in the figures is more in the middle pier than in the piers at both end. The reasons for the kind of trending is that the wall-type piers displace less than the more flexible pile-bent piers and also that the girders of the wall-type piers move more due to the more mass than the pile-bent piers.

Table 4.3: Maximum shear strain of bearing in 0.4g of MAECHAN with 4cm bearing

Pier Number	Bearing Displacement (m)	Bearing height (m)	Bearing shear strain (%)
1	0.006	0.040	14.60
2	0.012	0.040	30.82
2	0.009	0.040	21.40
3	0.011	0.040	26.89
3	0.010	0.040	24.07
4	0.019	0.040	48.13
4	0.024	0.040	60.49
5	0.018	0.040	45.84
5	0.021	0.040	53.44
6	0.017	0.040	43.13
6	0.018	0.040	45.77
7	0.019	0.040	47.90
7	0.017	0.040	42.55
8	0.020	0.040	50.68
8	0.017	0.040	41.76
9	0.019	0.040	46.90
9	0.016	0.040	40.10
10	0.016	0.040	40.10
10	0.019	0.040	46.91
11	0.017	0.040	41.76
11	0.020	0.040	50.69
12	0.017	0.040	42.55
12	0.019	0.040	47.91
13	0.018	0.040	45.79
13	0.017	0.040	43.14
14	0.021	0.040	53.45
14	0.018	0.040	45.85
15	0.024	0.040	60.49
15	0.019	0.040	48.14
16	0.010	0.040	24.06
16	0.011	0.040	26.83
17	0.009	0.040	21.41
17	0.012	0.040	30.79
18	0.006	0.040	14.58

The table above shows the percentage of the maximum shear strain of the bearing in cases of 4cm bearing in MAECHAN 0.4g of PGA. The percentage is at maximum at pier4 and pier 15 that both of these piers has the percentage of 60%. This can be implied that the bearing does not yet reach its maximum strain yet.

4.1.1.9. Maximum curvature of pier section:

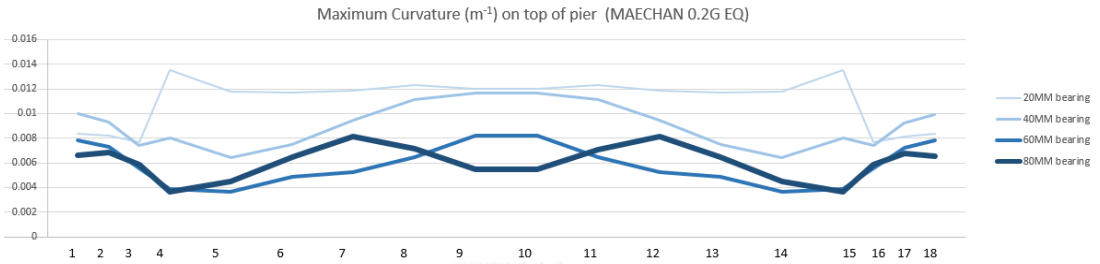

(a) Maximum curvature of pier section in MAECHAN 0.2G

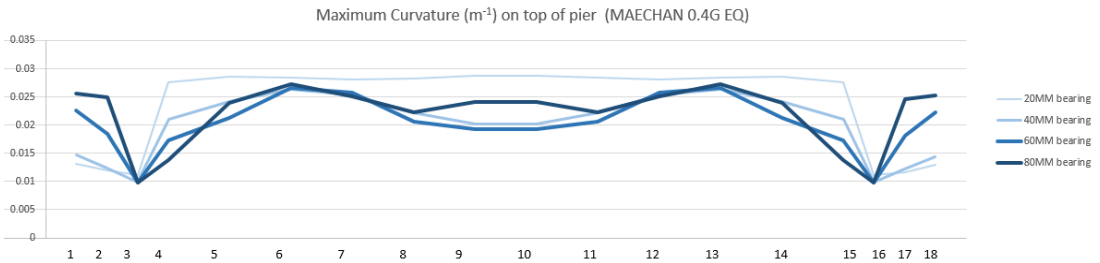

(b) Maximum curvature of pier section in MAECHAN 0.4G

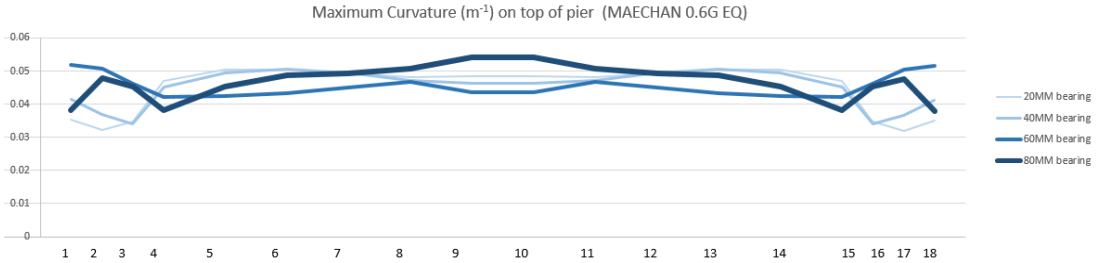

(c) Maximum curvature of pier section in MAECHAN 0.6G

Figure 4.13: Maximum curvature of pier section of each pier in MAECHAN ground motion

For MAECHAN ground motion, the maximum curvature graph for 0.2g of PGA shows clearly that the 8cm-thick bearing gives the smallest curvature while the 2cm-thick bearing case gives the largest curvature. In 0.4g of PGA, three cases except the 2cm-thick bearing gives similar results while the case gives the largest curvature. However, in 0.6g of PGA, all cases gives similar curvatures.

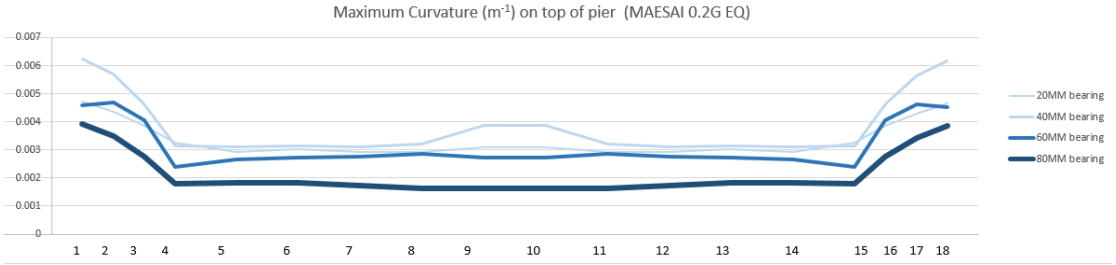

(a) Maximum curvature of pier section in MAESAI 0.2G

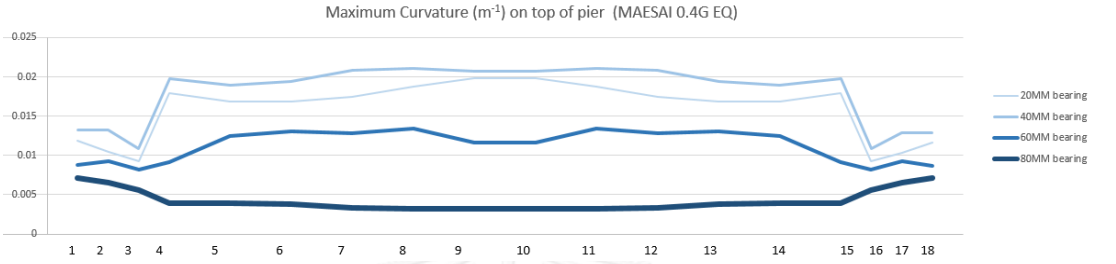

(b) Maximum curvature of pier section in MAESAI 0.4G

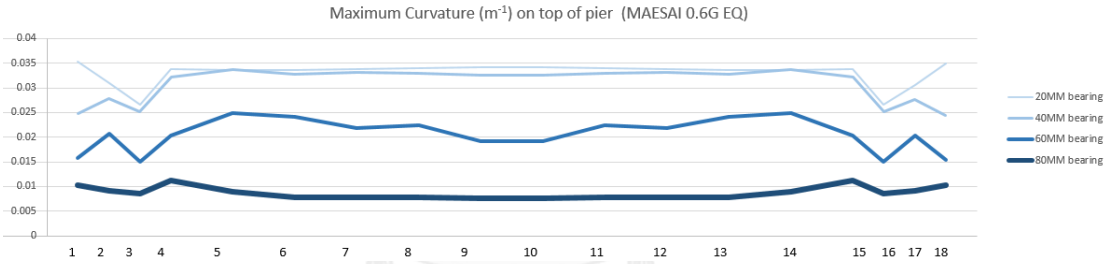

(c) Maximum curvature of pier section in MAESAI 0.6G

Figure 4.14: Maximum curvature of pier section of each pier in MAESAI ground motion

In this ground motion, the results is very clear that the best bearing to applied to the structure is the 8cm-thick bearing where it gives the smallest curvature in all levels of ground motion.

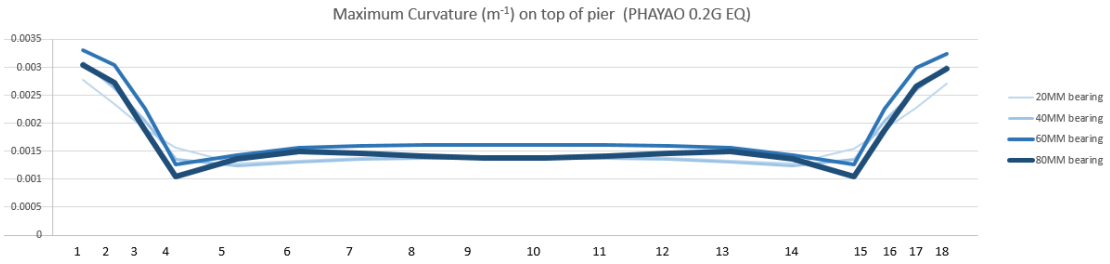

(a) Maximum curvature of pier section in PHAYAO 0.2G

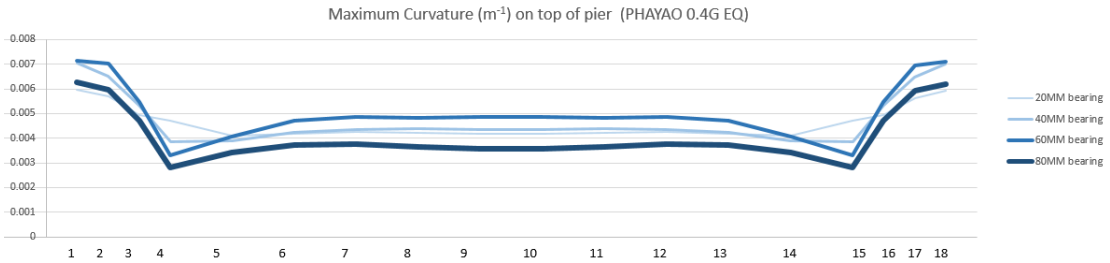

(b) Maximum curvature of pier section in PHAYAO 0.4G

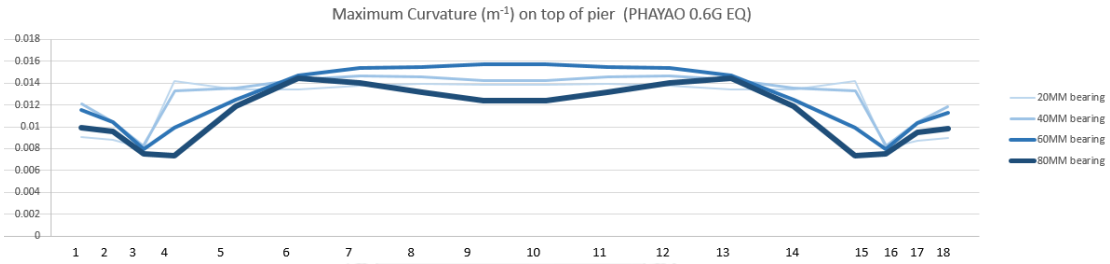

(c) Maximum curvature of pier section in PHAYAO 0.6G

Figure 4.15: Maximum curvature of pier section of each pier in PHAYAO ground motion

In 0.2g and 0.4g of PGA of this ground motion, the trend is quite similar to the 0.2g of previous ground motion. All cases gives similar maximum curvature but the 8cm-thick still gives slightly smaller curvature than others. In 0.6g of PGA, the smallest curvature is still given by the 8cm-thick bearing.

4.1.2. The bridge with abutment soil spring:

4.1.2.1. Time history displacement on top of the pier:

The time-history displacement graph below is the same as the previous but the difference is that in this section, there is the abutment soil spring added to the model as well. Therefore, there is some difference for the time history displacement in some of the pier effected by this abutment soil spring.

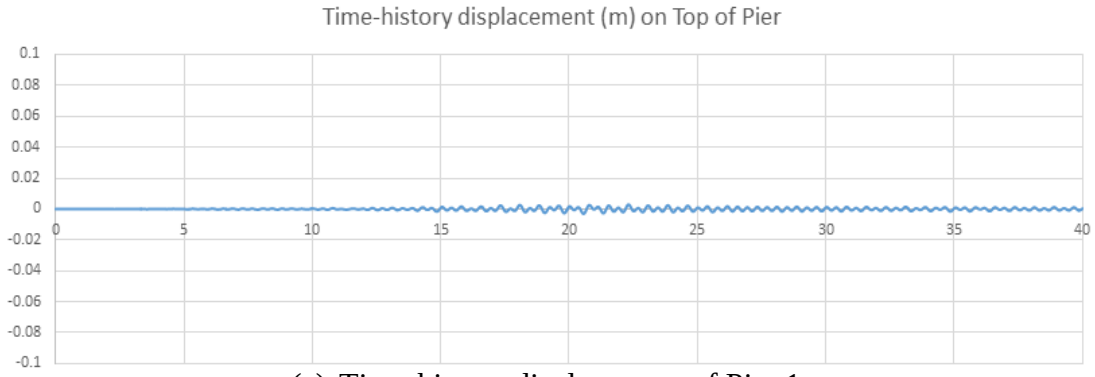

(a) Time-history displacement of Pier 1

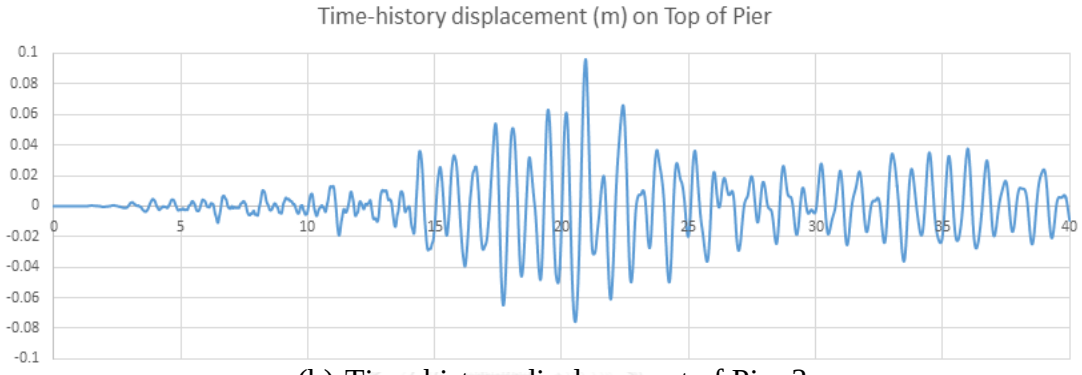

(b) Time-history displacement of Pier 3

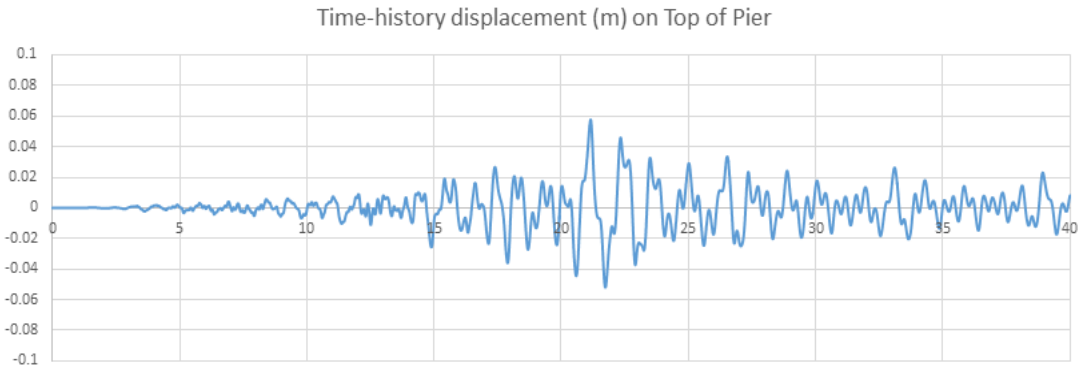

(c) Time-history displacement of Pier 4

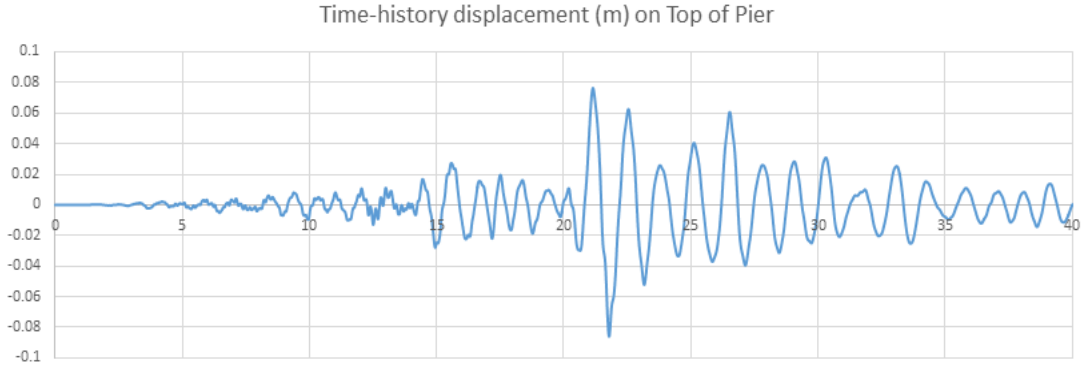

(d) Time-history displacement of Pier 9

Figure 4.16: Time-history displacement (m) on top of Pier1, Pier3, Pier4, and Pier9 in case of 8cm-thick bearing

First of all, after the installation of abutment soil spring stiffness to the model, the time-history displacement of the first pier where the soil spring is put is nearly zero since it is a very stiff soil spring. The pier 3 has a small amplitude since its girders are connected to other girders connecting the soil spring and it is not completely isolated. Then the pier4 has many small returning part when the structure is shaking back slightly. For the pier9, it is out of the effect of the soil spring and it is back to the normal performance which is quite similar to the case without soil spring.

4.1.2.2. Time-history girder displacement:

The time-history girder displacement in this section also shows the differences between the pier and the girder to see how the girder moves away from the pier and the level of differences of girder and piers to indicate the effect of bearing to the structure.

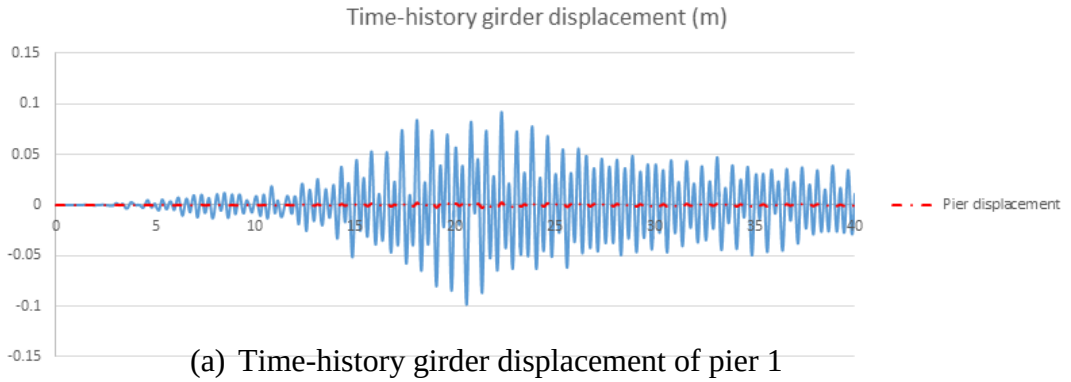

(a) Time-history girder displacement of pier 1

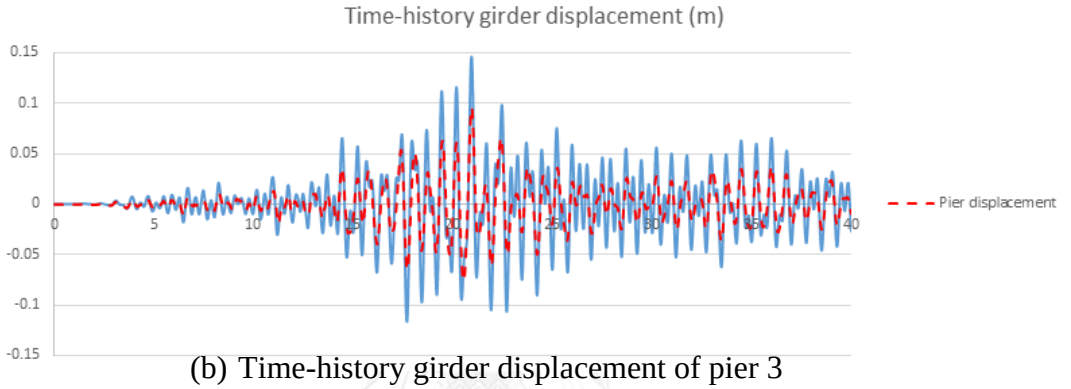

(b) Time-history girder displacement of pier 3

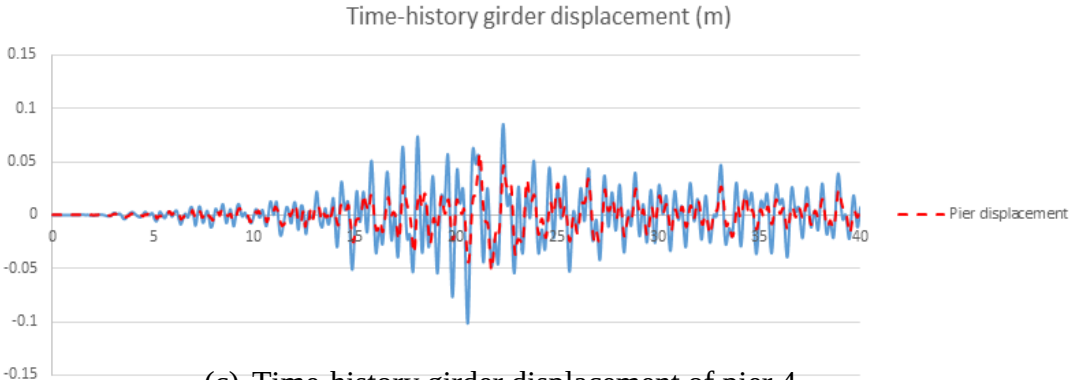

(c) Time-history girder displacement of pier 4

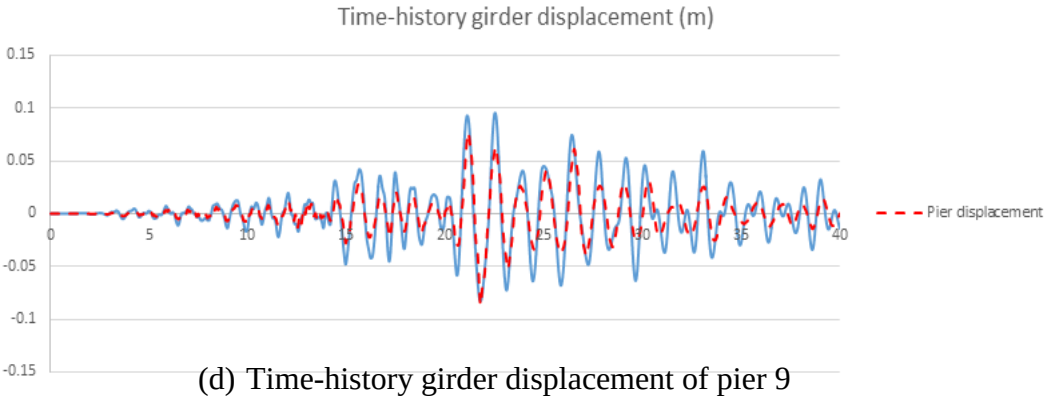

(d) Time-history girder displacement of pier 9

Figure 4.17: Time-history girder displacement (m) of Pier1, Pier3, Pier4, and Pier9 in case of 8cm-thick bearing

The pier1 has a very huge difference between top pier displacement and girder displacement because the stiff soil springs are attached to the top pier and the girders and the pier are isolated by the bearing. For other piers, it can be observed that the soil spring does not have much effect on them especially the pier9. The soil spring may take control some part of the pier stiffness. It make them stiffer and have smaller amplitude in pier3 and pier4.

4.1.2.3. Moment-curvature curve of the pier section:

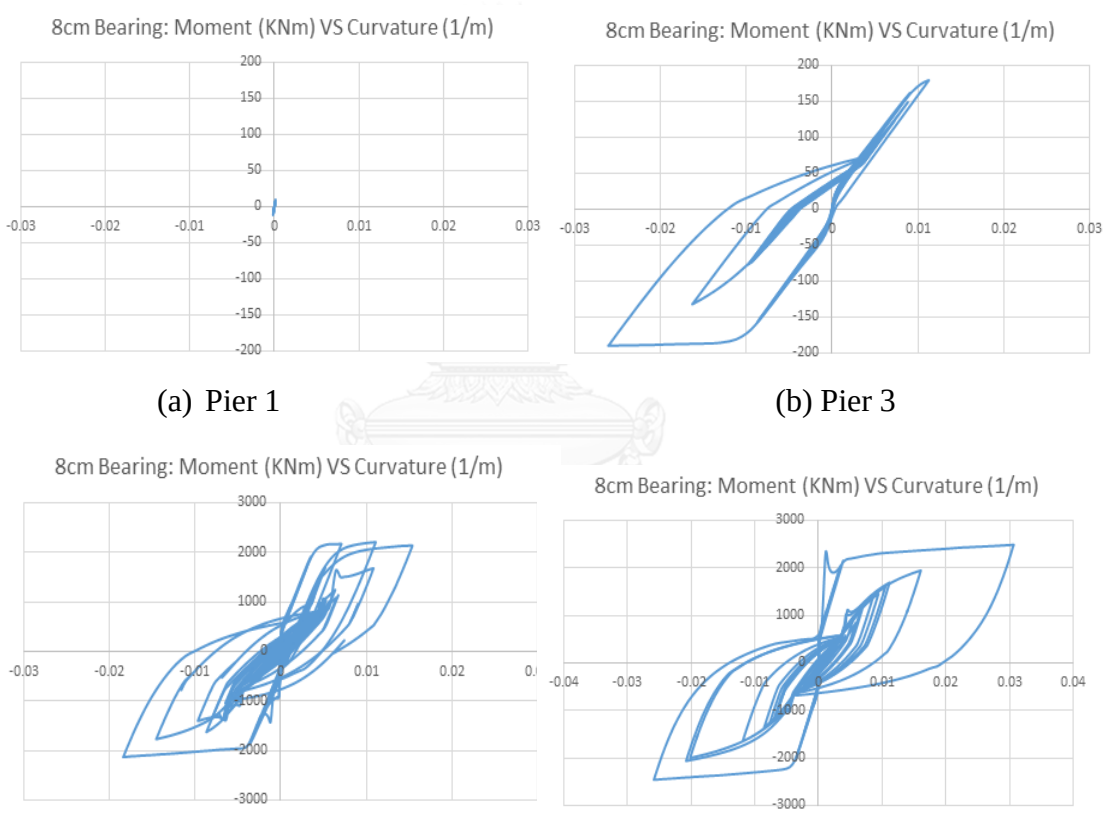

(a) Pier 1 (b) Pier 3

(c) Pier 4 (d) Pier 9

Figure 4.18: Stress-strain curve of the Confined concrete, the unconfined concrete, and the Reinforcement in Pier 9

As predicted, the first pier has a very small linear line of moment-curvature curve which corresponds well to the time-history displacement. The pier4 and pier9 have the similar loop comparing to the case without soil spring stiffness while the pier 3 has some small different when there are a few cycle of larger loop occurs.

The yielding curvature was calculated to be 0.009/m for the column's section of the pile bent and 0.004/m for the column's section of the wall-type pier. Therefore, the ductility of the section (not including the pier1 because its section does not yield yet) are: $\mu_{\phi\,pier1} = \frac{0.026}{0.009} = 2.89$, $\mu_{\phi\,pier4} = \frac{0.018}{0.004} = 4.5$, and $\mu_{\phi\,pier9} = \frac{0.0305}{0.004} = 7.625$.

4.1.2.4. Stress-strain curve of the pier section:

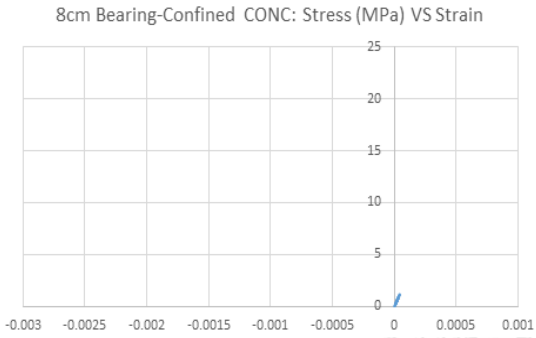

(b) Confined concrete

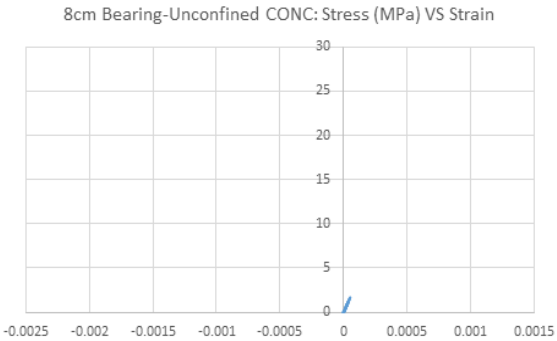

(a) Unconfined concrete

(c) Reinforcement

Figure 4.19: Stress-strain curve of Confined concrete, Unconfined concrete, and Reinforcement in Pier1

The figure above shows clearly the performance of material in the pier1. It is almost no damage at all in the section due to the stiffness of soil spring. Also, another reason to get this result is that the support of the pier was modeled as fix support.

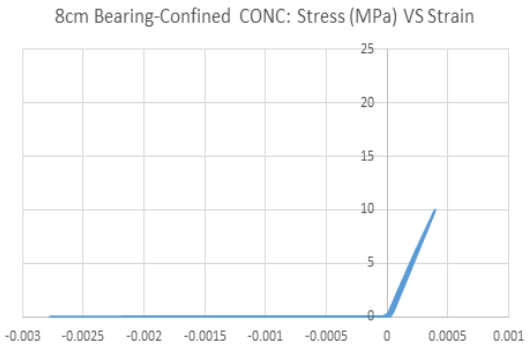

(a) Confined concrete

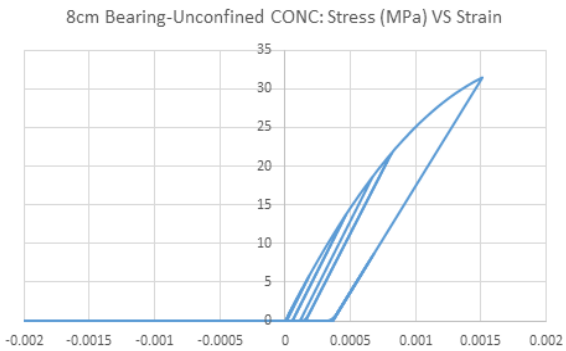

(b) Unconfined concrete

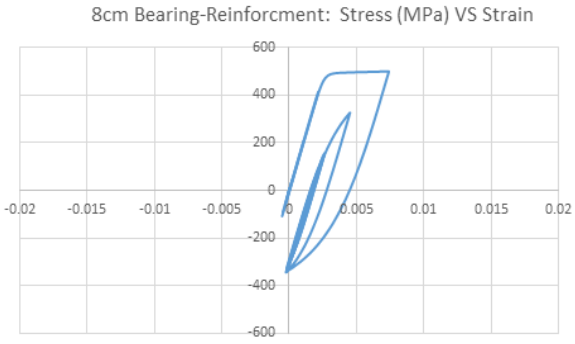

(c) Reinforcement

Figure 4.20: Stress-strain curve of Confined concrete, Unconfined concrete, and Reinforcement in Pier 3

The confined concrete is not seriously damaged while the unconfined yielded already since it reached its yielding strength. With the observation, the reinforcement also yielded but not much.

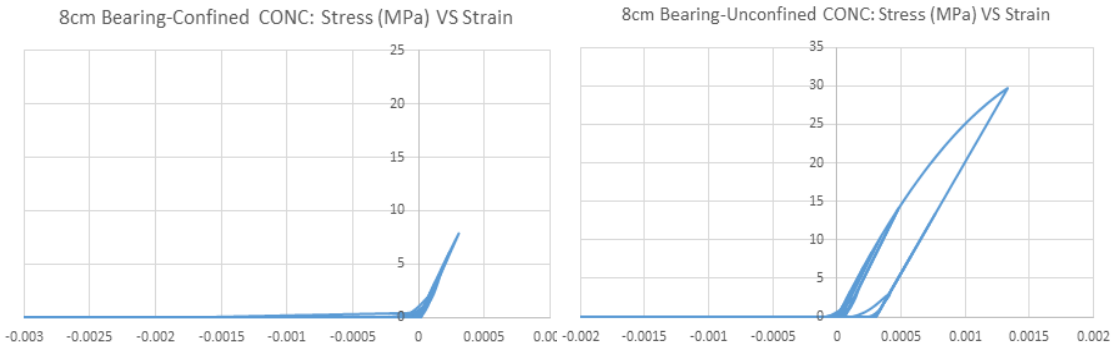

(a) Confined concrete (b) Unconfined concrete

(c) Reinforcement

Figure 4.21: Stress-strain curve of Confined concrete, Unconfined concrete, and Reinforcement in Pier 4

This pier has the similar stress-strain curve with the pier3. The confined concrete is still elastic while the unconfined concrete and the reinforcement yielded already. However, the yielding of both the unconfined concrete and the reinforcement is not considered as serious cases yet.

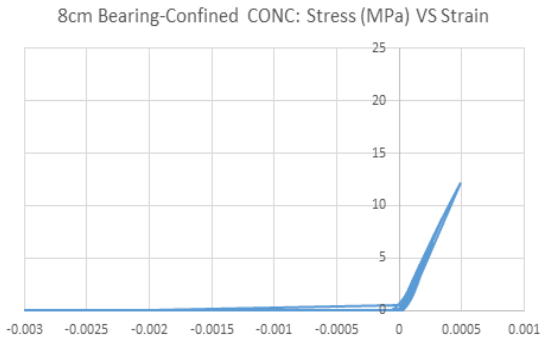

(a) Confined concrete

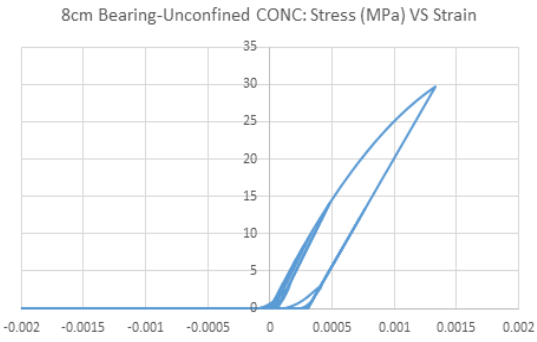

(b) Unconfined concrete

(c) Reinforcement

Figure 4.22: Stress-strain curve of Confined concrete, Unconfined concrete, and Reinforcement in Pier 9

All the three materials have the larger loop of stress-strain curve than the pier4 although they are in the same geometry. This will be explained in the section of maximum displacement section.

4.1.2.5. Maximum displacement on top of the pier:

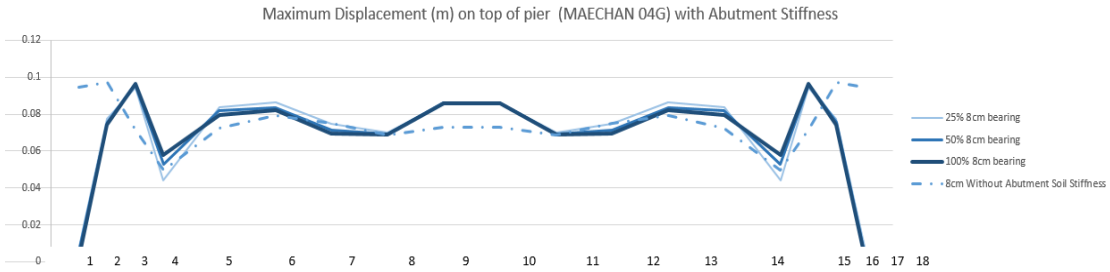

(a) Maximum displacement on top of pier in MAECHAN 0.4G

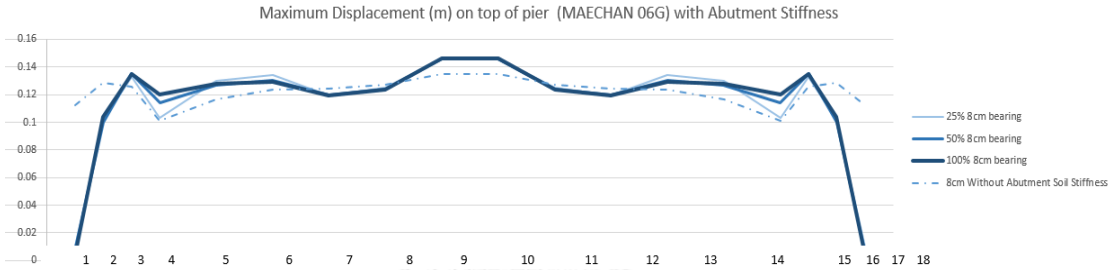

(b) Maximum displacement on top of pier in MAECHAN 0.6G

Figure 4.23: Maximum displacement on top of pier in 0.4g and 0.6g PGA of MAECHAN ground motion

The figures above show the maximum displacements on top of the pier with 8cm-thick bearing in the MAECHAN ground motion with PGA of 0.4g and 0.6g in the case with soil spring stiffness. The figures also the parameters of reduction of soil spring stiffness to 50% and 25% as well. The figure also features the cases of 8cm-thick bearing without abutment soil spring stiffness.

All cases give similar value of displacement except the pier where the stiffness of soil spring was put. It dropped from **0.095m to 0.001m in 0.4g of PGA and 0.11m to 0.003m in 0.6g of PGA.** This is because the stiffness was connected to the pier so that the pier got very stiff – almost not be able to move. However, since there are bearings in the cases performing as the isolators so all piers were separated from each other, the performance on other piers does not have much difference. Also, the reduction of the stiffness does not have any effect to the performance of the bridge in term of displacement while all the three cases give almost the same maximum displacement. This is because the stiffness is too stiff comparing to the pier stiffness.

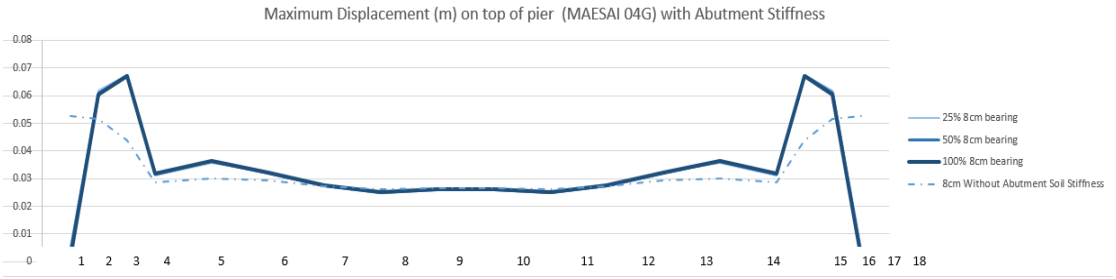

(a) Maximum displacement on top of pier in MAESAI 0.4G

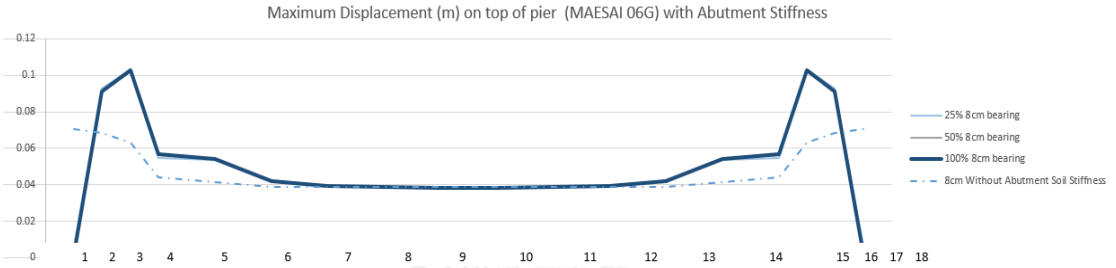

(b) Maximum displacement on top of pier in MAESAI 0.6G

Figure 4.24: Maximum displacement on top of pier in 0.4g and 0.6g PGA of MAESAI ground motion

For MAESAI ground motion, all three cases in reduction of stiffness give the same maximum displacement. Comparing to the case without soil spring stiffness, the end pier has a completely difference where the maximum displacement is **0.051m for the case without soil spring and 0.001m for the case with soil spring in 0.4g of PGA and 0.07m to 0.0015m in 0.6g of PGA**. The same displacement was observed in both cases in the middle piers due to the isolation of the bearing.

It can also be observed that the pop-up point in the middle of maximum displacement in MAECHAN ground motion does not happen in the MAESAI ground motion. This explains that the pop-up is due to the ground motion itself.

4.2. The bridge with elastomeric bearing and shear dowel:

The study of the bridge with both elastomeric bearing and shear dowel will be focused only in the case of the bridge without abutment soil spring stiffness since in

this section the main objective is to investigate the shear dowel's effect to the elastomeric and bridge's structural performance.

4.2.1 Time-history displacement on top of the pier:

There are four different cases of the dowel's diameter to do the comparison. They are 10mm, 12mm, 25mm, and 2 bars of 25mm. The time-history displacement between those with dowels and without dowel are compared.

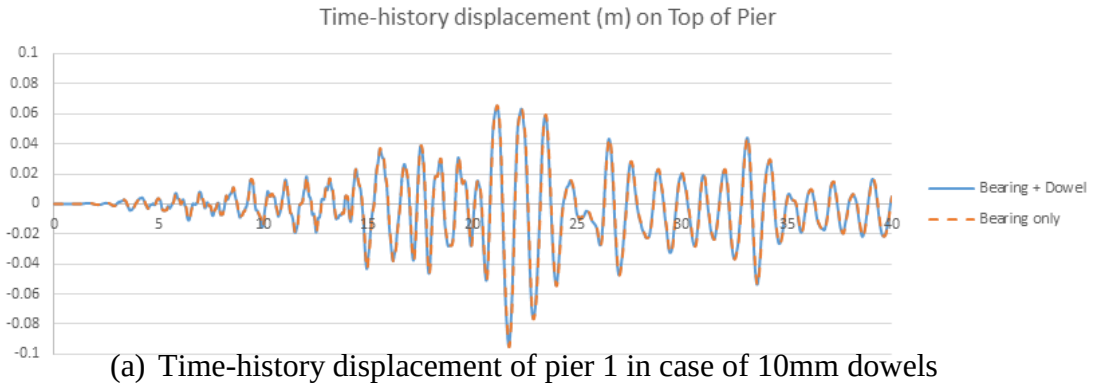

(a) Time-history displacement of pier 1 in case of 10mm dowels

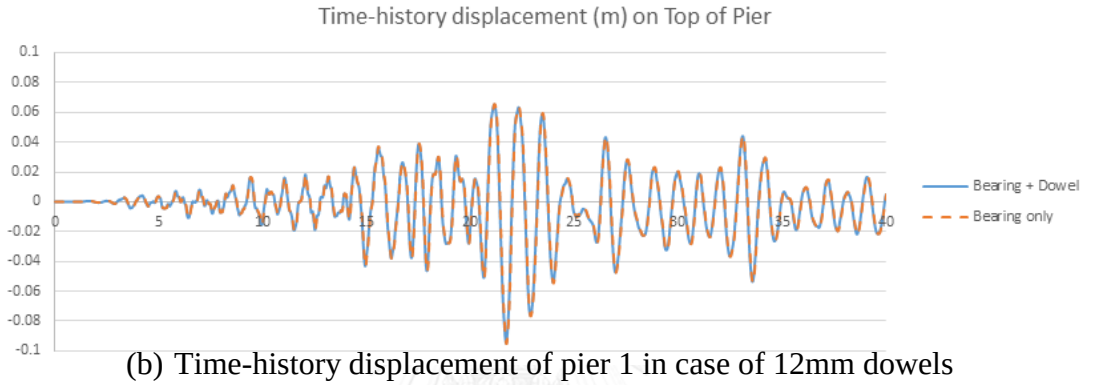

(b) Time-history displacement of pier 1 in case of 12mm dowels

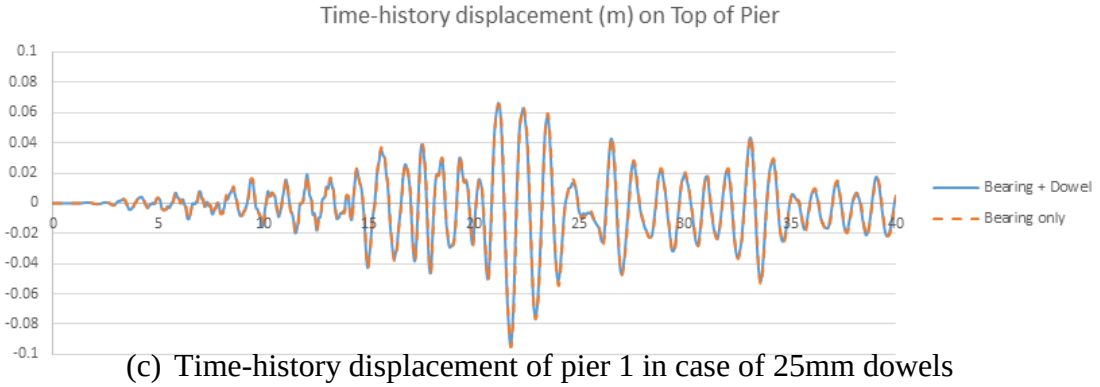

(c) Time-history displacement of pier 1 in case of 25mm dowels

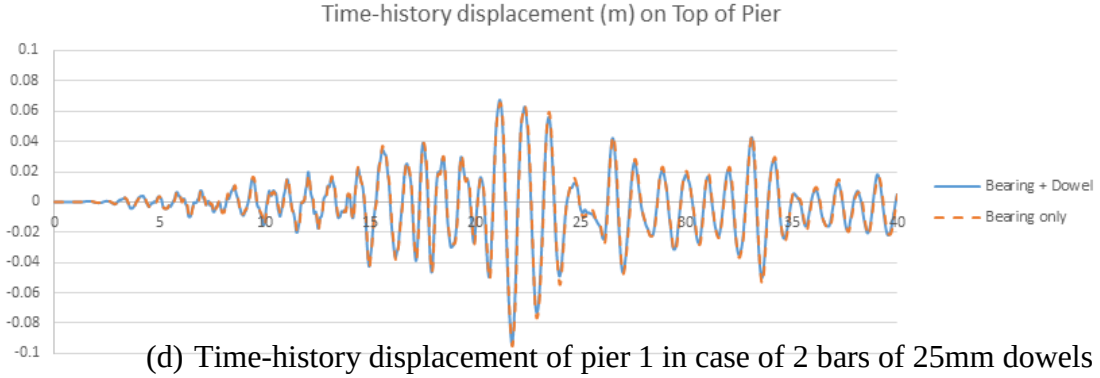

(d) Time-history displacement of pier 1 in case of 2 bars of 25mm dowels

Figure 4.25: Time-history displacement (m) on top of Pier1 in case of 10mm, 12mm, 25mm, and 2 bars of 25mm dowel with 8cm-thick bearing

The figures above show the time-history displacement on top of pier 1. As observed, there is not much difference whether to install the dowels or not. The difference of maximum displacements is shown in table below:

Table 4.4: Maximum displacement on top of pier1, pier3, pier4, and pier9

	Maximum Displacement (mm)			
	Pier 1	Pier 3	Pier 4	Pier 9
Bearing only	94.8	71.9	49.6	72.7
Bearing + 10mm dowel	94.8	71.9	49.7	72.7
Bearing + 12mm dowel	94.8	71.9	49.8	72.7
Bearing + 25mm dowel	94.7	72.0	51.3	72.5
Bearing + 2 bars of 25mm dowel	94.3	72.4	52.5	72.2

There is a very **small** difference between the case with shear dowel and without shear dowel where the reduction of the displacement is about **0.02% to 0.6%** only in the case of 2 bars of 25mm dowel in pier9.

4.2.2. Time-history girder displacements:

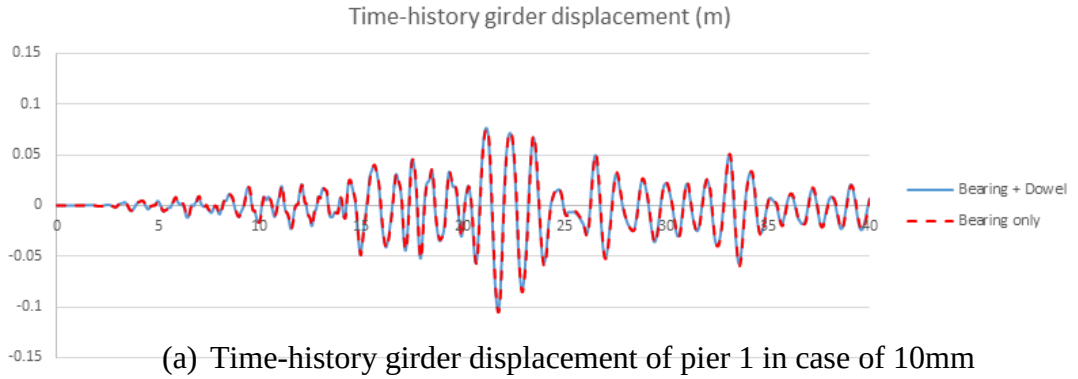

(a) Time-history girder displacement of pier 1 in case of 10mm

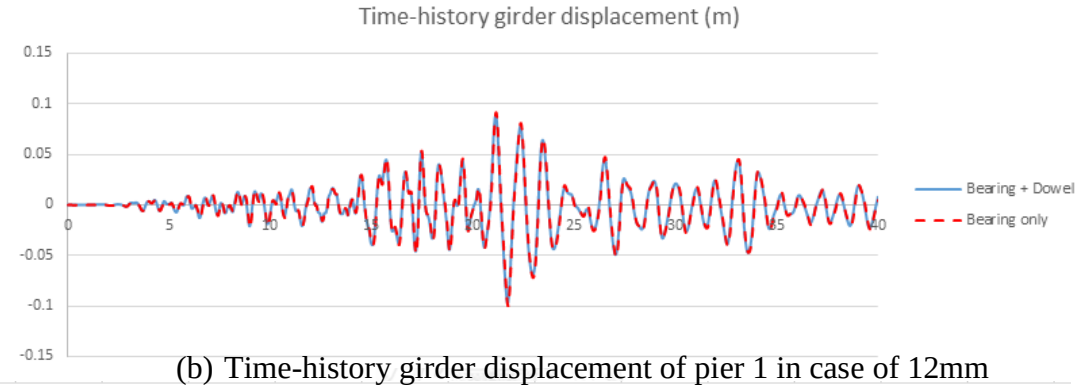

(b) Time-history girder displacement of pier 1 in case of 12mm

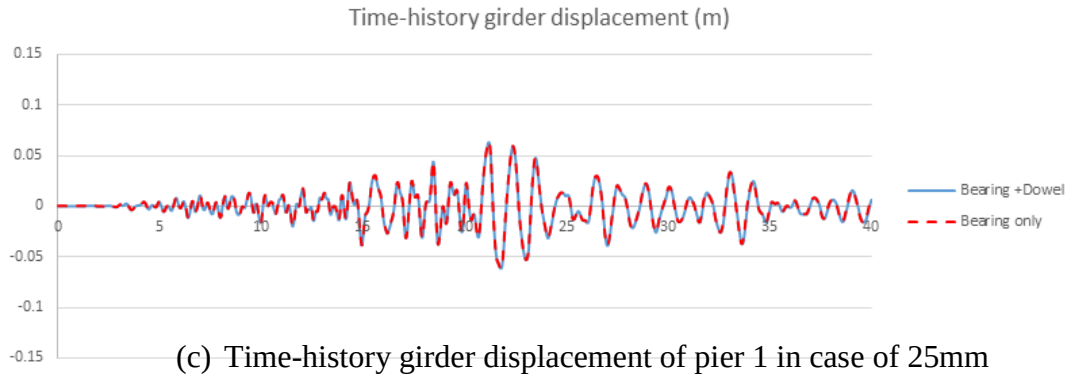

(c) Time-history girder displacement of pier 1 in case of 25mm

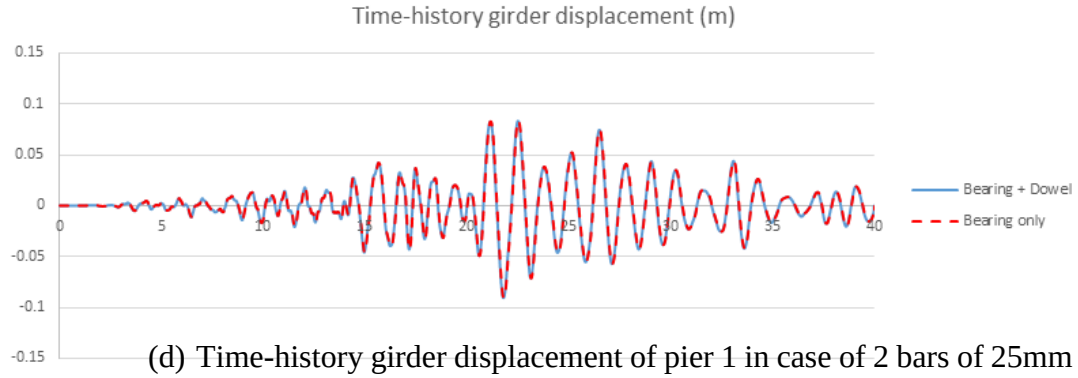

(d) Time-history girder displacement of pier 1 in case of 2 bars of 25mm

Figure 4.26: Time-history girder displacement (m) of Pier1, Pier3, Pier4, and Pier9 in case of 8cm-thick bearing without dowel and with 25mm dowel

The girder displacement also gives the same performance between the case with elastomeric bearing and with elastomeric bearing and shear dowel. The difference is very small. The different displacement of girder will be noted into the table below.

Table 4.5: Maximum girder displacement of pier1, pier3, pier4, and pier9

	Maximum Displacement (mm)			
	Pier 1	Pier 3	Pier 4	Pier 9
Bearing only	105.1	99.4	59.8	90.4
Bearing + 10mm dowel	105.1	99.3	59.9	90.4
Bearing + 12mm dowel	105.1	99.2	60.0	90.4
Bearing + 25mm dowel	104.7	97.3	61.4	90.5
Bearing + 2 bars of 25mm dowel	104.2	95.9	63.1	90.7

The difference of the girder displacement between the case without dowel and with different diameter of steel bar is shown in the table. It has a very small gap of different as observed even though it is more reduced more than the top pier displacement. The range of girder displacement reduction is **0.14% to 3.5% of the displacement without dowel.**

4.2.3. The case of reduction of the shear dowel height:

The previous cases were the one in which the dowel height is equal to the bearing height which means when the bearing height is 8cm, the dowel height is also 8cm. However, after the previous observation, it was not very effective for this kind of study because the dowel is more flexible than the bearing. So, an idea was proposed to install the shear dowel in different location so that the height of the dowel can be shorter and can provide more stiffness for force resistance. In the following study, the dowel

height is chosen to be 0.04m, half of the previous cases where the bearing stays with the same height of 0.08m.

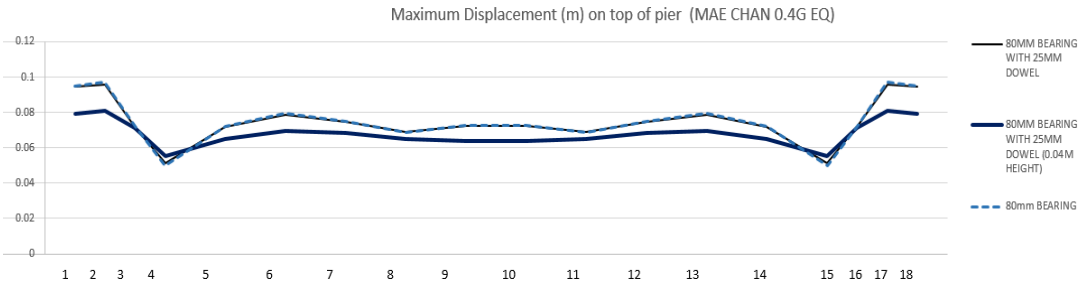

(a) Maximum displacement on top of pier in MAECHAN 0.4G

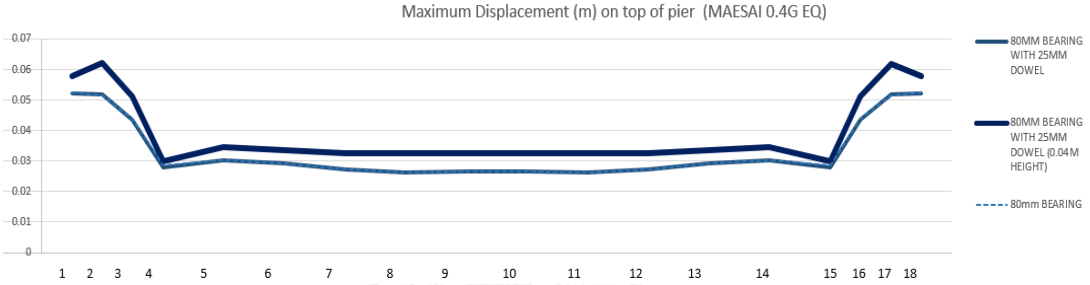

(b) Maximum displacement on top of pier in MAESAI 0.4G

Figure 4.27: Maximum displacement on top of pier in 0.4g of PGA of ground motion

In MAECHAN ground motion, the displacement reduced at both end about 20% of the total displacement while in the middle piers, the displacement reduced about 8% only. However, in MAESAI ground motion, the displacement after the installation of 0.04m height of shear dowel even made the displacement more than the one without shear dowel. From these two graph, a small conclusion was made that the usage of the shear dowel was not always effective in all the ground motion even it made the structure stiffer.

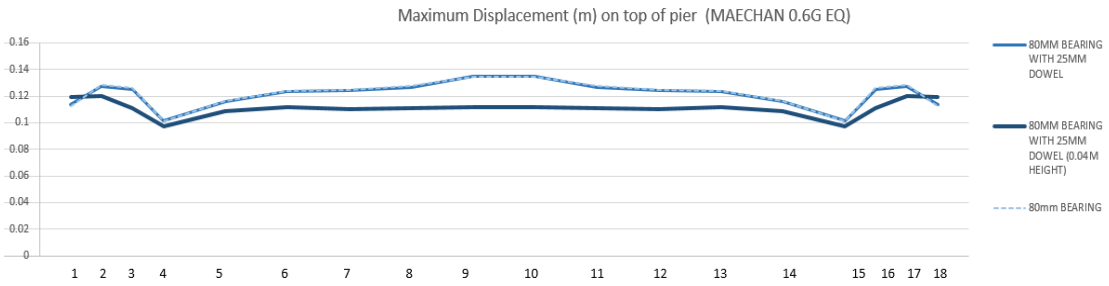

(a) Maximum displacement on top of pier in MAECHAN 0.6G

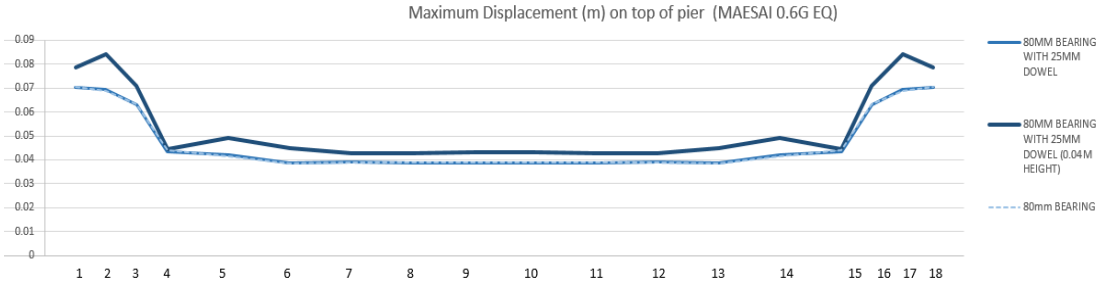

(b) Maximum displacement on top of pier in MAESAI 0.6G

Figure 4.28: Maximum displacement on top of pier in 0.6g of PGA of ground motion

For 0.6g of PGA of the two ground motions, the trend is similar to the case with 0.4g of PGA. The difference is at the amount of displacement. Since the force increases, the displacement increases as well. For MAECHAN ground motion, the installation of shear dowel helped reduce the displacement to about 35% in the middle piers and about 5% to 7% at both end. However, it is different for MAESAI ground motion. In this ground motion, the installation of shear dowel did not meet the objective of reducing the displacement but it is only the slightly increasing of the displacement.

CHAPTER 5 : CONCLUSION AND DISCUSSION

Briefly, the targeted bridge Mae Lao Bridge, is the reinforced concrete bridge containing 18 piers in which there are two types of piers: the pile-bent pier and the wall-type pier. Meanwhile, there are also two types of girders: the 10m-span reinforced concrete slab girder and the 20m-span box girder. The pile-bent pier contains of ten 0.4mx0.4m columns with crossbeam at 4m and the columns are 7m tall. The wall-type piers is 10m tall and has hollow inside. There are 6 pile-bent piers with 3 at each side and other 12 wall-type pier in the middle.

The bridge model was built with fiber element in the critical part and the elastic or rigid element in other parts. To implement to the model of the bridge, the elastomeric bearing and the shear dowel were added. The bearing was modeled as elastic model and the dowel as bilinear model. The parameters of the analysis are the variation of bearing thickness of 2cm, 4cm, 6cm, and 8cm and of dowel diameter of 10mm, 12mm, and 25mm. The different performance of the bridge will be observed in term of time-history displacement on top of pier, time-history girder displacement, moment-curvature loop, and stress-strain curve of the material including the confined concrete, the unconfined concrete and the reinforcement. There are three different ground motions with three different PGA.

The results were analyzed as follow:

1. For the study of **the effect of elastomeric bearing only to the bridge performance when the abutment soil spring stiffness was not installed**, the pier at both end gave bigger displacement than other piers in the middle. In MAECHAN and PHAYAO ground motion, the case of 6cm and 8cm-thick bearing had more effect to the bridge performance than 2cm or 4cm-thick bearing. They could reduce the displacement both on the top of the piers and the girders which could relate as well to the curvature of the column section and the stress-strain curve of the materials. However, the 8cm-thick bearing gave the best performance in term of displacement and

curvature in the MAESAI ground motion. The difference between 6cm-thick and 8cm-thick cases was about 15% to 20%. The maximum relative displacement graph also showed the significant difference of the different thickness of bearing to the bridge pier displacement. The 8cm-thick bearing gave the largest displacement at only both end but the middle piers are way more similar no matter how the thickness varied. The bearing displacement was different from the relative displacement since the bearing displacement was less at both end than the middle pier for it has larger displacement than the wall-type piers.

2. For the study of **the effect of elastomeric bearing only to the bridge performance** when the abutment soil spring stiffness was installed, for both MAECHAN and MAESAI ground motion, the biggest difference happened in the piers where the abutment stiffness was put since it was stiffer than before and made the piers almost not have any displacement. However, this made the piers next by have some change such as the pier 3 and pier 4 where the moment-curvature loop is a bit larger than the case without abutment soil spring. Meanwhile, as the piers approaches the middle of the bridge, the abutment soil spring stiffness did not have any effect on the bridge performance anymore for it was the same between both cases.
3. For the study **of the effect of the shear dowel to the bridge performance without the abutment soil spring stiffness**, the dowel diameters varied between 10mm, 12mm and 25mm. The performance of bridge with elastomeric bearing and shear dowel was compared with that with elastomeric bearing only. As observed, there was a very small difference where the shear dowel helped reduce the girder displacement certainly with maximum of 3.5% in case of 2 bars of 25mm-diameter dowel. The shear dowel could really reduce the displacement however the level of reduction was very limited. Another case was proposed to reduce the dowel height

to 0.04m. The results of displacement was different for two ground motions. This meant that the shear dowels were not always effective in all ground motion.

Overall, the bridge did not have serious damage especially the confined and the unconfined concrete even though the ground motion was very strong. The recommendation of the application of elastomeric bearing is the 8cm thickness because this thickness of bearing helps the bridge perform better than other thickness parameters in all three ground motion with different level of PGA as well. On the other hand, the abutment soil spring does have effect on the performance of the bridge completely especially the pier at both end. It will make the pier stiffer to reduce the displacement but the force will go to other piers nearby instead. The recommendation for the shear dowel is to install 25mm diameter of steel bar with 0.04m height since it is the best way to reduce the displacement of both the piers and girders the most which is the purpose to place it in the structure.

In short, the bridge will perform better in term of displacement, and section curvature while it faces the serious earthquake after the elastomeric bearing and the shear dowel recommended above are installed.

REFERENCES

ACI, (2005). 301-Specifications for Structural Concrete for Buildings. *American Concrete Institute International, 32*, 1313-1312.

Akogul, C., & Celik, O. C. (2008). *Effect of elastomeric bearing modeling parameters on the Seismis design of RC highway bridges with precast concrete girders.* Paper presented at the Proceedings of the 14th World Conference on Earthquake Engineering.

Anil, Ö., & Altin, S. (2007). An experimental study on reinforced concrete partially infilled frames. *Engineering structures, 29*(3), 449-460.

Bozorgzadeh, A., Ashford, S. A., Restrepo, J. I., & Nimityongskul, N. (2008). Experimental and Analytical Investigation on Stiffness and Ultimate Capacity of Bridge Abutments. *SSRP, 7*, 12.

Caltrans, S. (2004). Seismic design criteria: Version.

Deng, K., Pan, P., Su, Y., Ran, T., & Xue, Y. (2014). Development of an energy dissipation restrainer for bridges using a steel shear panel. *Journal of Constructional Steel Research, 101*, 83-95.

Dimitriadou, O. (2007). *Effect of isolation on bridge seismic design and response.* (Master degree), Pavia, Italy.

Ghosh, G., Singh, Y., & Thakkar, S. K. (2011). Seismic response of a continuous bridge with bearing protection devices. *Engineering structures, 33*(4), 1149-1156.

Gomes, A., & Appleton, J. (1997). Nonlinear cyclic stress-strain relationship of reinforcing bars including buckling. *Engineering structures, 19*(10), 822-826.

Hoshikuma, J., Kawashima, K., Nagaya, K., & Taylor, A. (1997). Stress-strain model for confined reinforced concrete in bridge piers. *Journal of Structural Engineering, 123*(5), 624-633.

Jónsson, M. H., Bessason, B., & Haflidason, E. (2010). Earthquake response of a base-isolated bridge subjected to strong near-fault ground motion. *Soil dynamics and earthquake engineering, 30*(6), 447-455.

Kent, D. C., & Park, R. (1971). Flexural members with confined concrete. *Journal of the Structural Division, 97*(7), 1969-1990.

Mander, J. B., Priestley, M. J., & Park, R. (1988). Theoretical stress-strain model for confined concrete. *Journal of Structural Engineering, 114*(8), 1804-1826.

Maroney, B. H. (1995). *Large scale bridge abutment tests to determine stiffness and ultimate strength under seismic loading*.

Menegotto, M., & Pinto, P. (1973). *Method of Analysis for Cyclically Loaded RC Frames Including Changes in Geometry and Non-elastic Behaviour of Elements Under*

Combined Normal Force and Bending. Paper presented at the IABSE Congress Reports of the Working Commission.

Priestley. (1996). *Seismic design and retrofit of bridges*: John Wiley & Sons.

Priestley, M. N., Seible, F., & Calvi, G. M. (1996). *Seismic design and retrofit of bridges*: John Wiley & Sons.

S. Soralump, J. F., Sirisart yangsanphu, Montri Jinagoolwipat, Chinoros Thongthamchart, Rattatam Isaroranit. (2014). *Impacts of 2014 Chiangrai Earthquake from Geotechinical Perspectives*. Paper presented at the EIT-JSCE Joint International Symposium on Human Resource Deveopment for Disaster-Resilient Countries 2014.

Silvia Mazzoni, F. M., Michael H. Scott, Gregory L. Fenves, et al. (2007). OpenSees Command Language Manual.

Siqueira, G. H., Sanda, A. S., Paultre, P., & Padgett, J. E. (2014). Fragility curves for isolated bridges in eastern Canada using experimental results. *Engineering structures, 74*, 311-324.

Vorakorn, S. (2008). *Performance.* (Doctoral Degree), Chulalongkorn University, Bangkok, Thailand.

Zhang, C., Zhang, Z., & Zhang, Q. (2012). Static and dynamic cyclic performance of a low-yield-strength steel shear panel damper. *Journal of Constructional Steel Research, 79*, 195-203.

APPENDIX

APPENDIX	Cases study	Graph type	Ground motion	PGA
APPENDIX 1	Case without abutment and without shear dowels	APPENDIX 1.1: Maximum relative displacement	MAECHAN	0.2G
				0.6G
			MAESAI	0.2G
				0.6G
			PHAYAO	0.2G
				0.6G
		APPENDIX 1.2: Maximum bearing displacement	MAECHAN	0.2G
				0.6G
			MAESAI	0.2G
				0.6G
			PHAYAO	0.2G
				0.6G
APPENDIX 2	Case with abutment and without shear dowels	APPENDIX 2.1: Maximum relative displacement	MAECHAN	0.4G
				0.6G
			MAESAI	0.4G
				0.6G
		APPENDIX 2.2.: Maximum bearing displacement	MAECHAN	0.4G
				0.6G
			MAESAI	0.4G
				0.6G
APPENDIX 3	Case without abutment and with shear dowels	APPENDIX 3.1: Maximum relative displacement	MAECHAN	0.4G
				0.6G
			MAESAI	0.4G
				0.6G
		APPENDIX 3.2: Maximum bearing displacement	MAECHAN	0.4G
				0.6G
			MAESAI	0.4G
				0.6G
APPENDIX 4	Verification of the convergence of the model			

APPENDIX 1: Case without abutment and without shear dowels:

APPENDIX 1.1: Maximum relative displacement on top of pier:

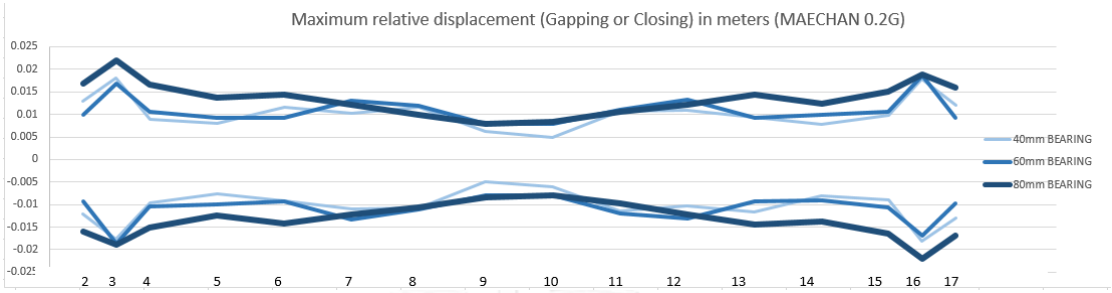

(a) Maximum relative displacement on top of pier in MAECHAN 0.2g

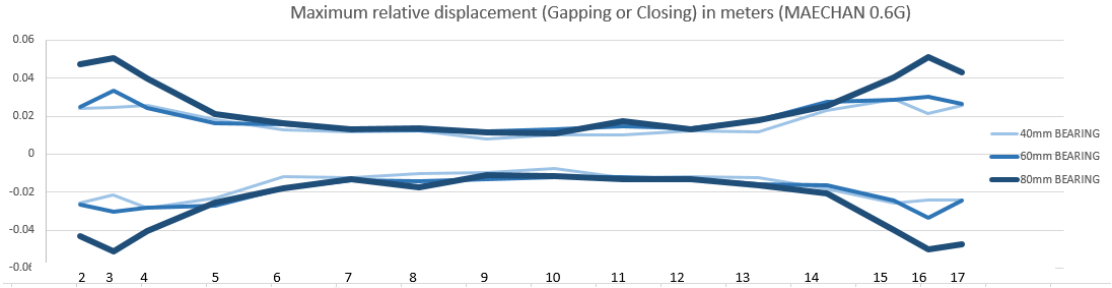

(b) Maximum relative displacement on top of pier in MAECHAN 0.6g

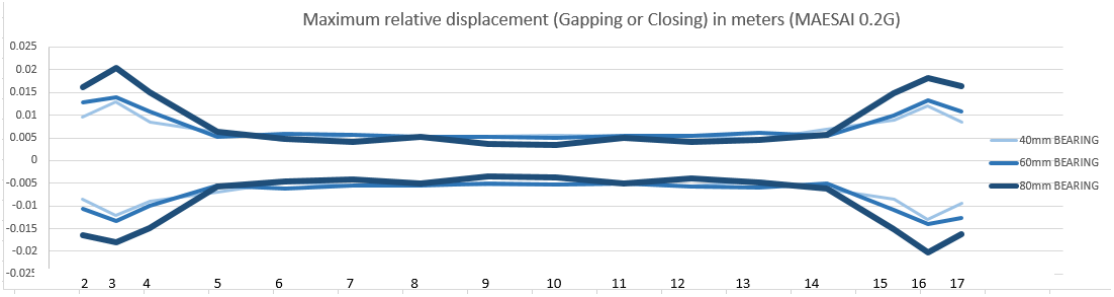

(c) Maximum relative displacement on top of pier in MAESAI 0.2g

Figure A.0.1: Maximum relative displacement on top of pier

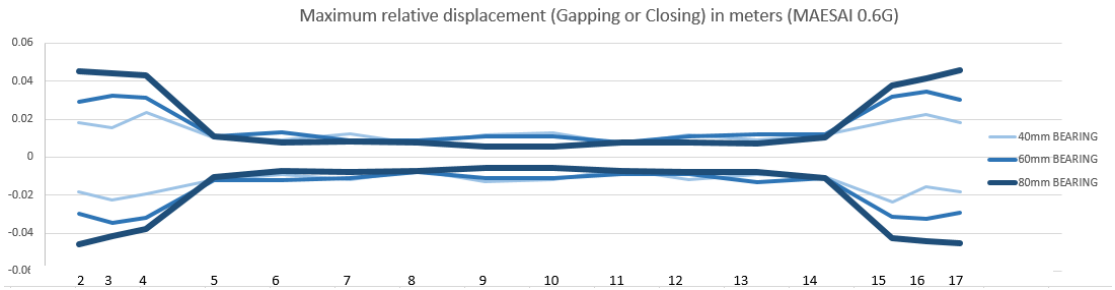

(d) Maximum relative displacement on top of pier in MAESAI 0.6g

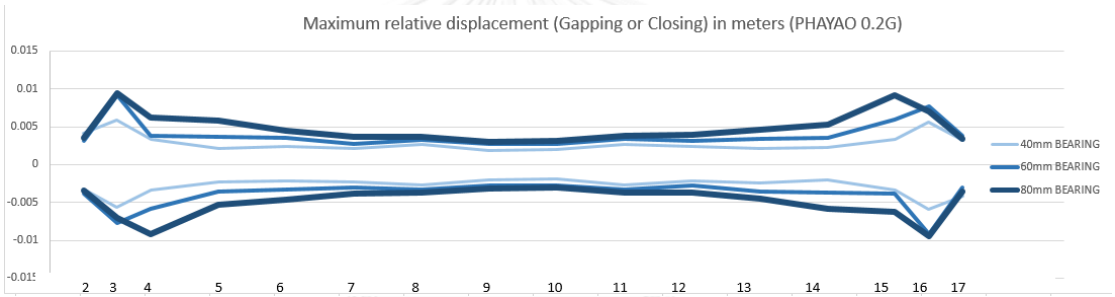

(e) Maximum relative displacement on top of pier in PHAYAO 0.2g

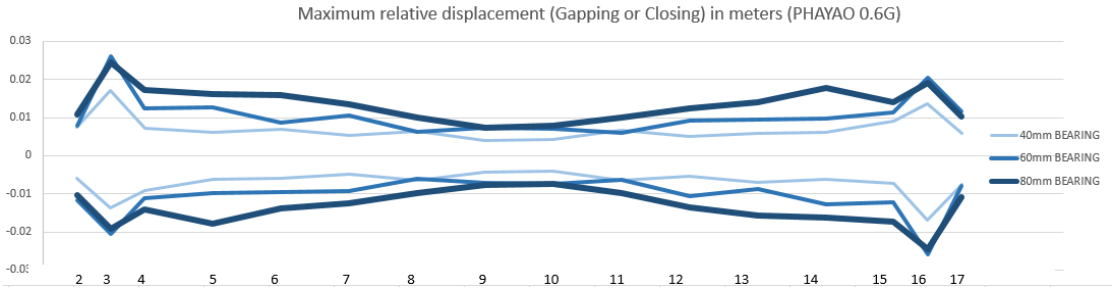

(f) Maximum relative displacement on top of pier in PHAYAO 0.6g

Figure A.0.1: Maximum relative displacement on top of pier (Continued)

APPENDIX 1.2: Maximum bearing displacement:

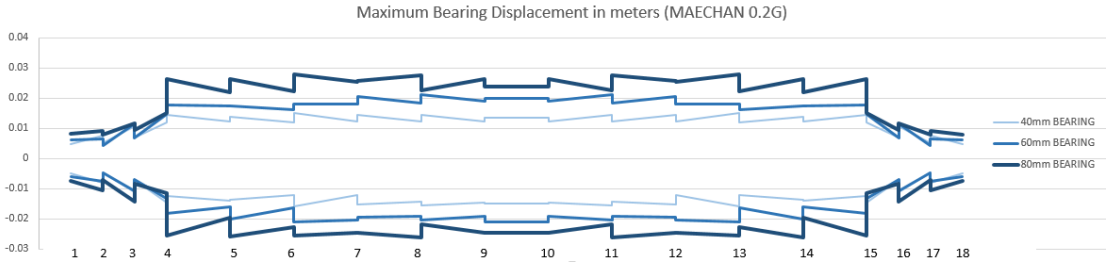

(a) Maximum bearing displacement in MAECHAN 0.2g

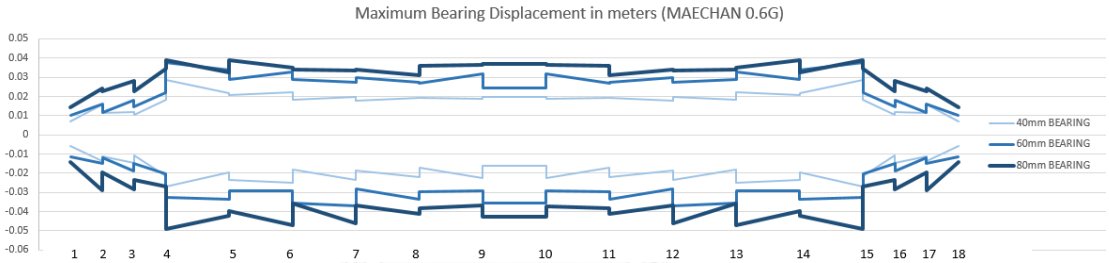

(b) Maximum bearing displacement in MAECHAN 0.6g

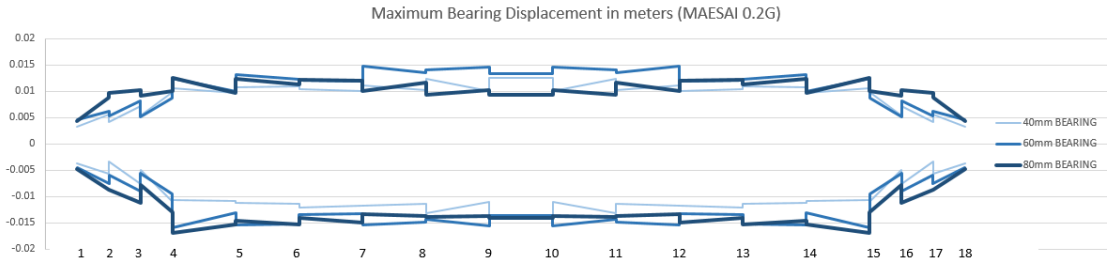

(c) Maximum bearing displacement in MAESAI 0.2g

Figure A.0.2: Maximum bearing displacement

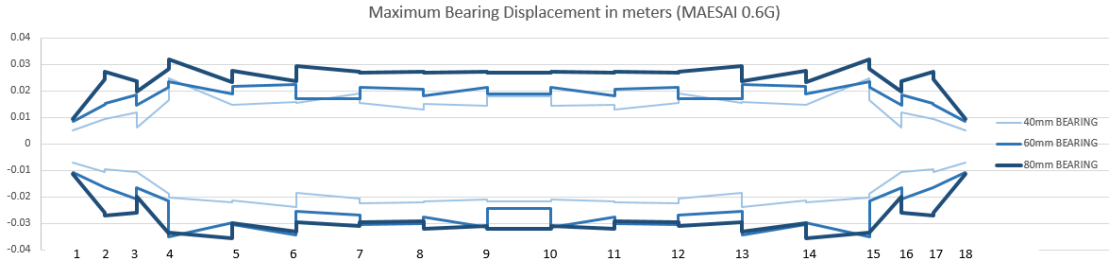

(d) Maximum bearing displacement in MAESAI 0.6g

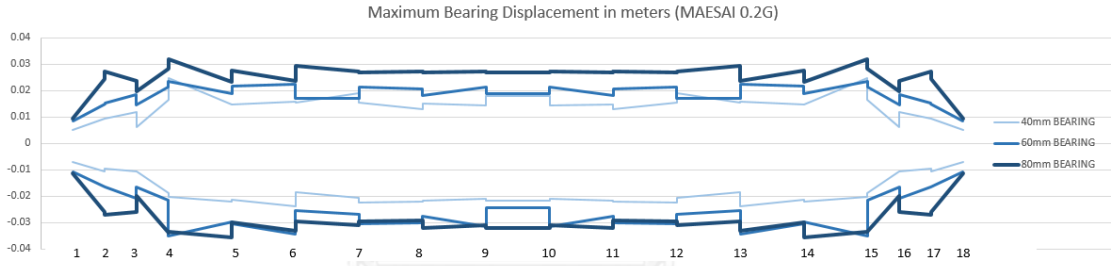

(e) Maximum bearing displacement in PHAYAO 0.2g

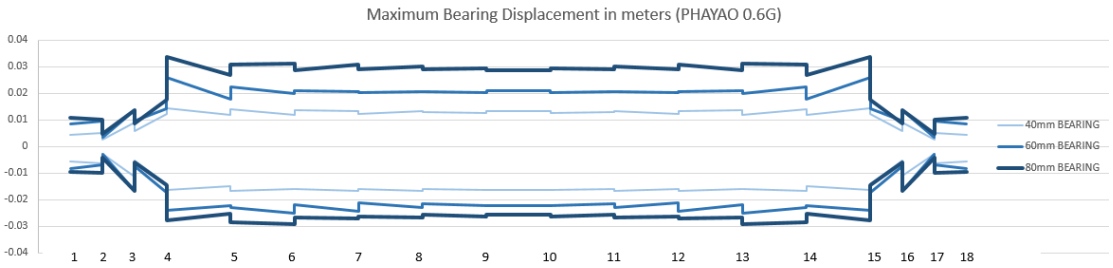

(f) Maximum bearing displacement in PHAYAO 0.6g

Figure A.0.2: Maximum bearing displacement (Continued)

APPENDIX 2: Case with abutment and without shear dowels:

APPENDIX 2.1: Maximum relative displacement on top of pier:

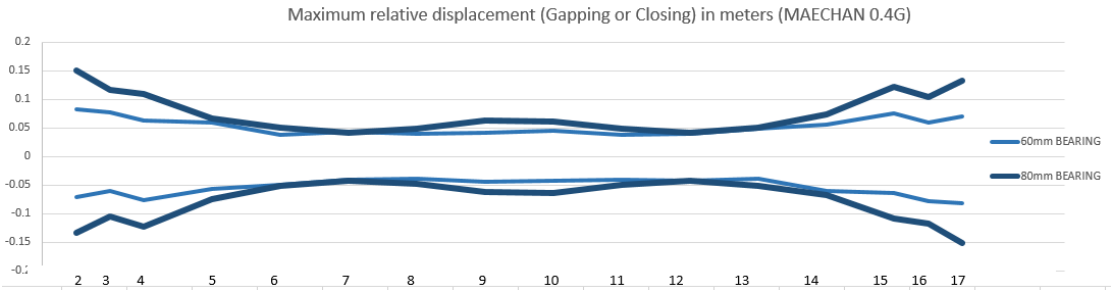

(c) Maximum relative displacement on top of pier in MAECHAN 0.4g

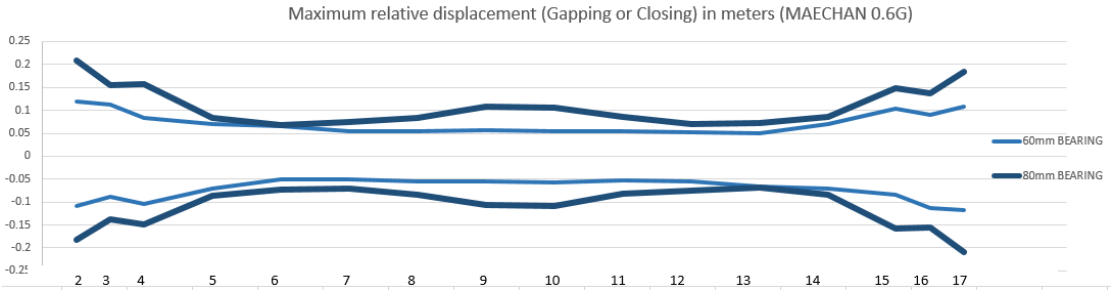

(b) Maximum relative displacement on top of pier in MAECHAN 0.6g

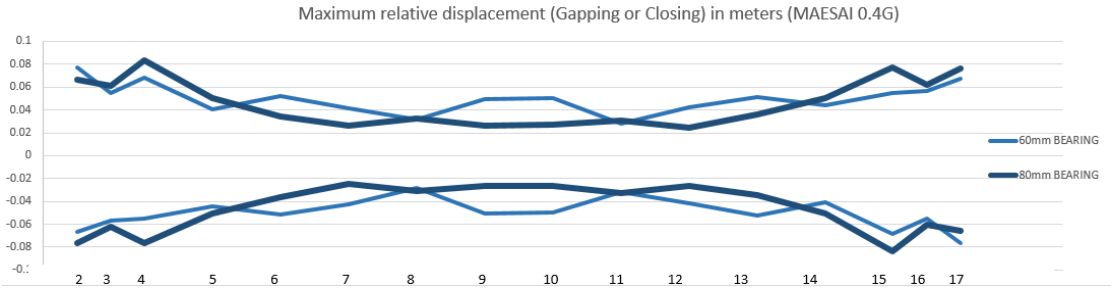

(a) Maximum relative displacement on top of pier in MAESAI 0.4g

Figure A.0.3: Maximum relative displacement on top of pier

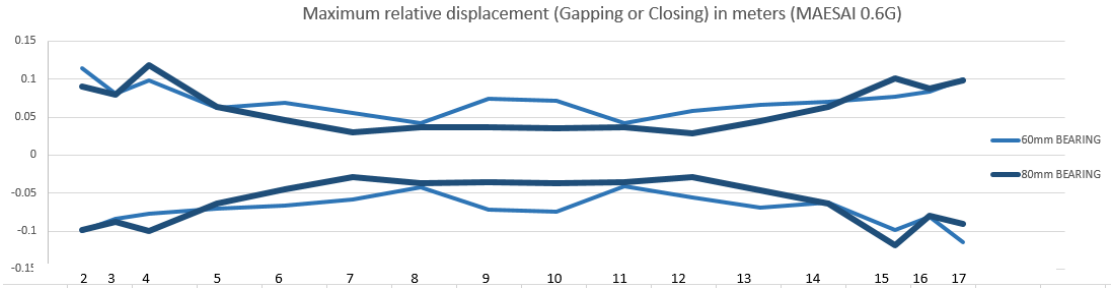

(d) Maximum relative displacement on top of pier in MAESAI 0.6g

Figure A.0.3: Maximum relative displacement on top of pier (Continued)

APPENDIX 2.2: Maximum bearing displacement

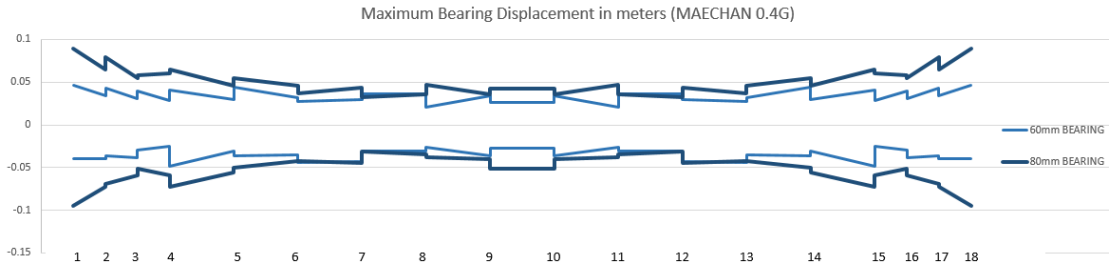

(a) Maximum bearing displacement on top of pier in MAECHAN 0.4g

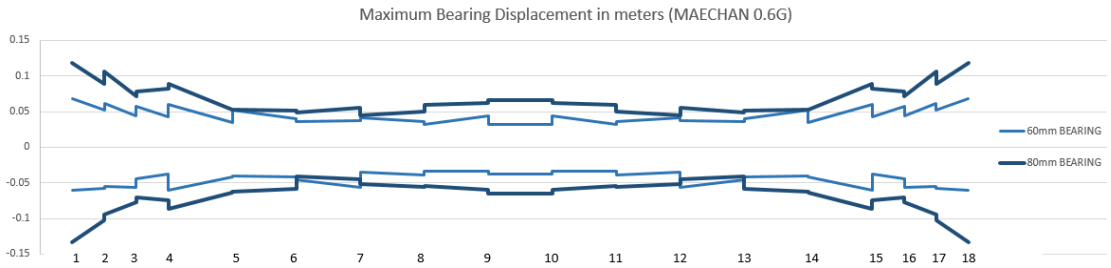

(b) Maximum bearing displacement on top of pier in MAECHAN 0.6g

Figure A.0.4: Maximum bearing displacement

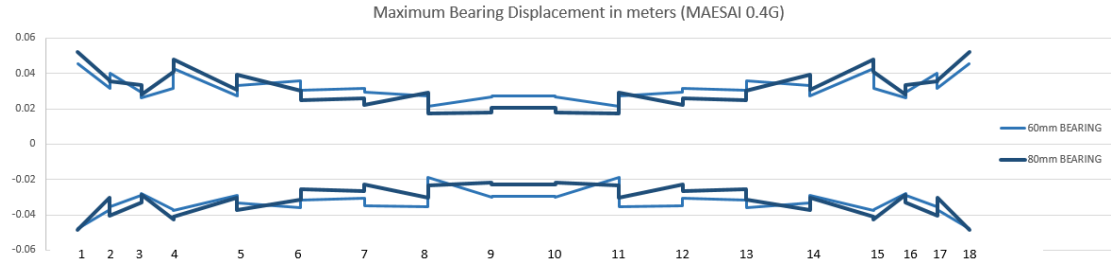

(c) Maximum bearing displacement on top of pier in MAESAI 0.4g

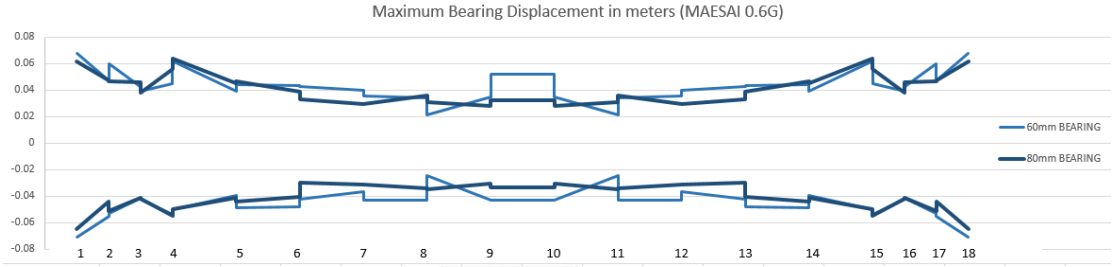

(d) Maximum bearing displacement on top of pier in MAESAI 0.6g

Figure A.0.4: Maximum bearing displacement (Continued)

APPENDIX 3: Case without abutment and with shear dowels

APPENDIX 3.1: Maximum relative displacement on top of pier

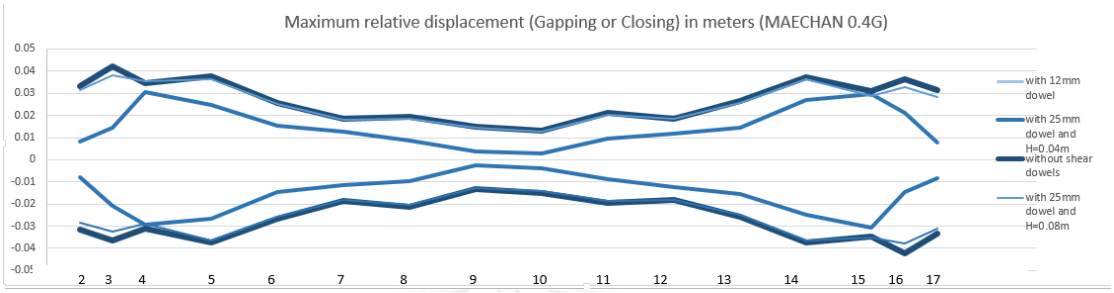

(a) Maximum relative displacement on top of pier in MAECHAN 0.4g

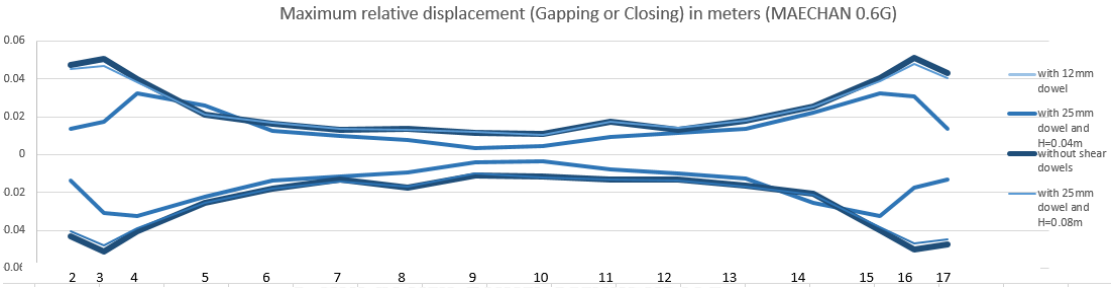

(b) Maximum relative displacement on top of pier in MAECHAN 0.6g

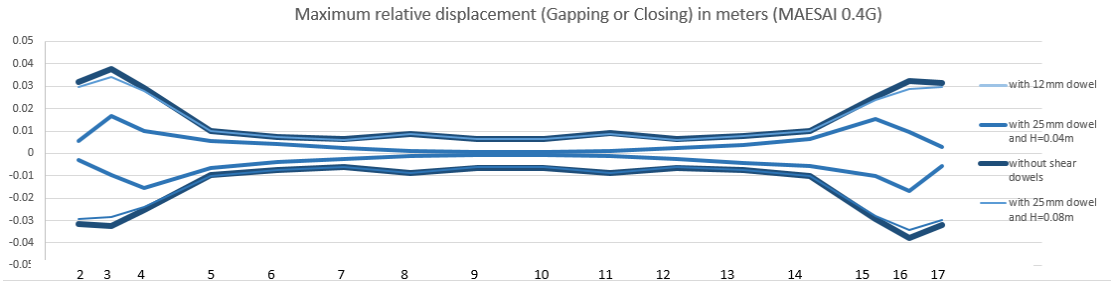

(c) Maximum relative displacement on top of pier in MAESAI 0.4g

Figure A.0.5: Maximum relative displacement on top of pier

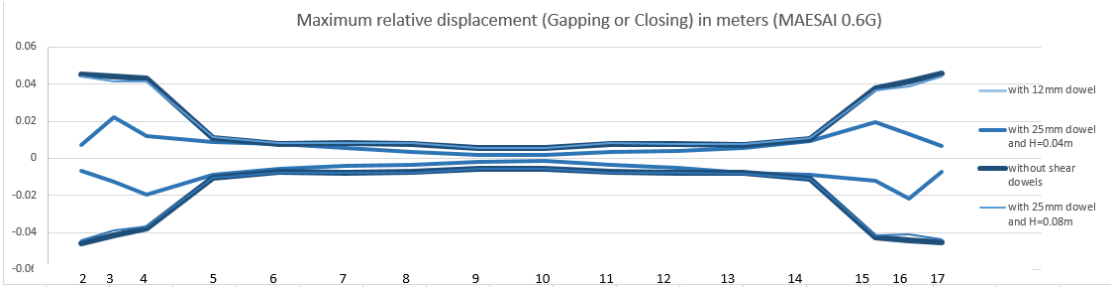

(d) Maximum relative displacement on top of pier in MAESAI 0.6g

Figure A.0.5: Maximum relative displacement on top of pier (Continued)

APPENDIX 3.2: Maximum bearing displacement

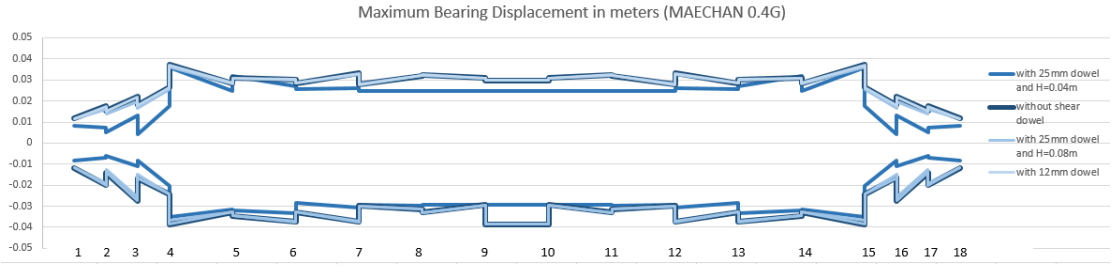

(a) Maximum bearing displacement on top of pier in MAECHAN 0.4g

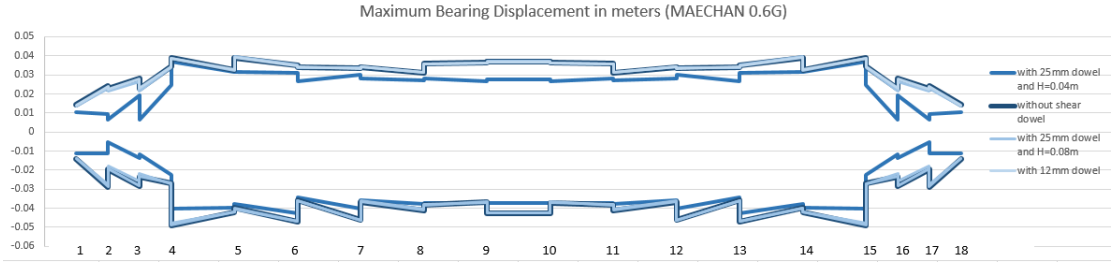

(b) Maximum bearing displacement on top of pier in MAECHAN 0.6g

Figure A.0.6: Maximum bearing displacement

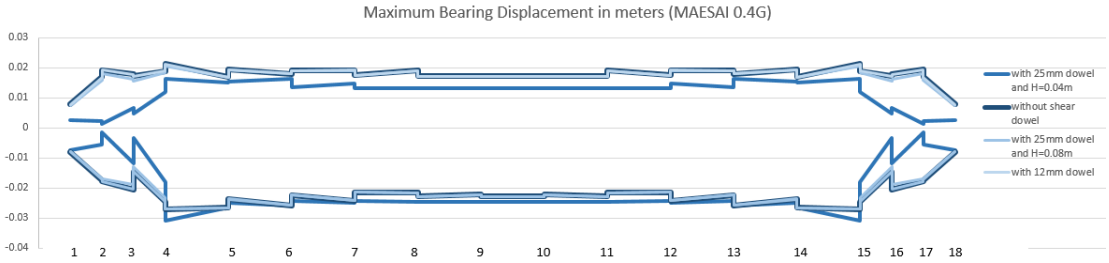

(c) Maximum bearing displacement on top of pier in MAESAI 0.4g

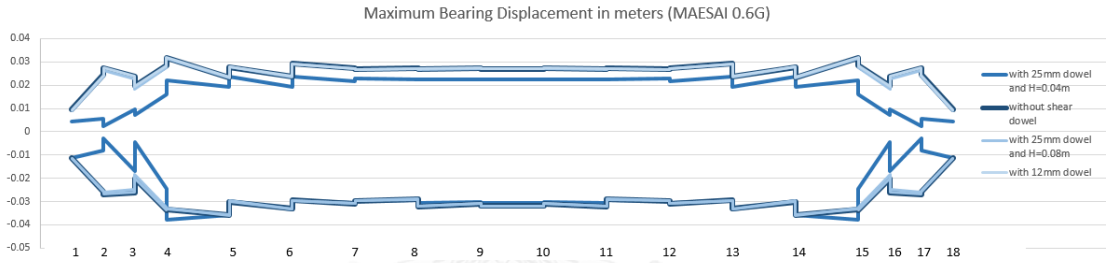

(d) Maximum bearing displacement on top of pier in MAESAI 0.6g

Figure A.0.6: Maximum bearing displacement (Continued)

APPENDIX 4: Verification of the convergence of the model

In order to verify the convergence of the model, the verification of the results with different time step (Δt) is conducted. The similar results are expected. The ground motion chosen to perform this check is PHAYAO ground motion with PGA of 0.4g and the case is the 8cm-thick bearing without shear dowels and abutment soil spring. The time step was varied with 0.005s and 0.001s. These two time steps were put in the analysis and the results in term of the maximum displacement on top of the piers are shown in the following:

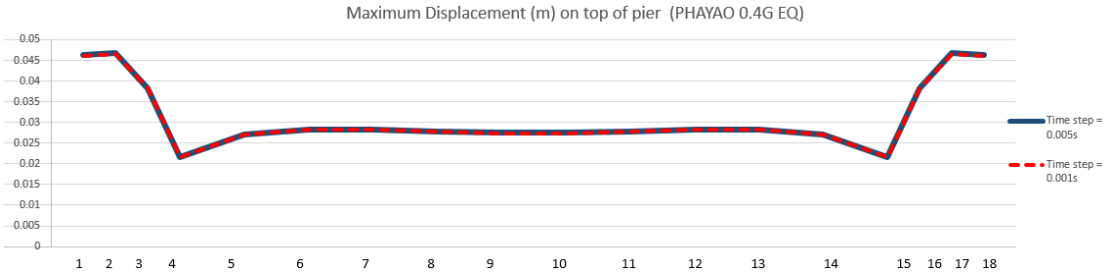

Figure A.0.7: Maximum displacement on top of pier in PHAYAO ground motion

As observed, the maximum displacement on top of all piers of the whole bridge gives similar results although it is not absolutely the same. However, the results are acceptable since the difference is less than 1% as shown in the table below:

Table A.0.1: The difference of the maximum displacement with different time steps

Pier No		1	2	3	4	5	6	7	8	9
Dispalcement (mm)	Δt= 0.005s	46.3	46.7	38.3	21.7	27.1	28.4	28.3	27.9	27.5
	Δt= 0.001s	46.1	46.6	38.1	21.7	27.2	28.4	28.2	27.9	27.4
Difference (%)		0.41	0.26	0.33	0.01	0.14	0.04	0.14	0.09	0.09

Pier No		10	11	12	13	14	15	16	17	18
Dispalcement (mm)	Δt= 0.005s	27.5	27.9	28.3	28.4	27.1	21.7	38.3	46.7	46.3
	Δt= 0.001s	27.4	27.9	28.2	28.4	27.2	21.7	38.1	46.6	46.1
Difference (%)		0.09	0.09	0.14	0.04	0.14	0.01	0.33	0.26	0.41

The results in term of the displacement is quite similar for both time step. This can prove that the convergence of the model can be trusted and applicable.

VITA

He was born in Phnom Penh city, the capital of Cambodia. He went to Chhbar Ampov primary school in Phnom Penh city. Then I studied in Chhbar Ampov High School from 7th grade to 12th grade. After passing the national exam, He went to study for my bachelor in engineering in the field of civil engineering in 2008 at Institute of Technology of Cambodia (ITC). He won the AUN/SeedNet scholarship to pursue his study in master degree at Chulalongkron university in the same year.